Supporting information

Structure–Activity Relationships of ATCUN-Based Cu(II) Complexes with large chelate rings: Interplay of ROS Generation, DNA Binding, and Nuclease Activity

Julian Heinrich, Johanna Lück, Dmitrii Varlakhanov, Ravi Kumar, Matthias Stein, Nora Kulak*

S-1 Materials and general methods

All chemicals and solvents were purchased from *Sigma-Aldrich*, *Merck*, *Fisher Scientific*, *Acros Organics*, *Carl Roth*, *TCI*, *VWR* and *Carbolution Chemicals*, respectively, and were used without further purification. Copper(II) chloride ($CuCl_2$) was used as the dihydrate. As ascorbate and pyruvate source, the sodium salt was used. In general, Milli-Q® water (18 MΩ·cm) was used as a solvent.

For the purification of the synthesized peptides, a *VWR Hitachi Chromaster 5000* HPLC system (reversed phase) was used. UV/VIS spectroscopy was carried out on a *Varian Cary 100 Bio UV/VIS spectrophotometer* and circular dichroism (CD) spectroscopy on a *Chirascan Original*

from *Applied Photophysics.* For fluorescence spectroscopy a *Varian Cary Eclipse spectrofluorimeter* was used. For electrospray ionization-mass spectrometry (ESI-MS) a LC-MS system was used. LC-MS measurements were carried out on a UPLC system (*Waters Acquity UPLC® H-Class*) coupled to a mass spectrometer (*Waters Xevo G2 Tof MS*). A C18 column (*Waters Acquity UPLC® BEH C18 1.7 µm*) was used. The mobile phase consisted of 2 mM ammonium acetate in water (A) and acetonitrile (B). The gradient was 2% B (v/v) for 0.5 min, 2-98% B in 2.5 min, 98% B for 1 min, back to 2% B in 0.2 min and 2% B for 0.8 min (total run time: 5 min). The flow rate was 0.4 mL/min and the sample injection volume was 2 µL (*Waters Sample Manager - FTN*).

S-2 Peptide synthesis

The synthesized ATCUN-based peptides have the general sequence of N-X-aa2-His-Lys-Lys-$CONH_2$ with aa2 being either Gly or β-Ala. N-X- stands either for an amine group, the different 3,5-substituted pyrazolyl (CH_3-, CF_3-) or the triazolyl moiety (Figure S1).

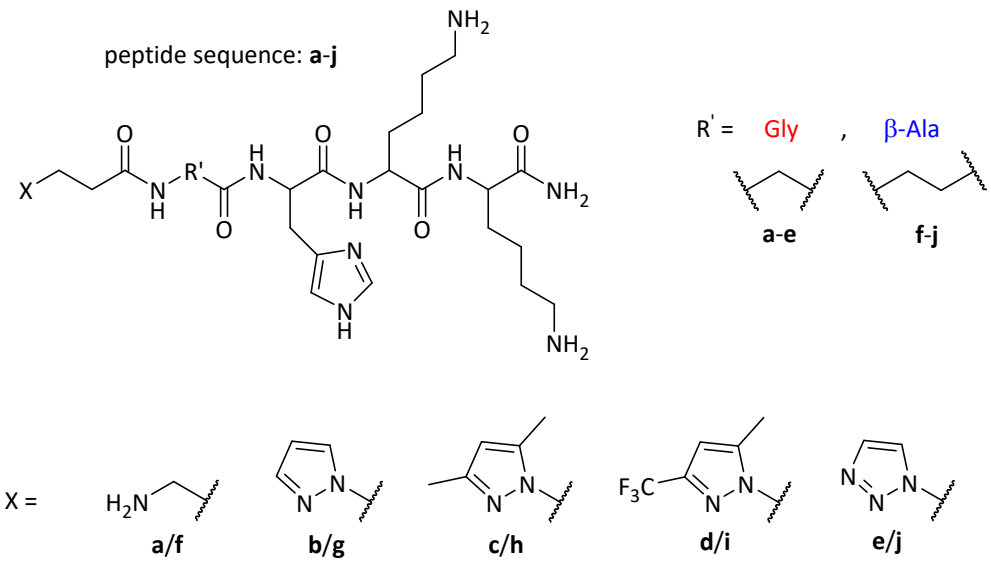

Figure S1. Synthesized ATCUN-based peptides **a**-**j** with the general sequence N-X-aa2-His-Lys-Lys-$CONH_2$ and variation of aa2 being Gly or β-Ala and N-X- being an amine group, 3,5-substituted (CH_3-, CF_3-) pyrazoles or a triazole moiety. The C-terminus is amidated.

S-2.1 Solid-phase peptide synthesis (SPPS)

All ATCUN-based peptides were prepared through the Fmoc strategy by using a rink amide MBHA resin as solid support. *Tert*-butyloxycarbonyl (Boc) for Lys and trityl (Trt) for His were chosen as side chain protecting groups of the amino acids. For all peptides, the corresponding L-amino acids were applied in peptide synthesis. Whereas for N-terminal GABA coupling (**a** and **f**) Fmoc-GABA-OH was used, for **b**-**e** and **g**-**j** the corresponding (3,5-substituted, CH_3-/ CF_3-) pyrazolyl or triazolyl 3-propionic acid was used in SPPS.

All synthesis steps were done in a syringe reaction vessel in DMF (*GPR Rectapur*). Rink amide MBHA resin (200 mg, 0.118 mmol) was incubated for 1 h in DMF (3 mL) for swelling. Fmoc deprotection was carried out in 20% piperidine in DMF (3 mL) for 20 min. The coupling of the amino acids was performed for 2 h with a mixture of the corresponding Fmoc-protected amino acid (0.472 mmol, 4 eq.), the activating agent PyBOP (246 mg, 0.472 mmol, 4 eq.) and *N*,*N* diisopropylethylamine (DIPEA, 200 µL) in DMF (3 mL). For the corresponding pyrazolyl and triazolyl propionic acid units 8 eq. and 24 h coupling time were used and all other components were adjusted to ensure the same ratio in the coupling mixture, respectively.
After each step of the procedure (deprotection/coupling) the solid support was washed 5 times with DMF (3 mL). An additional washing step with 5 times dichloromethane (3 mL) was only carried out directly before cleavage of the synthesized peptides from the solid support. The cleavage of the peptides and simultaneous deprotection of the amino acid side chains was carried out for 3.5 h with a mixture of trifluoroacetic acid (TFA), triisopropylsilane (TIPS) and H_2O (90:5:5; 2.5 mL). The peptides were precipitated and washed two times with ice-cold diethyl ether.

S-2.2 High performance liquid chromatography (HPLC)

Purification of the crude peptides **a**-**j** was performed *via* semi-preparative RP-HPLC using a C18 column (LiChrospher® 100 RP-18, 10 µm, 10 mm x 250 mm, *Merck*). The eluent consisted of H_2O + 0.1% TFA (solvent A) and MeOH + 0.1% TFA (solvent B). The gradient was 5% B for 5 min, 5-95% B over 25 min, 95% B for 7 min, 95-5% B over 3 min, and finally 5% B for 5 min. The flow was 4 mL/min. The retention times (rt) of the corresponding peptides under the conditions described above were obtained by the UV/VIS-spectroscopic detection at 245 nm for **c** and **h** and 240 nm for all other peptides. The collected fractions of peptide-trifluoroacetate salts were lyophilized and weighed for yield determination. Due to differences in the number of protonation sites of the peptides the amount of trifluoroacetate in the eluted peptide salts differs and therefore determination of the yield just by weighing can be inaccurate. For **a**-**c** and **f**-**h**, we expect the presence of four trifluoroacetate counterions caused by either a protonation of the terminal amine group due to GABA coupling or a

protonation of the pyrazolyl moiety (N terminus), the imidazole nitrogen (His) and amine groups of two Lys side chains. For all other peptides **d**-**e** and **i**-**j** three trifluoroacetate anions are expected, as the N-terminus is not protonated.[1]

A summary of the respective retention times, sample masses, molar masses of the peptide-trifluoroacetate salt and peptide yields determined by weighing are given in Table S1. The actual yields were determined by UV/VIS spectroscopy (see S-3).

Table S1. Retention times (rt) of the synthesized peptides during semi-preparative RP-HPLC purification with a C18 column (10 µm, 10 x 250 mm), weight after drying under vacuum, molar mass of peptide trifluoroacetate salt (**a**-**c** and **f**-**h** = 4 trifluoroacetate anions, **d**-**e** and **i**-**j** = 3 trifluoroacetate anions) and yield by weighing of the peptides.

peptide	rt [min]	m [mg]	M [g/mol]	yield [%]
a	4.57	63.4	1008.77	53.26
b	6.89	45.1	1045.79	36.55
c	11.10	55.2	1073.85	43.56
d	13.52	31.0	1013.80	25.91
e	5.18	49.0	932.76	44.52
f	4.73	49.3	1022.80	40.85
g	7.39	47.0	1059.82	37.58
h	10.83	43.1	1087.88	33.57
i	14.57	27.2	1027.82	22.43
j	5.44	60.0	946.79	53.71

For evidence of purity, analytical RP-HPLC runs with a C18 column (LiChrospher® 100 RP 18, 5 µm, 3 mm x 250 mm, *Merck*) and the same gradient as in the semi-preparative runs were carried out. Due to different column conditions (semi-preparative *vs.* analytical) the rt of the purified peptides **a**-**j** are slightly shifted. The chromatograms of the analytical runs for each peptide **a**-**j** are presented in Figures S2-S11.

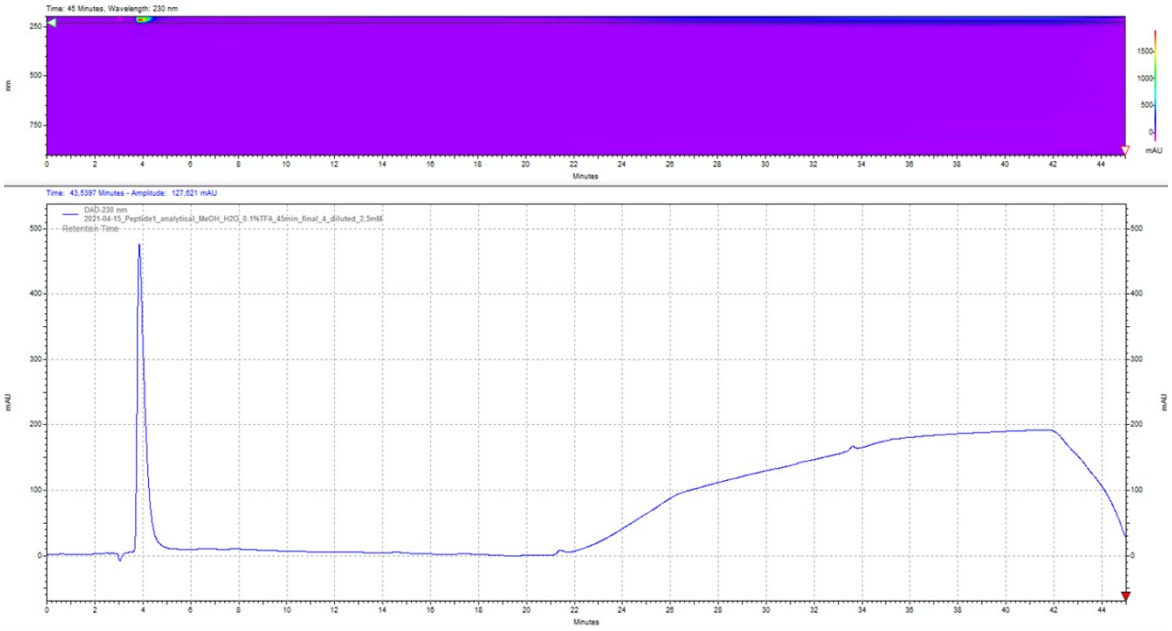

Figure S2. Chromatogram of the analytical RP-HPLC run for **a** (λ = 230 nm; same gradient as in semi-preparative purification).

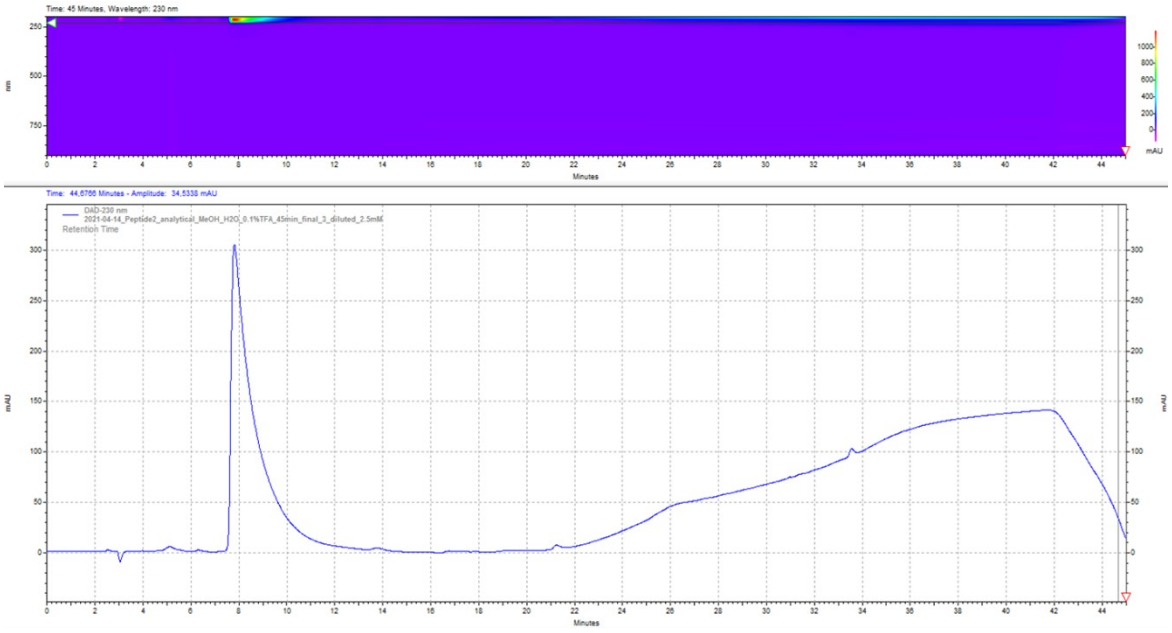

Figure S3. Chromatogram of the analytical RP-HPLC run for **b** (λ = 230 nm; same gradient as in semi-preparative purification).

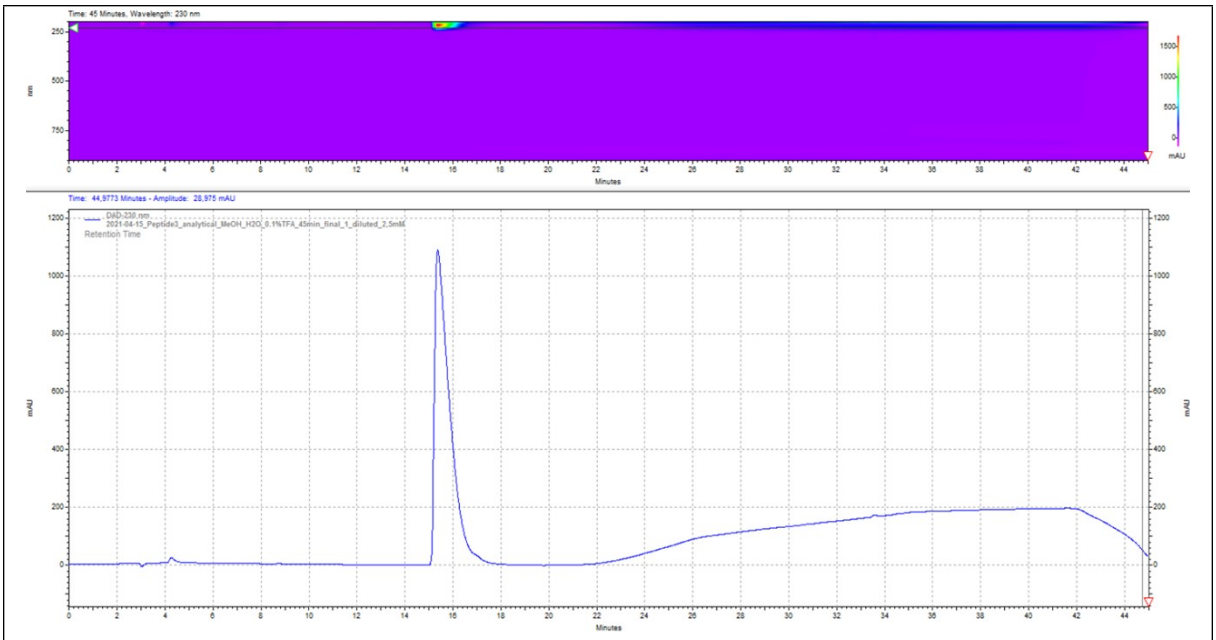

Figure S4. Chromatogram of the analytical RP-HPLC run for **c** (λ = 230 nm; same gradient as in semi-preparative purification).

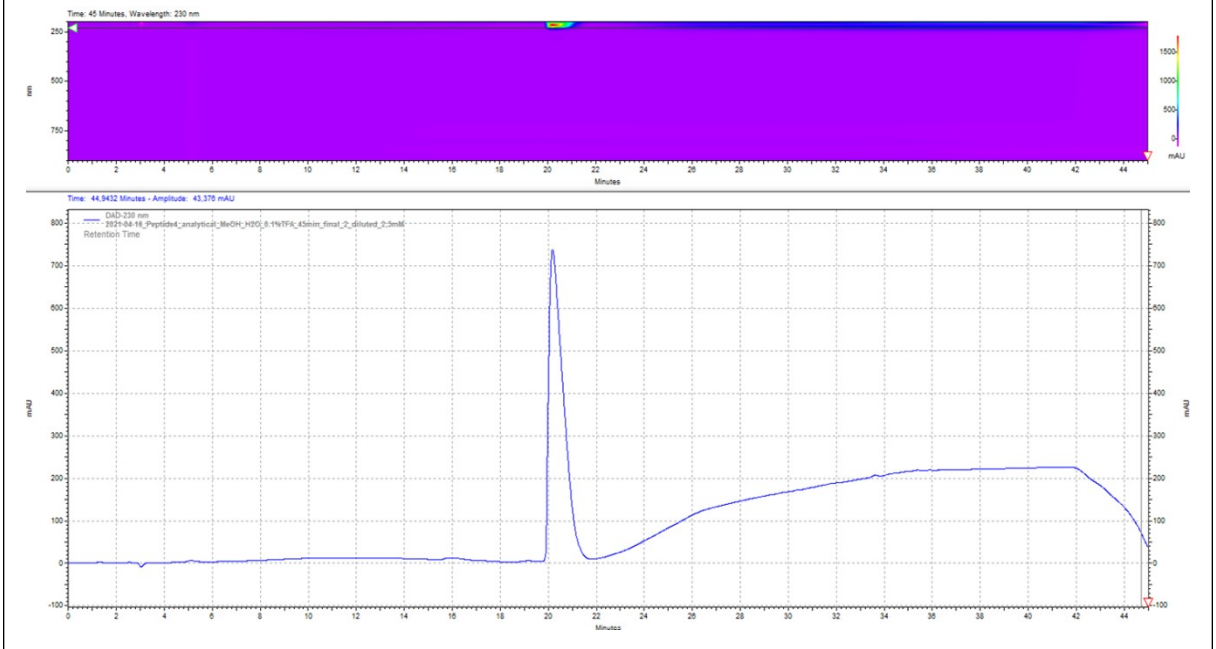

Figure S5. Chromatogram of the analytical RP-HPLC run for **d** (λ = 230 nm; same gradient as in semi-preparative purification).

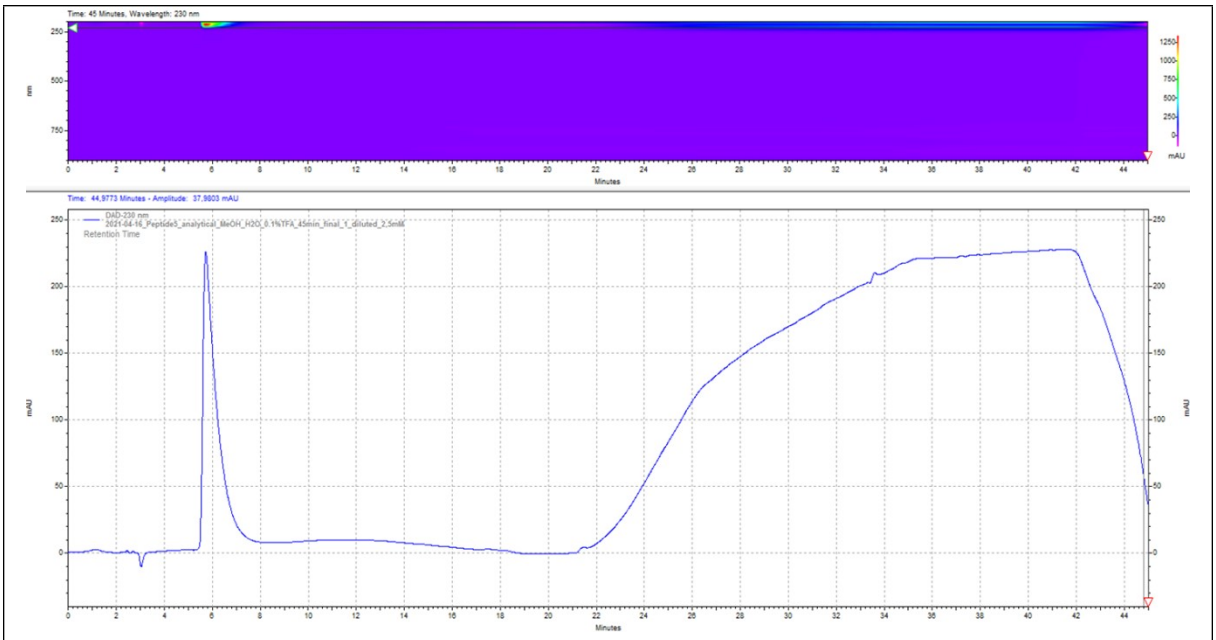

Figure S6. Chromatogram of the analytical RP-HPLC run for **e** (λ = 230 nm; same gradient as in semi-preparative purification).

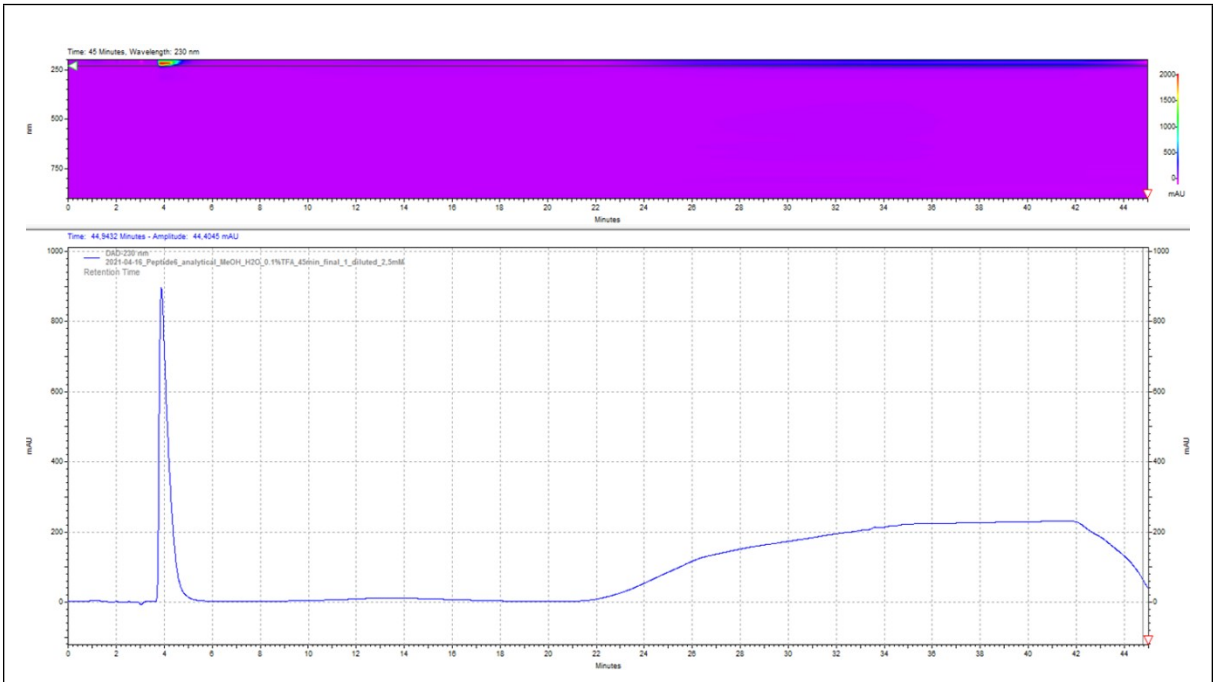

Figure S7. Chromatogram of the analytical RP-HPLC run for **f** (λ = 230 nm; same gradient as in semi-preparative purification).

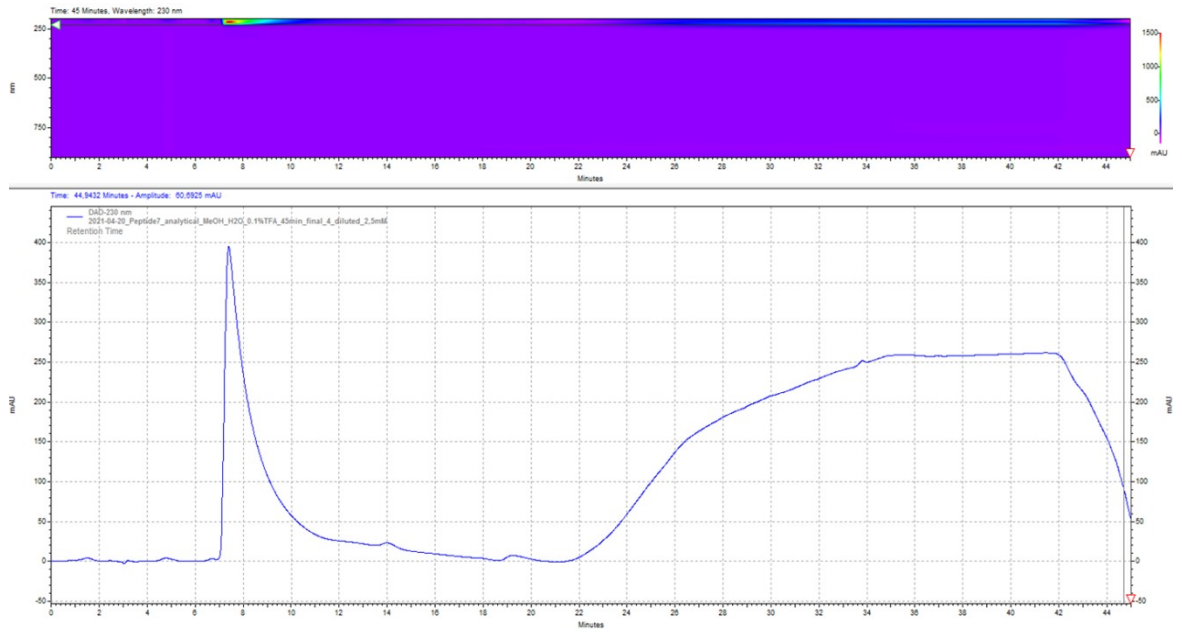

Figure S8. Chromatogram of the analytical RP-HPLC run for **g** (λ = 230 nm; same gradient as in semi-preparative purification).

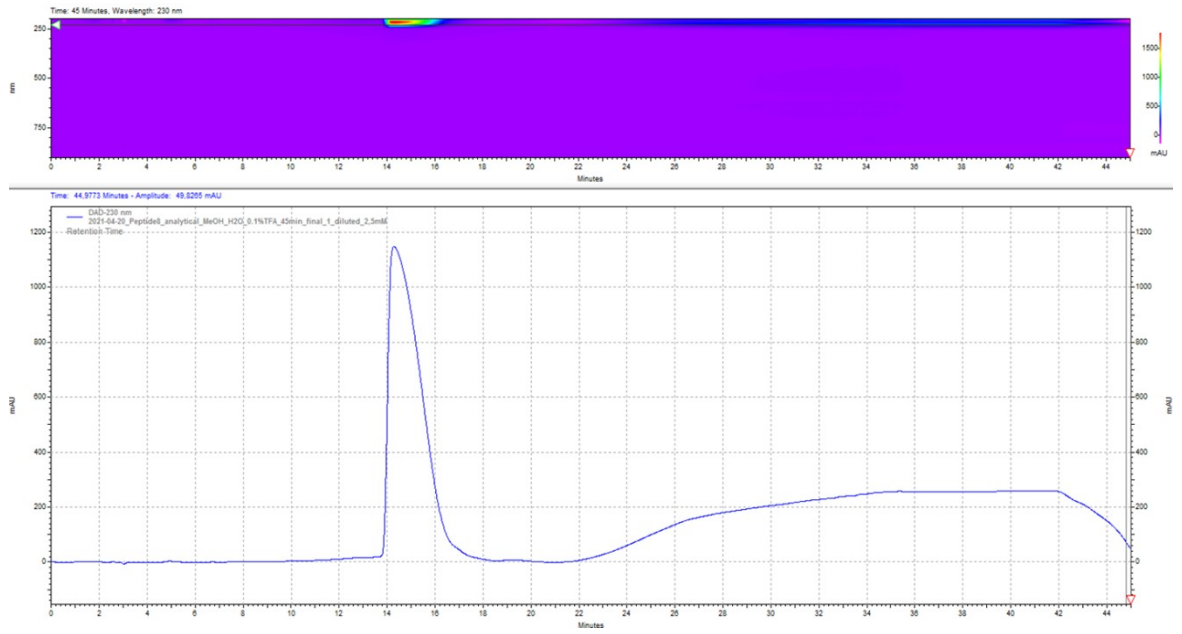

Figure S9. Chromatogram of the analytical RP-HPLC run for **h** (λ = 230 nm; same gradient as in semi-preparative purification).

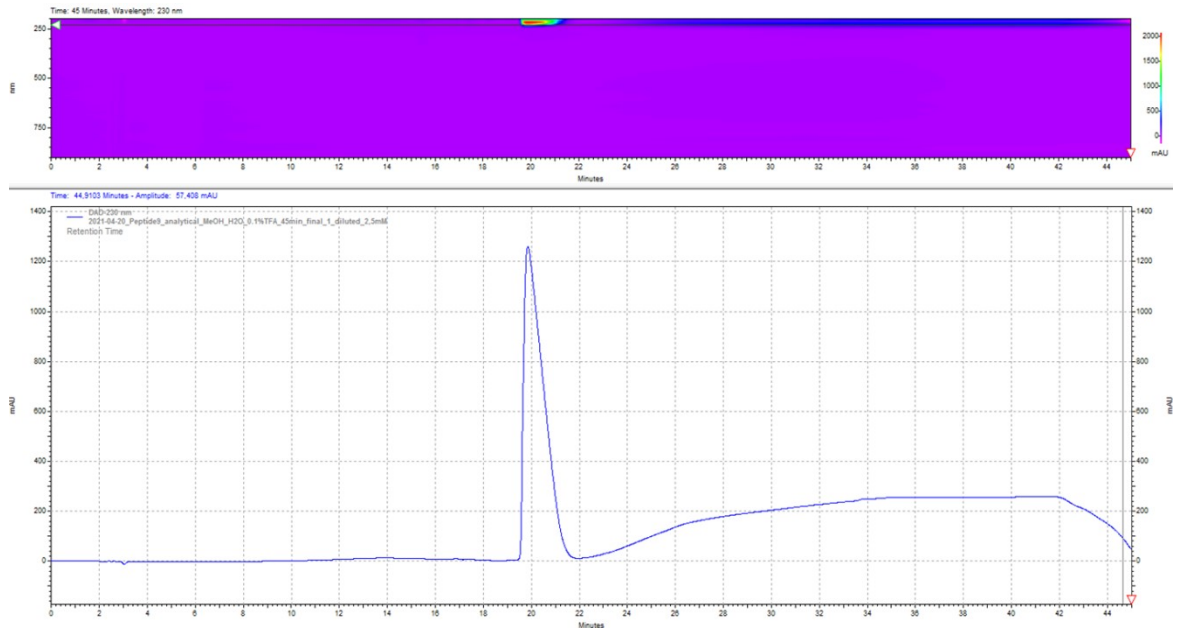

Figure S10. Chromatogram of the analytical RP-HPLC run for **i** (λ = 230 nm; same gradient as in semi-preparative purification).

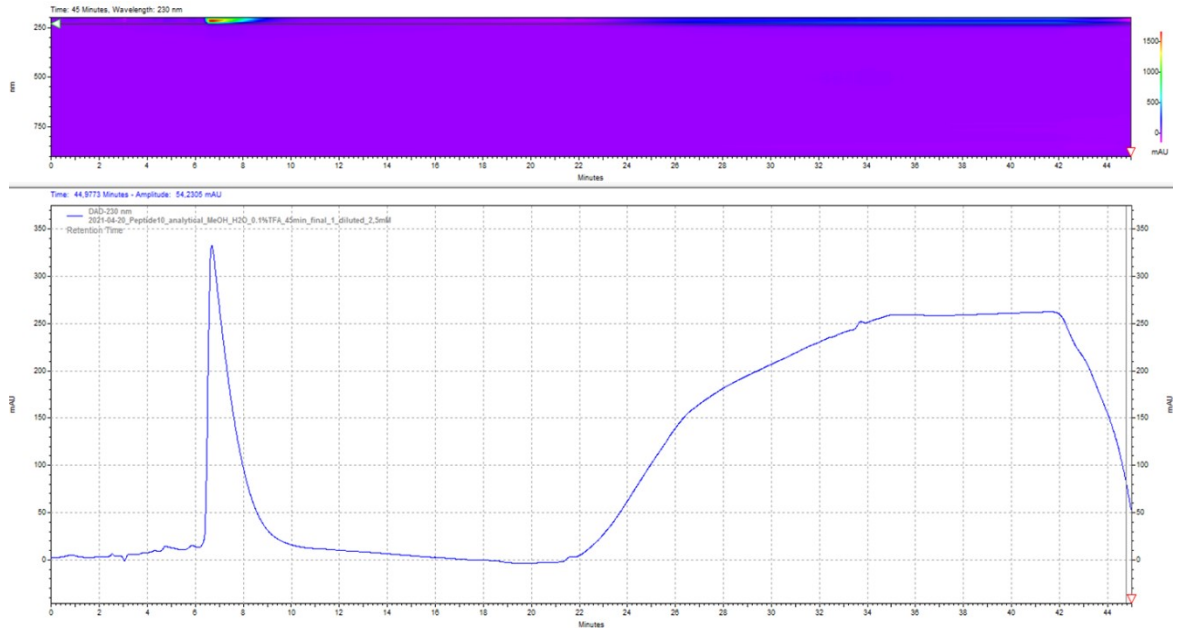

Figure S11. Chromatogram of the analytical RP-HPLC run for **j** (λ = 230 nm; same gradient as in semi-preparative purification).

S-2.3 Electrospray ionization-mass spectrometry (ESI-MS)

High-resolution (HR) ESI-MS was applied for characterization of the purified peptides **a**-**j**. The calculated and found masses are listed in Table S2. The HR ESI mass spectra are shown in Figures S12–S21.

Table S2. Calculated and found *m/z* values in HR ESI-MS of the synthesized peptides **a**-**j** after semipreparative RP-HPLC purification.

compound	calculated: $[M+H]^+$ $[2M+H]^+$	found: $[M+H]^+$ $[2M+H]^+$
a	553.3569 1105.7066	553.3568 1105.7062
b	590.3522 1179.6971	590.3522 1179.6963
c	618.3835 1235.7597	618.3715 --- *
d	672.3553 1343.7031	672.3563 --- *
e	591.3474 1181.6876	591.3489 --- #
f	567.3726 1133.7379	567.3729 1133.7390
g	604.3678 1207.7284	604.3688 --- *
h	632.3991 1263.7910	632.4025 --- *
i	686.3709 1371.7344	686.3729 --- *
j	605.3631 1209.7189	605.3636 --- *

* Not in the measured range of 100 – 1200 *m/z*.

\# Peak visible, but no value was detected by the software of the instrument.

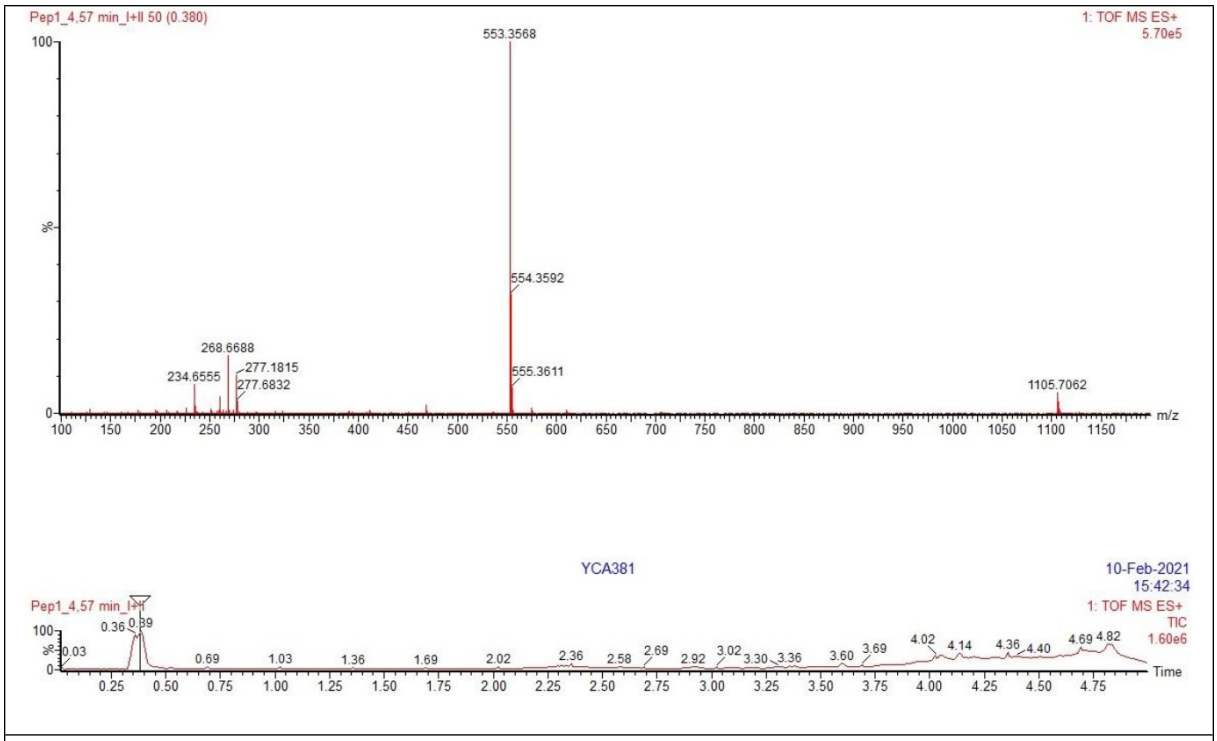

Figure S12. (Top) After semi-preparative RP-HPLC purification, mass spectrum of **a** in a *m*/*z* range of 100 – 1200 *m/z* collected *via* a LC-MS measurement. (Below) The corresponding total ion current (TIC) chromatogram. H_2O was used for LC-MS sample dilution.

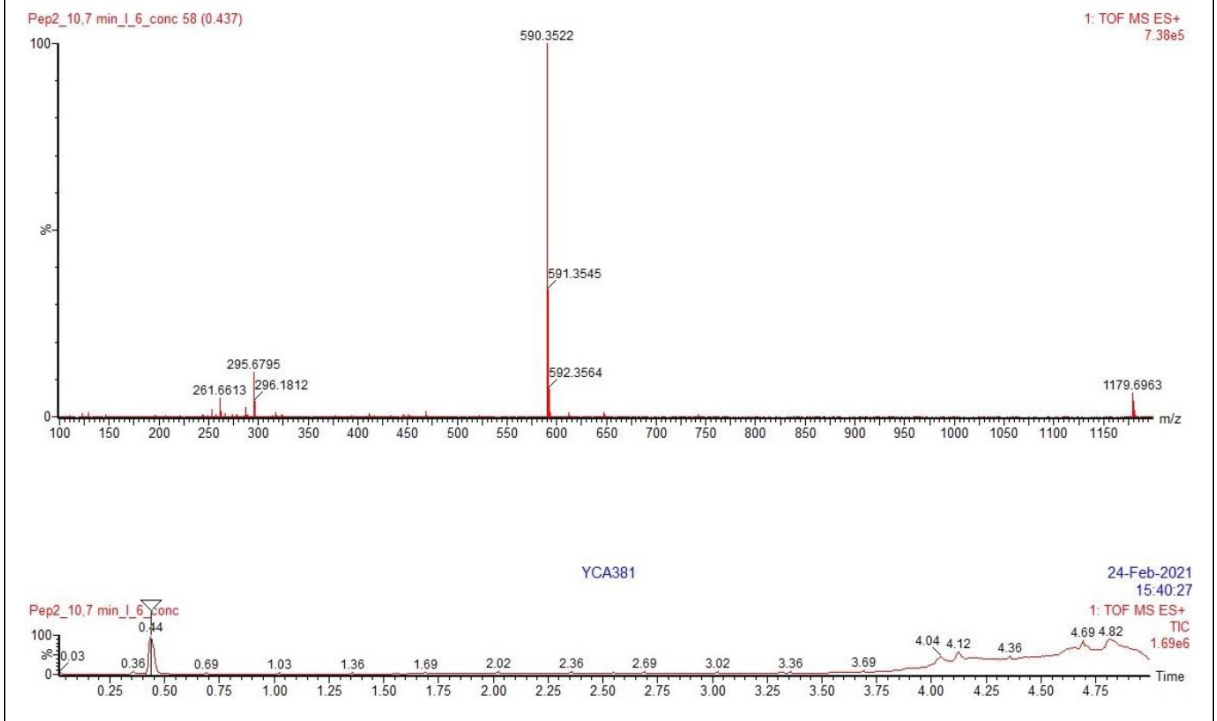

Figure S13. (Top) After semi-preparative RP-HPLC purification, mass spectrum of **b** in a *m*/*z* range of 100 – 1200 *m/z* collected *via* a LC-MS measurement. (Below) The corresponding total ion current (TIC) chromatogram. H_2O was used for LC-MS sample dilution.

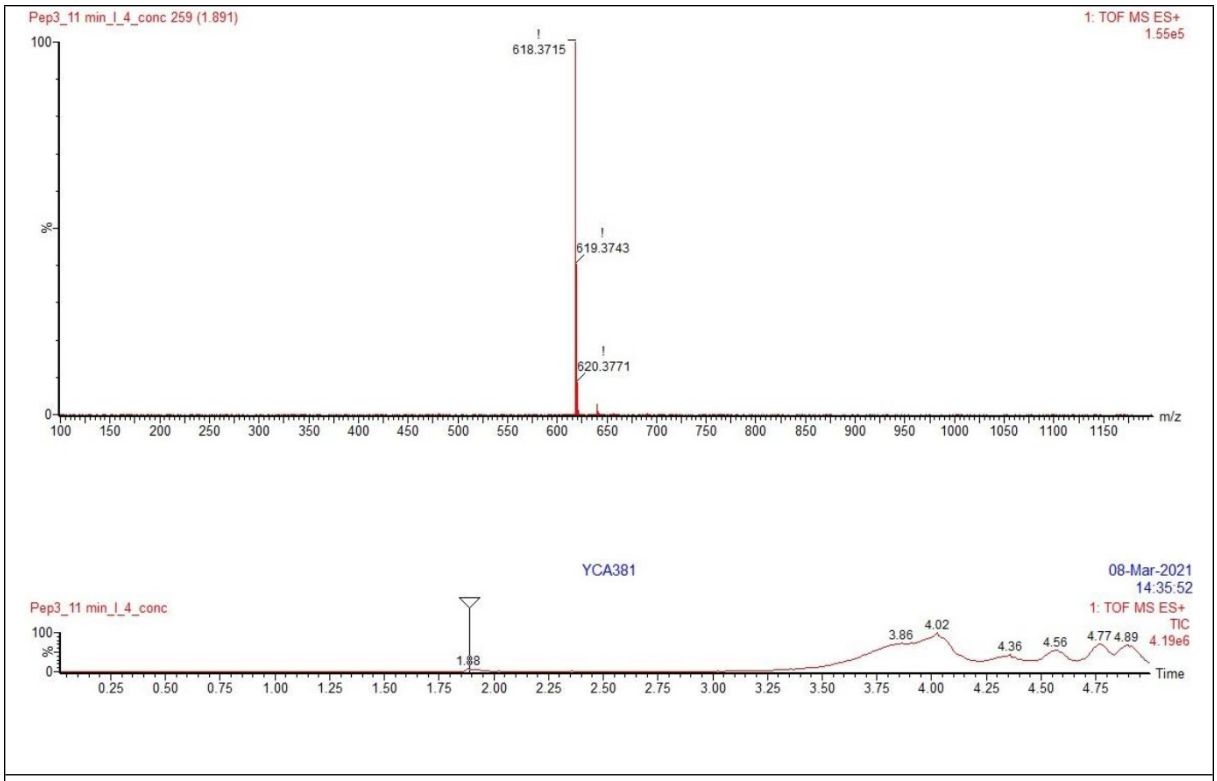

Figure S14. (Top) After semi-preparative RP-HPLC purification, mass spectrum of **c** in a *m/z* range of 100 – 1200 *m/z* collected *via* a LC-MS measurement. (Below) The corresponding total ion current (TIC) chromatogram. H_2O was used for LC-MS sample dilution.

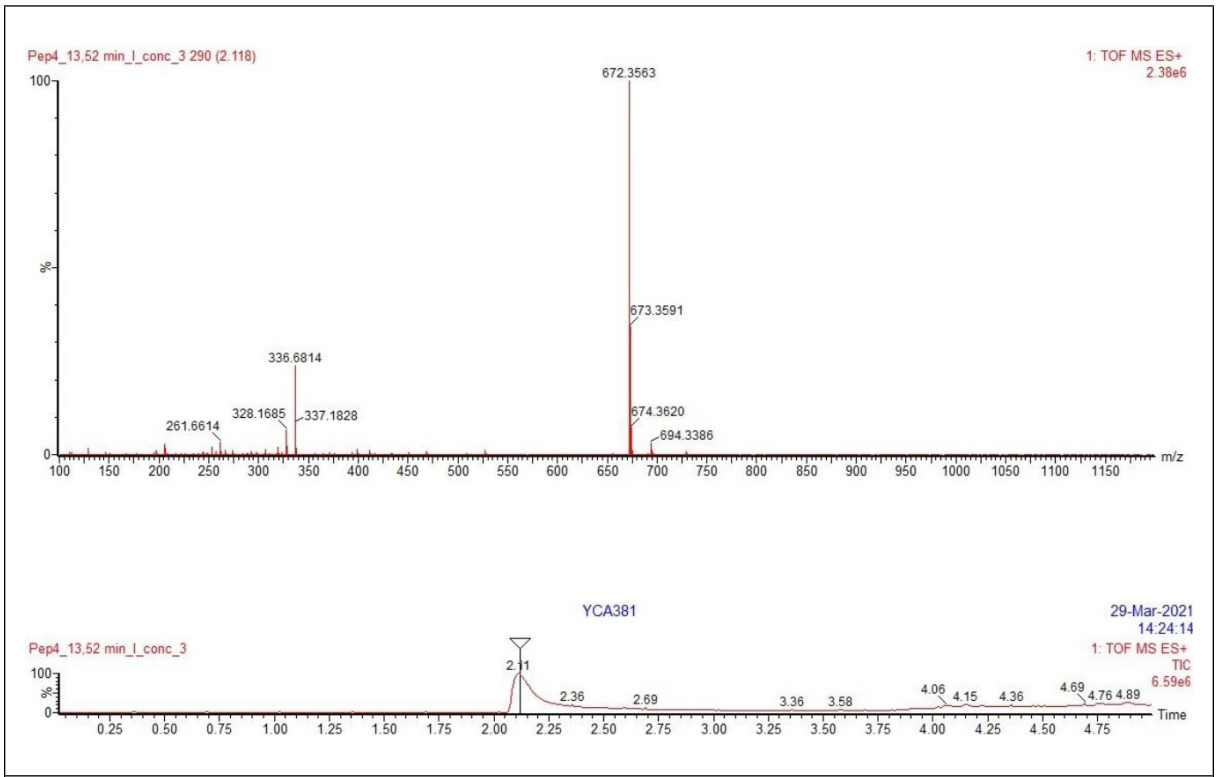

Figure S15. (Top) After semi-preparative RP-HPLC purification, mass spectrum of **d** in a *m/z* range of 100 – 1200 *m/z* collected *via* a LC-MS measurement. (Below) The corresponding total ion current (TIC) chromatogram. H_2O was used for LC-MS sample dilution.

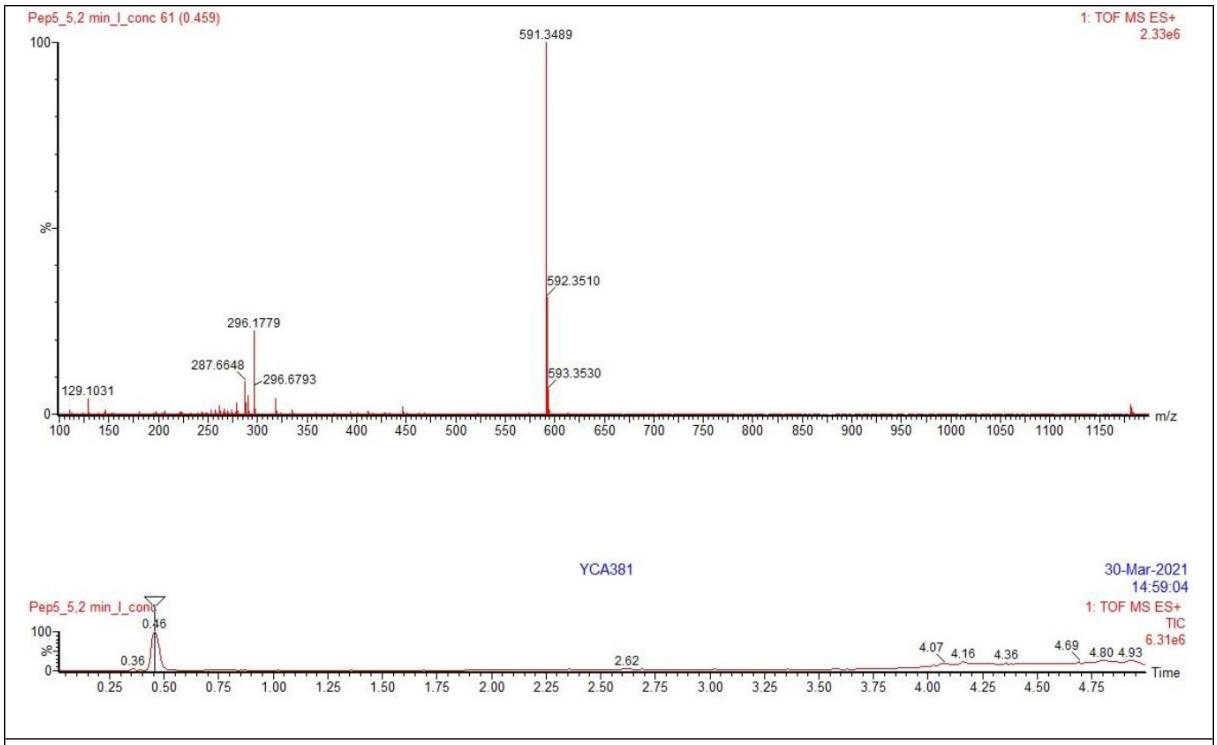

Figure S16. (Top) After semi-preparative RP-HPLC purification, mass spectrum of **e** in a *m/z* range of 100 – 1200 *m/z* collected *via* a LC-MS measurement. (Below) The corresponding total ion current (TIC) chromatogram. H_2O was used for LC-MS sample dilution.

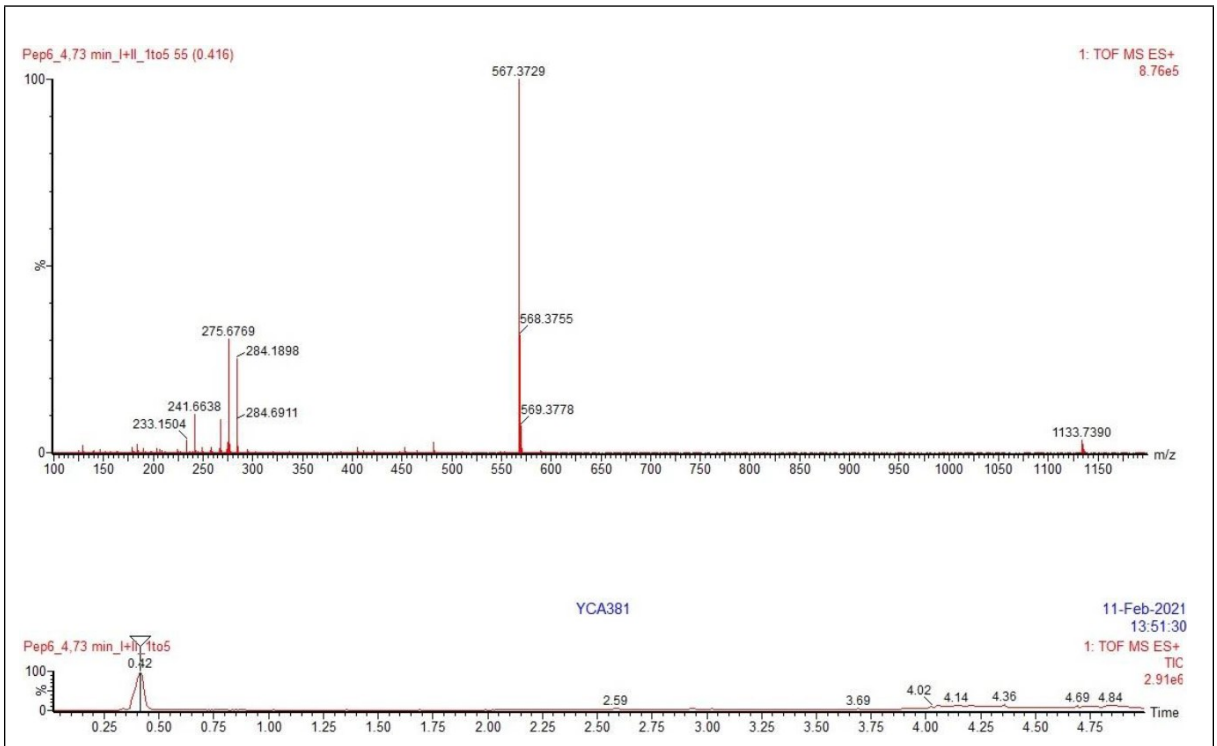

Figure S17. (Top) After semi-preparative RP-HPLC purification, mass spectrum of **f** in a *m/z* range of 100 – 1200 *m/z* collected *via* a LC-MS measurement. (Below) The corresponding total ion current (TIC) chromatogram. H_2O was used for LC-MS sample dilution.

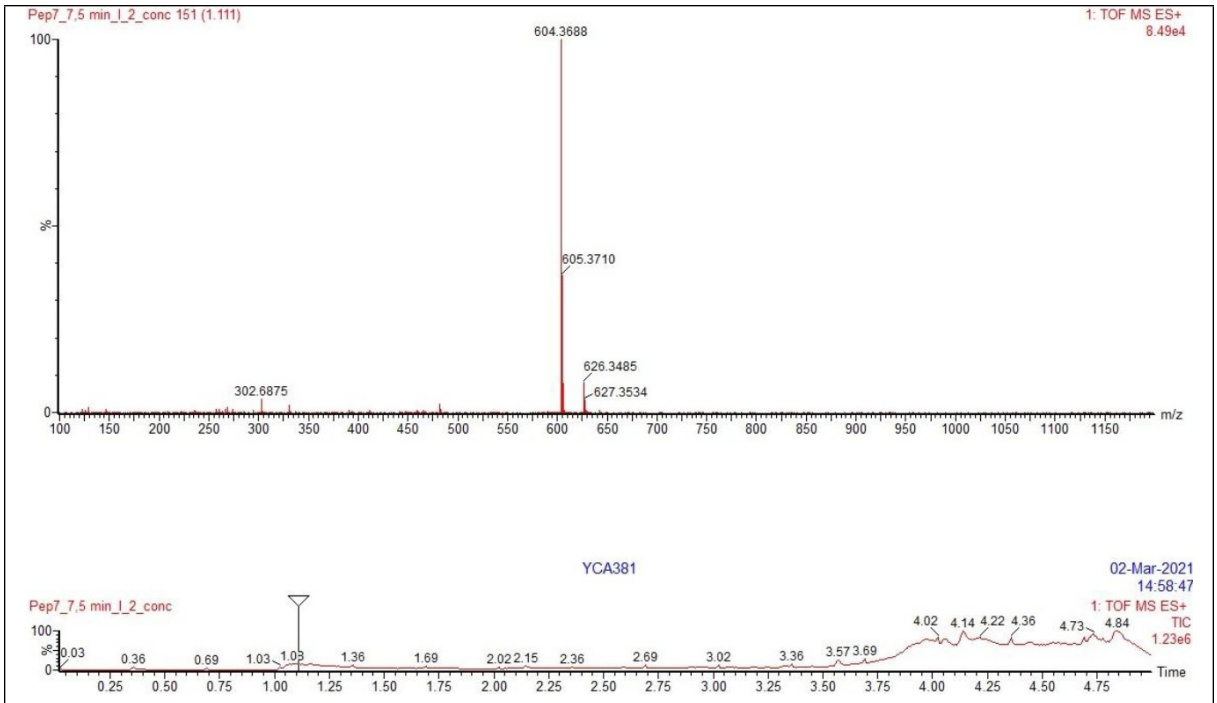

Figure S18. (Top) After semi-preparative RP-HPLC purification, mass spectrum of **g** in a *m/z* range of 100 – 1200 *m/z* collected *via* a LC-MS measurement. (Below) The corresponding total ion current (TIC) chromatogram. H_2O was used for LC-MS sample dilution.

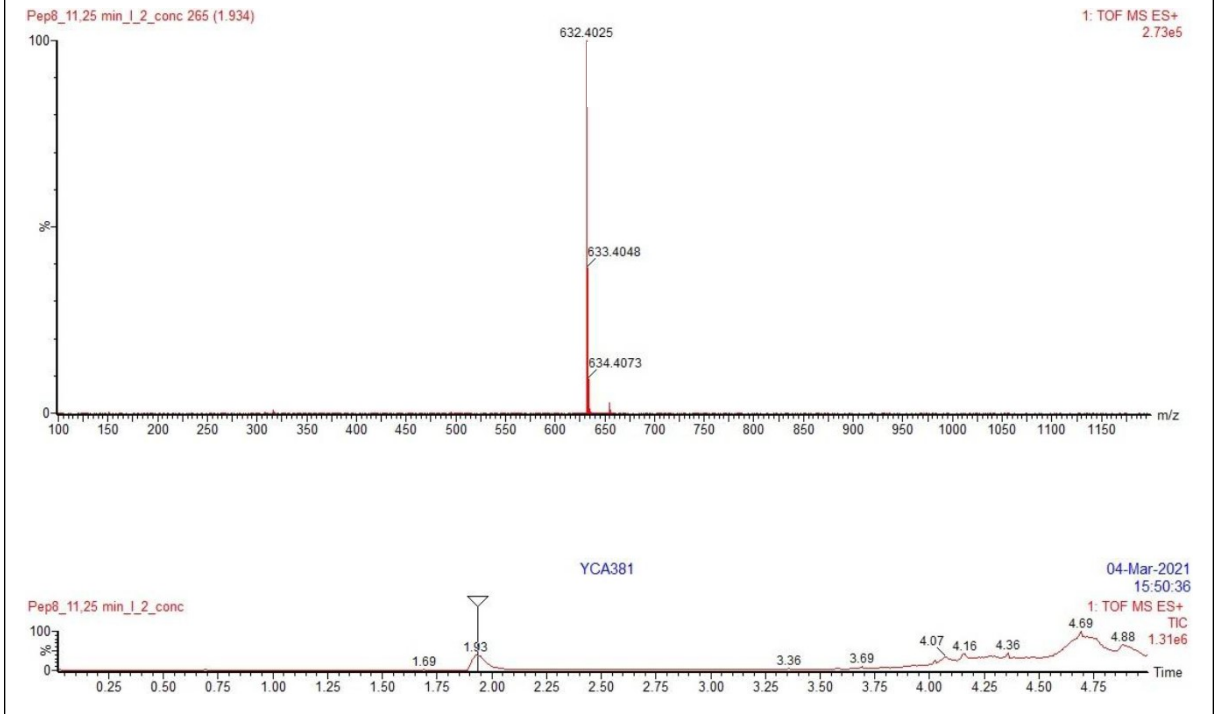

Figure S19. (Top) After semi-preparative RP-HPLC purification, mass spectrum of **h** in a *m/z* range of 100 – 1200 *m/z* collected *via* a LC-MS measurement. (Below) The corresponding total ion current (TIC) chromatogram. H_2O was used for LC-MS sample dilution.

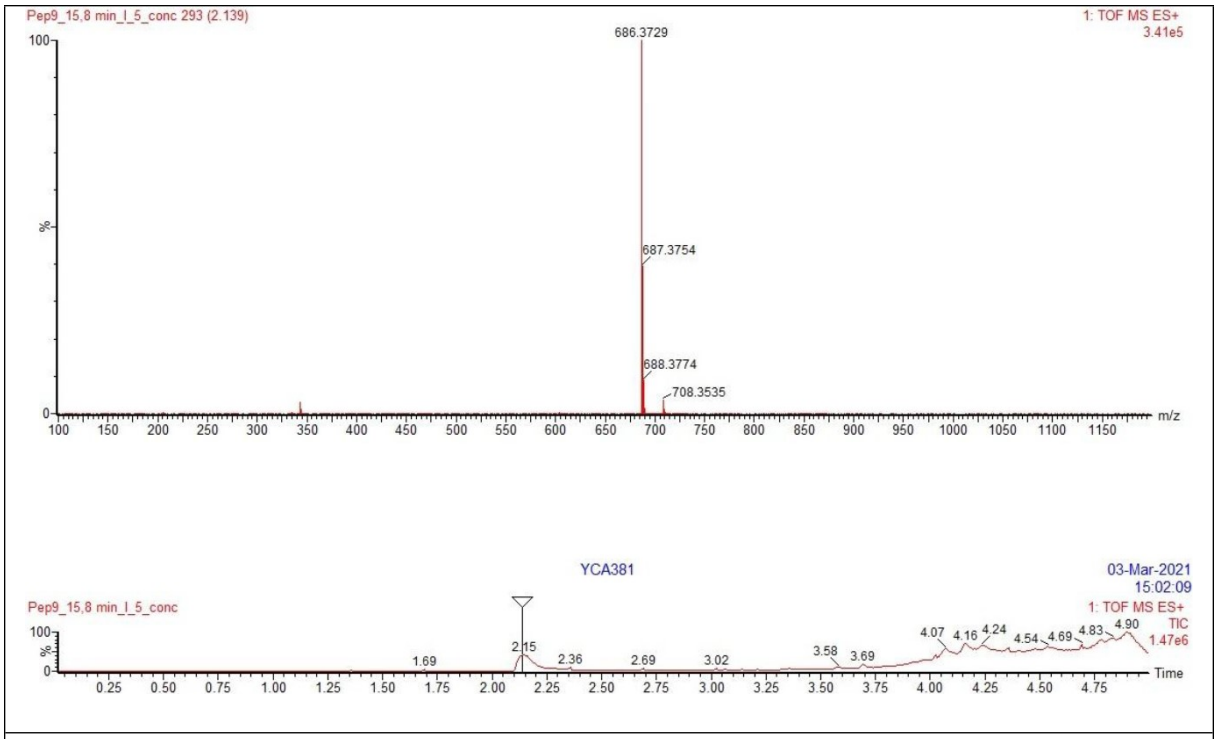

Figure S20. (Top) After semi-preparative RP-HPLC purification, mass spectrum of **i** in a *m*/*z* range of 100 – 1200 *m/z* collected *via* a LC-MS measurement. (Below) The corresponding total ion current (TIC) chromatogram. H_2O was used for LC-MS sample dilution.

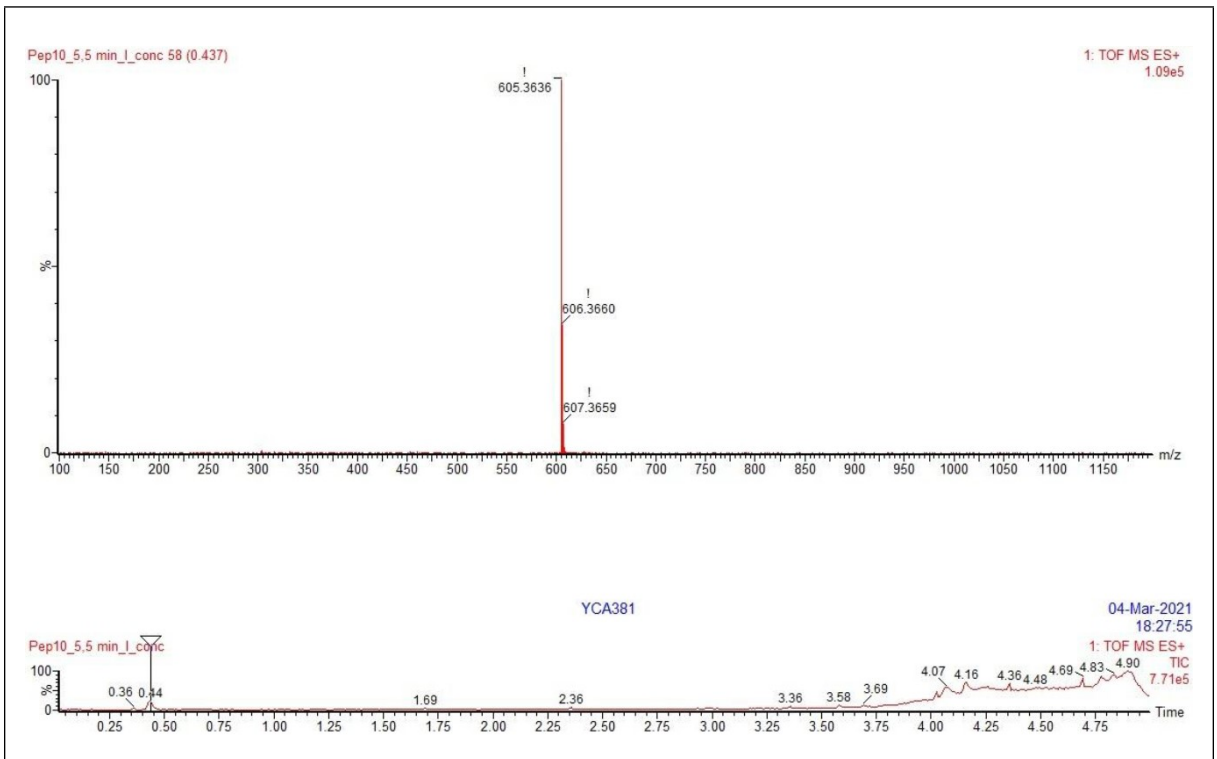

Figure S21. (Top) After semi-preparative RP-HPLC purification, mass spectrum of **j** in a *m*/*z* range of 100 – 1200 *m/z* collected *via* a LC-MS measurement. (Below) The corresponding total ion current (TIC) chromatogram. H_2O was used for LC-MS sample dilution.

S-3 Determination of peptide yields

The synthesized peptides **a**–**j** are protonated to an uncertain extent during RP-HPLC purification, resulting in an undefined composition of the peptide trifluoroacetate salt (ratio peptide : trifluoroacetate counterion). Thus, just weighing the peptide for yield determination is inaccurate. UV/VIS spectroscopy was used for adjusting the actual yield based on the known d-d transition bands of Cu(II) complexes with ligands of the type NH_2-Gly-Gly-His (5,5,6-membered chelates; λ_{max} = 525 nm[2]), NH_2-Gly-β-Ala-His (5,6,6; λ_{max} = 545 nm[3]), NH_2-β-Ala-β-Ala-His (6,6,6; λ_{max} =670 nm[4]) and the latter with pyrazolyl/triazolyl units at the N-terminus (6,6,6; λ_{max} = 605/670 nm [4]). λ_{max} values of complexes **1**–**10** are in these ranges (*vide infra*).

Based on the weighing result, a 2 mM peptide solution of **a**–**j** (1 eq.) was prepared in 50 mM MOPS buffer (pH 7.4) and treated with $CuCl_2 \cdot 2\ H_2O$ in 0.1 mM steps (0.05 eq.). The d-d transition bands of the corresponding Cu(II) complexes **1**–**10** were monitored by UV/VIS spectroscopy. The saturation point of the forming d-d transition bands for each Cu(II) ATCUN complex was utilized for recalculating the actual yield. The adjusted yield for the peptides **a**–**j** and the absorption maxima of the d-d transition for their Cu(II) complexes **1**–**10** are listed in Table S3. The UV/VIS spectra in the range 400–800 nm of the Cu(II) peptide titrations are shown in Figures S22-S31.

Table S3. Yield by weighing and adjusted/actual yield of the synthesized peptides **a**–**j**, saturation points in equiv. of the d-d transition band detected upon treatment of the peptides with $CuCl_2 \cdot 2\ H_2O$ in 0.05 eq. steps and λ_{max} of d-d transition of the corresponding Cu(II) ATCUN-based complexes **1**–**10**.

peptide	saturation point [eq.]	adjusted/actual yield [%]	yield by weighing [%]	complex	λ_{max} of d-d transition band [nm]
a	0.70	37.29	53.26	**1**	567
b	0.75	30.77	41.02	**2**	571
c	0.75	36.56	48.74	**3**	545
d	0.75	19.43	25.91	**4**	582
e	0.80	35.62	44.52	**5**	597
f	0.40	16.34	40.85	**6**	632
g	0.40	16.84	42.11	**7**	635
h	0.35	13.13	37.51	**8**	627
i	0.30	6.73	22.43	**9**	630
j	0.35	18.80	53.71	**10**	645

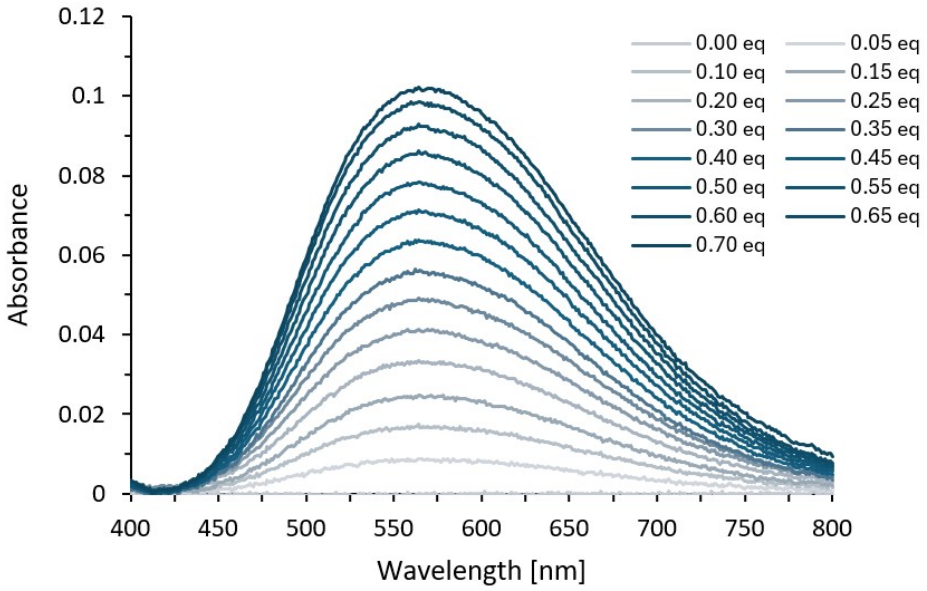

Figure S22. UV/VIS spectra in the range 400 – 800 nm of 2 mM peptide **a** with increasing concentrations of $CuCl_2$ (0.1 mM, 0.05 eq.) visualizing the d-d transition at λ_{max} = 567 nm of the forming Cu(II) ATCUN-based complex **1**. The saturation point is 0.70 eq. and was used to adjust the inaccurate peptide yield determined by weighing.

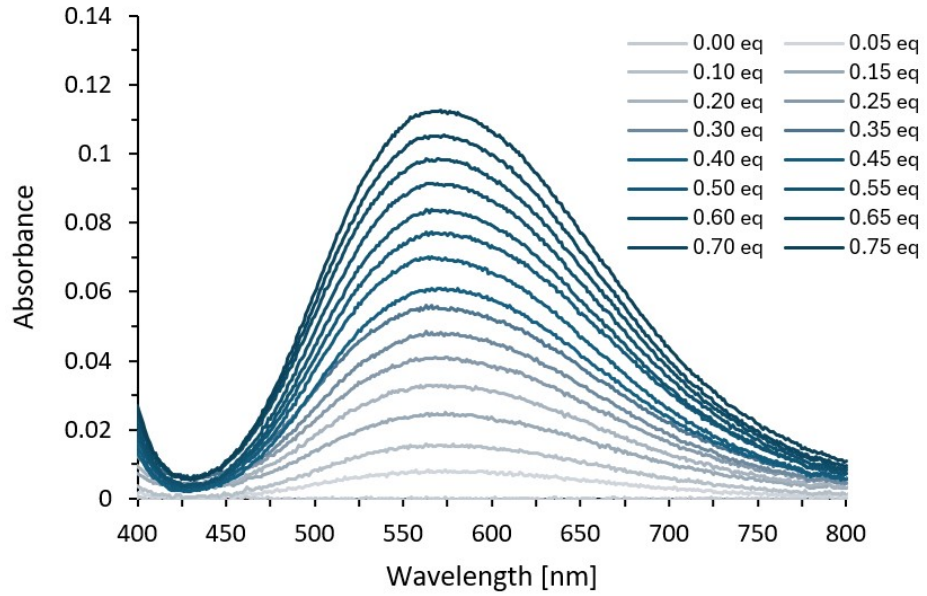

Figure S23. UV/VIS spectra in the range 400 – 800 nm of 2 mM peptide **b** with increasing concentrations of $CuCl_2$ (0.1 mM, 0.05 eq.) visualizing the d-d transition at λ_{max} = 571 nm of the forming Cu(II) ATCUN-based complex **2**. The saturation point is 0.75 eq. and was used to adjust the inaccurate peptide yield determined by weighing.

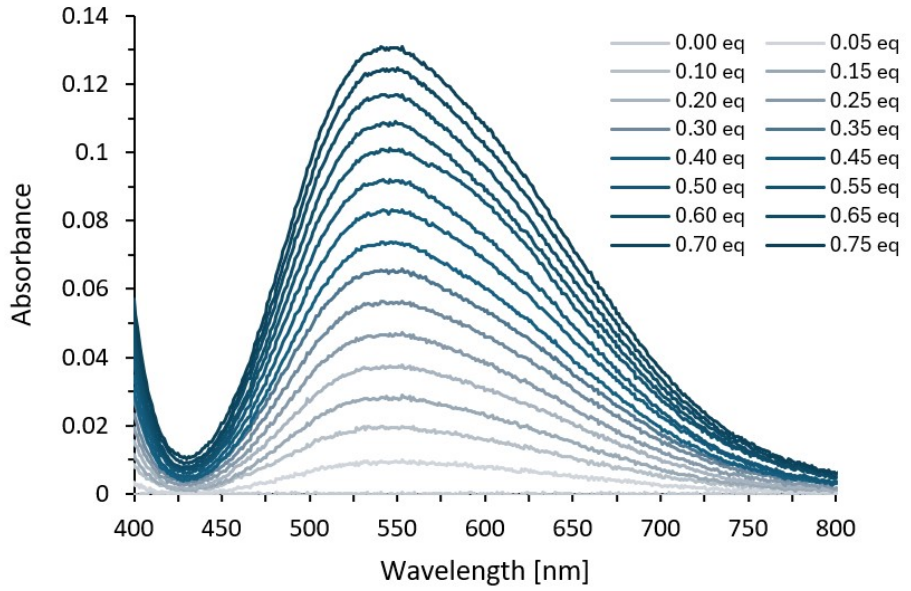

Figure S24. UV/VIS spectra in the range 400 – 800 nm of 2 mM peptide **c** with increasing concentrations of $CuCl_2$ (0.1 mM, 0.05 eq.) visualizing the d-d transition at λ_{max} = 545 nm of the forming Cu(II) ATCUN-based complex **3**. The saturation point is 0.75 eq. and was used to adjust the inaccurate peptide yield determined by weighing.

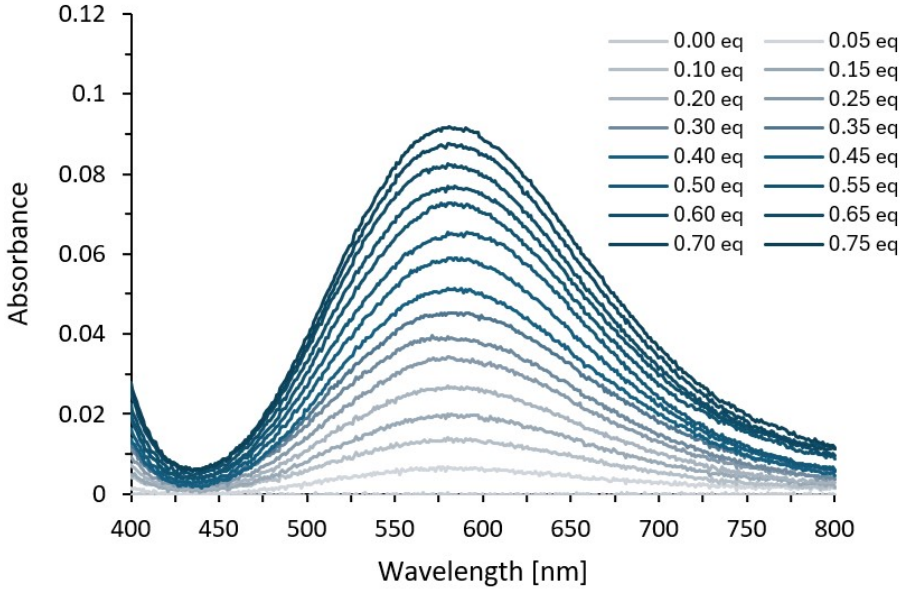

Figure S25. UV/VIS spectra in the range 400 – 800 nm of 2 mM peptide **d** with increasing concentrations of $CuCl_2$ (0.1 mM, 0.05 eq.) visualizing the d-d transition at λ_{max} = 582 nm of the forming Cu(II) ATCUN-based complex **4**. The saturation point is 0.75 eq. and was used to adjust the inaccurate peptide yield determined by weighing.

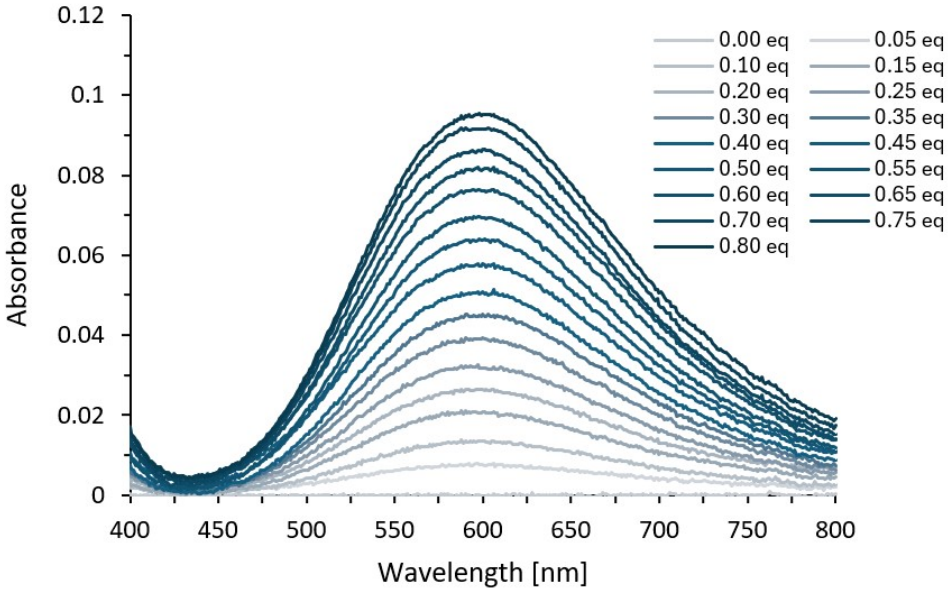

Figure S26. UV/VIS spectra in the range 400 – 800 nm of 2 mM peptide **e** with increasing concentrations of $CuCl_2$ (0.1 mM, 0.05 eq.) visualizing the d-d transition at λ_{max} = 597 nm of the forming Cu(II) ATCUN-based complex **5**. The saturation point is 0.80 eq. and was used to adjust the inaccurate peptide yield determined by weighing.

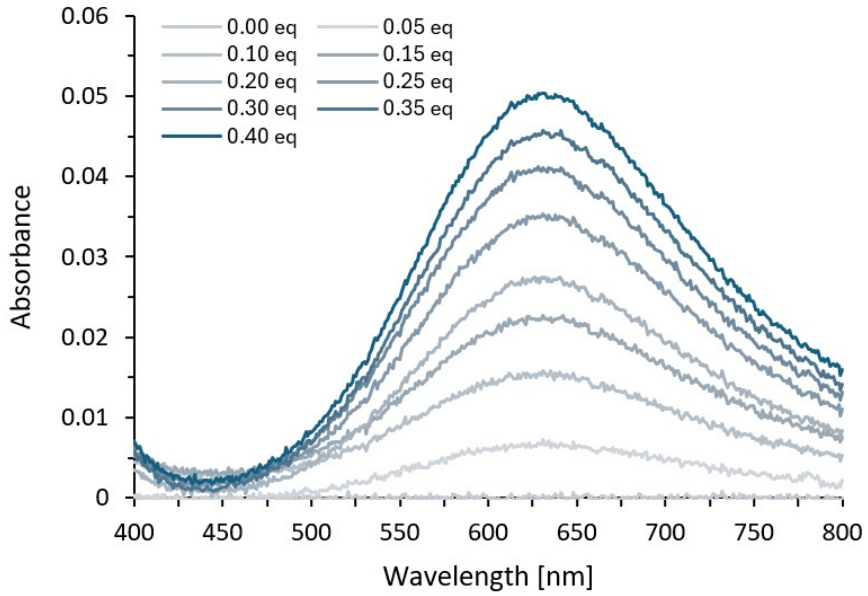

Figure S27. UV/VIS spectra in the range 400 – 800 nm of 2 mM peptide **f** with increasing concentrations of $CuCl_2$ (0.1 mM, 0.05 eq.) visualizing the d-d transition at λ_{max} = 632 nm of the forming Cu(II) ATCUN-based complex **6**. The saturation point is 0.40 eq. and was used to adjust the inaccurate peptide yield determined by weighing.

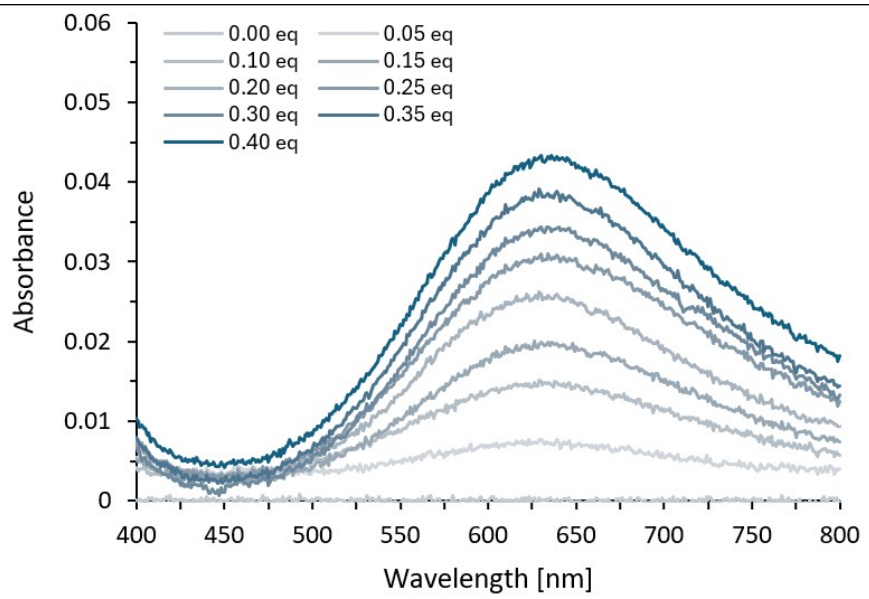

Figure S28. UV/VIS spectra in the range 400 – 800 nm of 2 mM peptide **g** with increasing concentrations of $CuCl_2$ (0.1 mM, 0.05 eq.) visualizing the d-d transition at λ_{max} = 635 nm of the forming Cu(II) ATCUN-based complex **7**. The saturation point is 0.40 eq. and was used to adjust the inaccurate peptide yield determined by weighing.

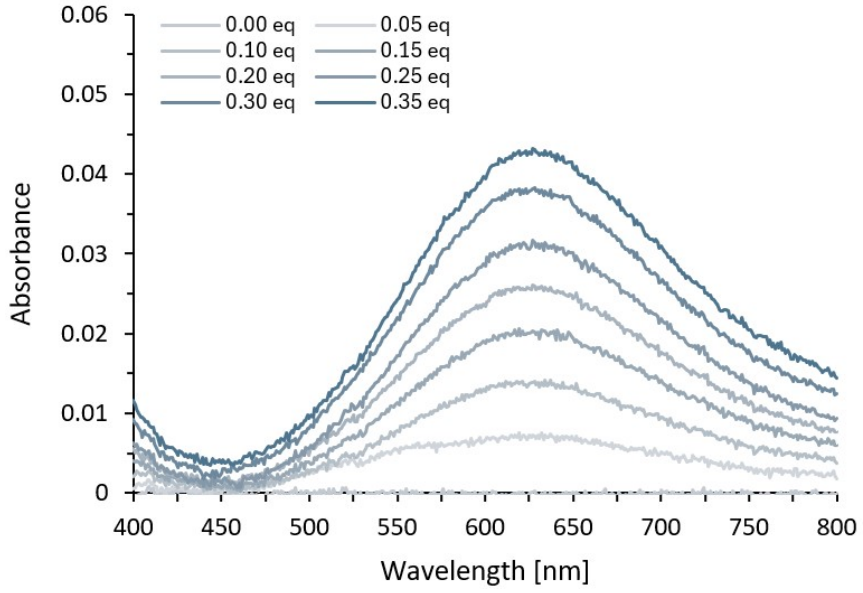

Figure S29. UV/VIS spectra in the range 400 – 800 nm of 2 mM peptide **h** with increasing concentrations of $CuCl_2$ (0.1 mM, 0.05 eq.) visualizing the d-d transition at λ_{max} = 627 nm of the forming Cu(II) ATCUN-based complex **8**. The saturation point is 0.35 eq. and was used to adjust the inaccurate peptide yield determined by weighing.

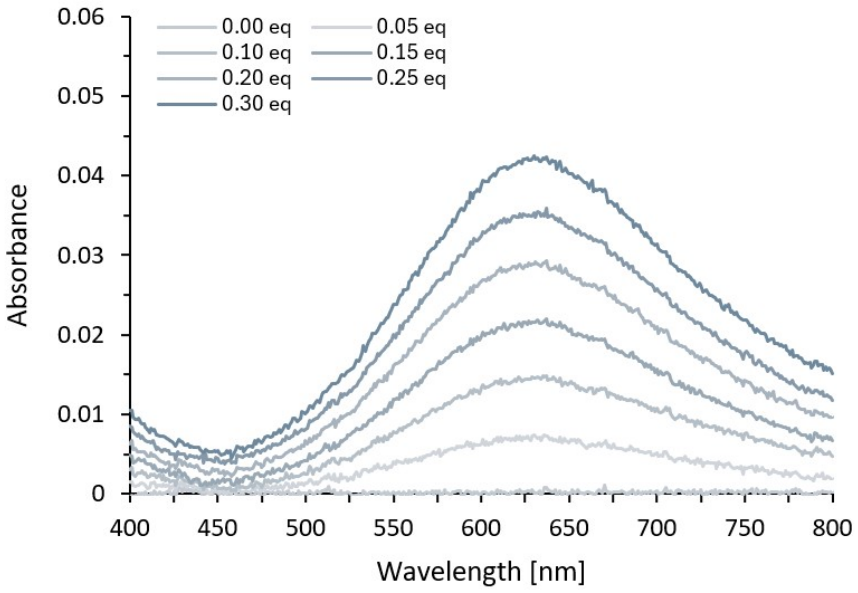

Figure S30. UV/VIS spectra in the range 400 – 800 nm of 2 mM peptide **i** with increasing concentrations of $CuCl_2$ (0.1 mM, 0.05 eq.) visualizing the d-d transition at λ_{max} = 630 nm of the forming Cu(II) ATCUN-based complex **9**. The saturation point is 0.30 eq. and was used to adjust the inaccurate peptide yield determined by weighing.

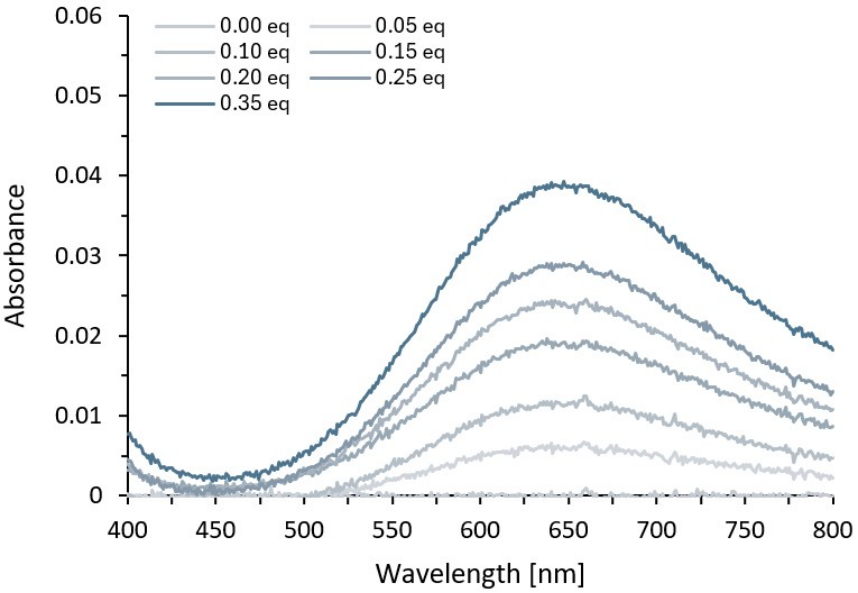

Figure S31. UV/VIS spectra in the range 400 – 800 nm of 2 mM peptide **j** with increasing concentrations of $CuCl_2$ (0.1 mM, 0.05 eq.) visualizing the d-d transition at λ_{max} = 645 nm of the forming Cu(II) ATCUN-based complex **10**. The saturation point is 0.35 eq. and was used to adjust the inaccurate peptide yield determined by weighing.

Table S4. Summarized data set of Cu(II) ATCUN-based complexes **1**–**10** and previously studied metallopeptides[4] regarding their chelate ring sizes, N-termini, Cu binding modes and d-d transition bands.

compound	**chelate ring sizes**	**N-terminus**	**Cu(II)-N binding mode**	**λ_{max} of d-d transition band [nm]**
1	7,5,6	amine	4N	567
2	7,5,6	pyrazolyl	4N	571
3	7,5,6	3-CH_3-5-CH_3-pyrazolyl	4N	545
4	7,5,6	3-CF_3-5-CH_3-pyrazolyl	4N	582
5	7,5,6	triazolyl	4N	597
6	7,6,6	amine	4N	632
7	7,6,6	pyrazolyl	4N	635
8	7,6,6	3-CH_3-5-CH_3-pyrazolyl	4N	627
9	7,6,6	3-CF_3-5-CH_3-pyrazolyl	4N	630
10	7,6,6	triazolyl	4N	645
previous work	5,5,6	amine	4N	≈ 525
previous work	6,5,6	amine	3N or 4N	≈ 540
previous work	5,6,6	amine	3N or 4N	≈ 555
previous work	6,6,6	amine	2N	≈ 670
previous work	6,6,6	pyrazolyl	3N or 4N	604
previous work	6,6,6	triazolyl	2N	≈ 670

S-4 Computational Details and Results

Structures of the copper ATCUN complexes were minimized using the GFN2-xTB Hamiltonian[5] with XTB v. 6.4.0 using an ALPB solvent model for water. The conformational space of complexes **1-10** was systematically explored using the Conformer-Rotamer Ensemble-Tool (CREST)[6] with GFN2-xTB (ALPB) and default settings for structural (RMSD), energy (threshold < 6 kcal/mol), and rotational constant B features to remove duplicates. Finally, the set of unique conformers was re-optimized with tighter thresholds. The global minima were then structurally minimized at the BP86-D3(BJ)/def2-TZVP (COSMO, water) level of theory with Turbomole v. 7.5.1.[7]

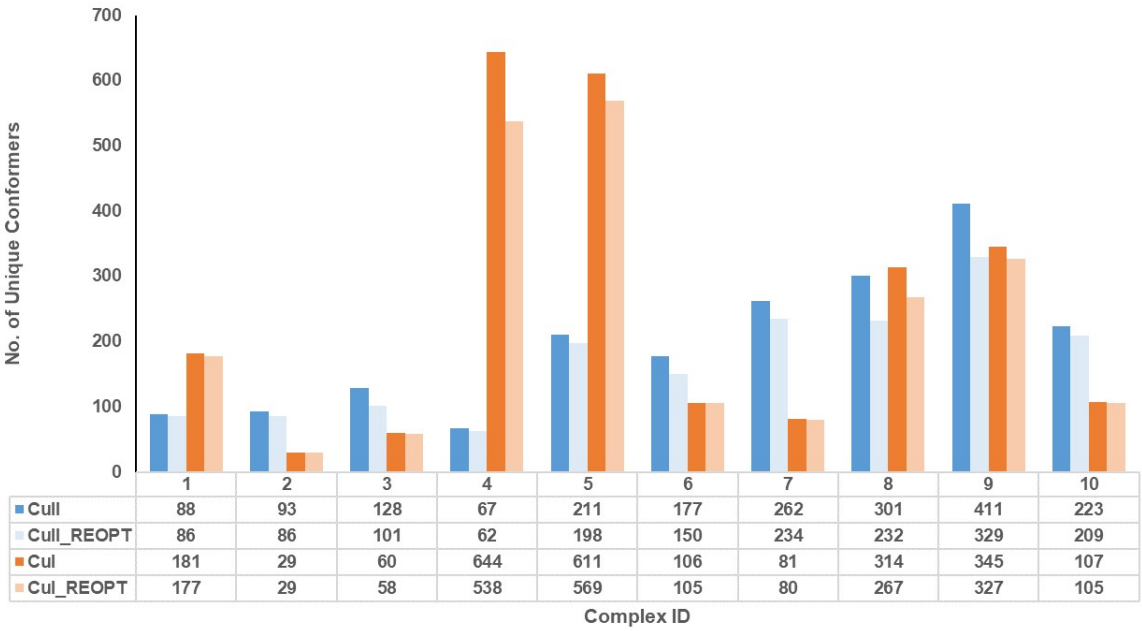

	1	2	3	4	5	6	7	8	9	10
CuII	88	93	128	67	211	177	262	301	411	223
CuII_REOPT	86	86	101	62	198	150	234	232	329	209
CuI	181	29	60	644	611	106	81	314	345	107
CuI_REOPT	177	29	58	538	569	105	80	267	327	105

Figure S32. Number of unique conformers for complexes **1**-**10** in Cu(II) and Cu(I) oxidation states from conformational searches at GFN2-xTB level.

Table S5. Different coordination modes of ATCUN-based peptides **1-10** in Cu(II) and Cu(I) oxidation states from CREST GFN2-xTB. Lowest energy structure refined by BP86-D3(BJ)/def2-TZVP (COSMO) calculations.

compound	**1**	**2**	**3**	**4**	**5**	**6**	**7**	**8**	**9**	**10**
for Cu(II)	4N	4N	4N	4N	4N	4N	4N	4N	4N	4N
for Cu(I)	3N	4N	4N	3N	3N	3N	4N	3N	3N	4N

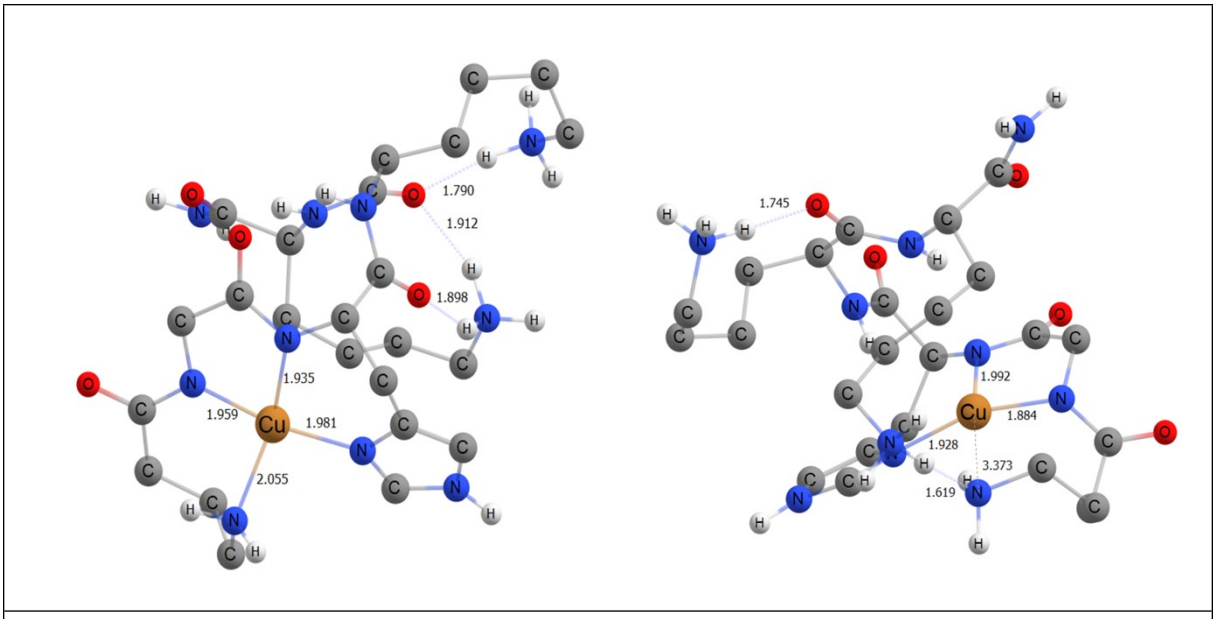

Figure S33. Cu(II) and Cu(I) complex structures of Gly compound **1** (7,5,6 chelates; terminal NH_2). Lowest energy structure from GFN2-xTB CREST re-optimized with DFT (BP86-D3(BJ)/def2-TZVP (COSMO). For Cu(II) (left) an ATCUN-like 4N binding (distorted square planar) and for Cu(I) (right) a 3N binding mode (distorted tetrahedral) is present.

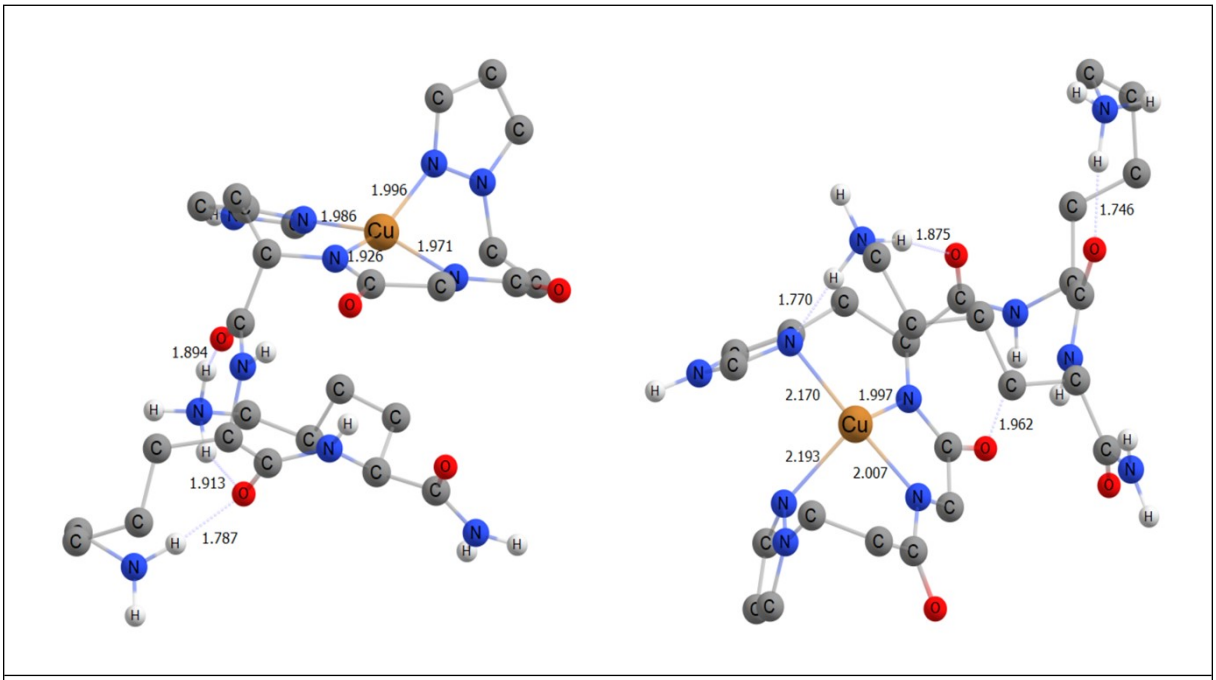

Figure S34. Cu(II) and Cu(I) complex structures of Gly compound **2** (7,5,6 chelates; terminal NH_2). Lowest energy structure from GFN2-xTB CREST re-optimized with DFT (BP86-D3(BJ)/def2-TZVP (COSMO). For Cu(II) (left) and Cu(I) (right) an ATCUN-like 4N binding mode (distorted square planar) is present.

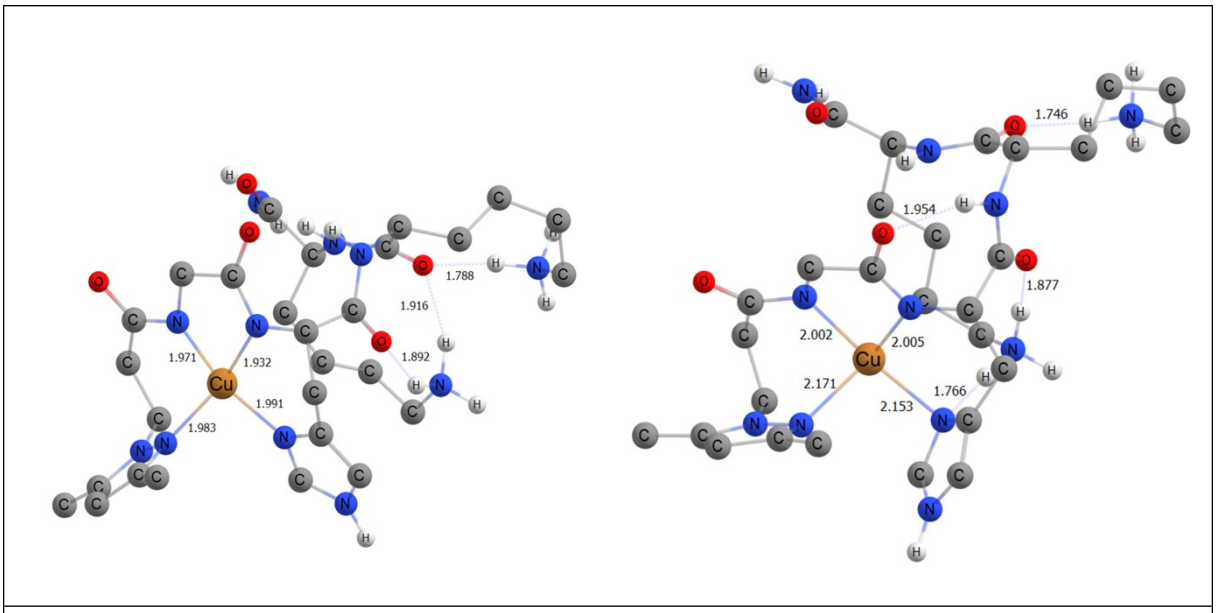

Figure S35. Cu(II) and Cu(I) complex structures of Gly compound **3** (7,5,6 chelates; terminal NH_2). Lowest energy structure from GFN2-xTB CREST re-optimized with DFT (BP86-D3(BJ)/def2-TZVP (COSMO). For Cu(II) (left) and Cu(I) (right) an ATCUN-like 4N binding mode (distorted square planar) is present.

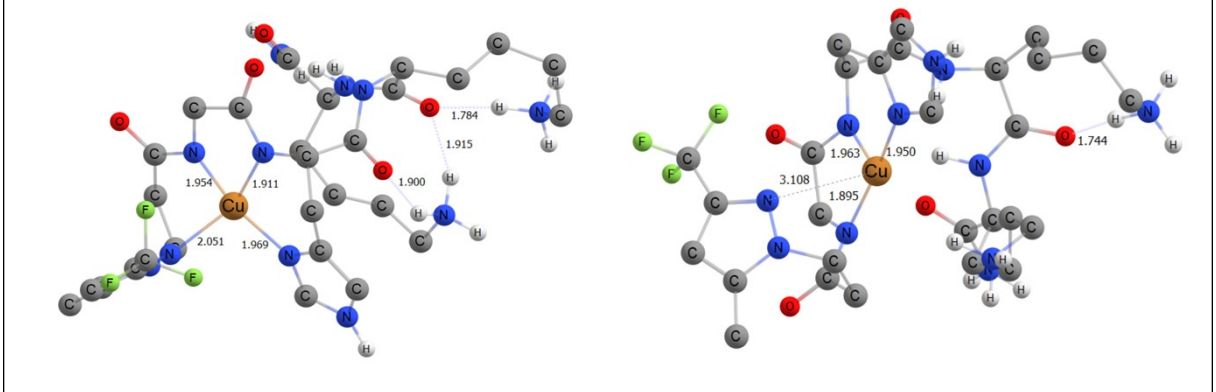

Figure S36. Cu(II) and Cu(I) complex structures of Gly compound **4** (7,5,6 chelates; terminal NH_2). Lowest energy structure from GFN2-xTB CREST re-optimized with DFT (BP86-D3(BJ)/def2-TZVP (COSMO). For Cu(II) (left) an ATCUN-like 4N binding (distorted square planar) and for Cu(I) (right) a 3N binding mode (distorted tetrahedral) is present.

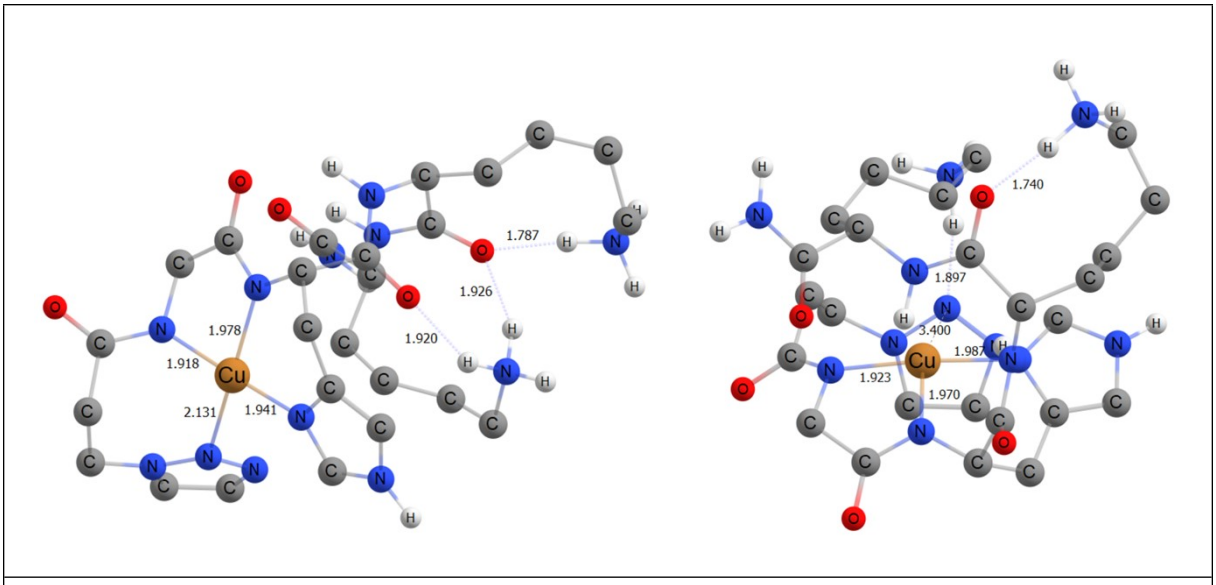

Figure S37. Cu(II) and Cu(I) complex structures of Gly compound **5** (7,5,6 chelates; terminal NH_2). Lowest energy structure from GFN2-xTB CREST re-optimized with DFT (BP86-D3(BJ)/def2-TZVP (COSMO). For Cu(II) (left) an ATCUN-like 4N binding (distorted square planar) and for Cu(I) (right) a 3N binding mode (distorted tetrahedral) is present.

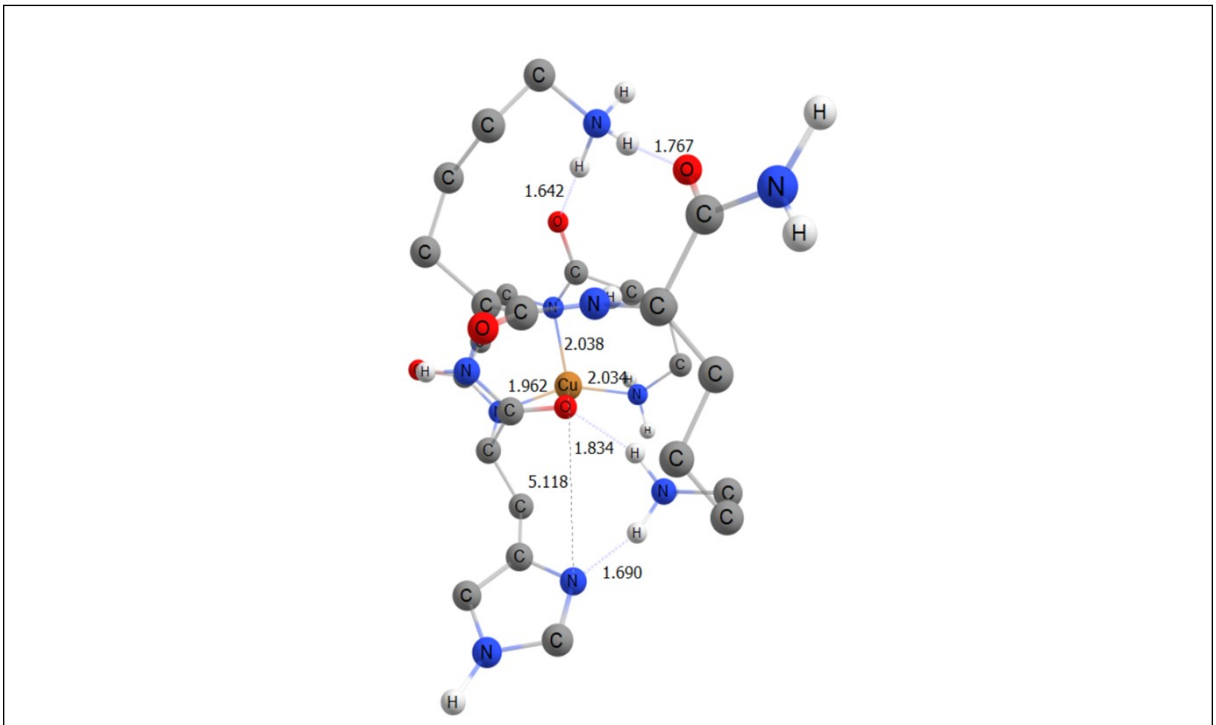

Figure S38. Cu(I) complex structure of β-Ala compound **6** (7,6,6 chelates; terminal NH_2). Lowest energy structure from GFN2-xTB CREST re-optimized with DFT (BP86-D3(BJ)/def2-TZVP (COSMO). For Cu(I) a 3N binding mode (distorted tetrahedral) present.

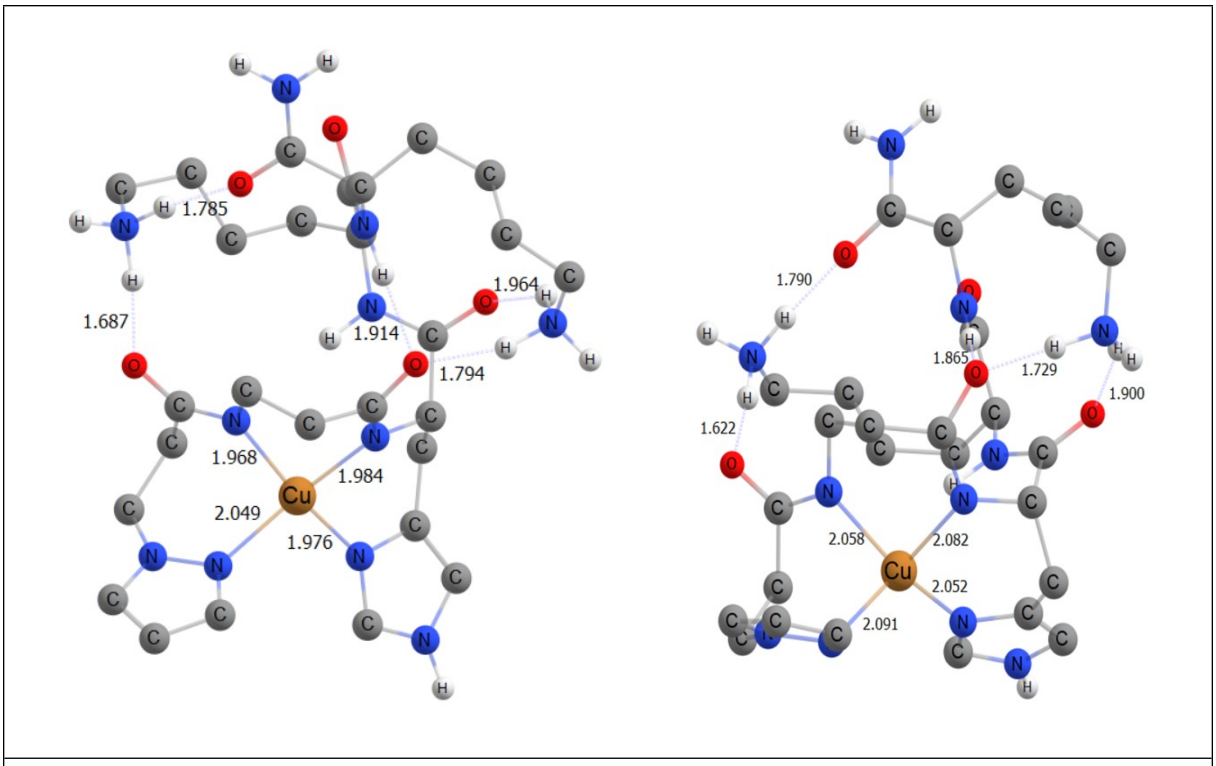

Figure S39. Cu(II) and Cu(I) complex structures of β-Ala compound **7** (7,6,6 chelates; terminal NH_2). Lowest energy structure from GFN2-xTB CREST re-optimized with DFT (BP86-D3(BJ)/def2-TZVP (COSMO). For Cu(II) (left) and Cu(I) (right) an ATCUN-like 4N binding mode (distorted square planar) is present.

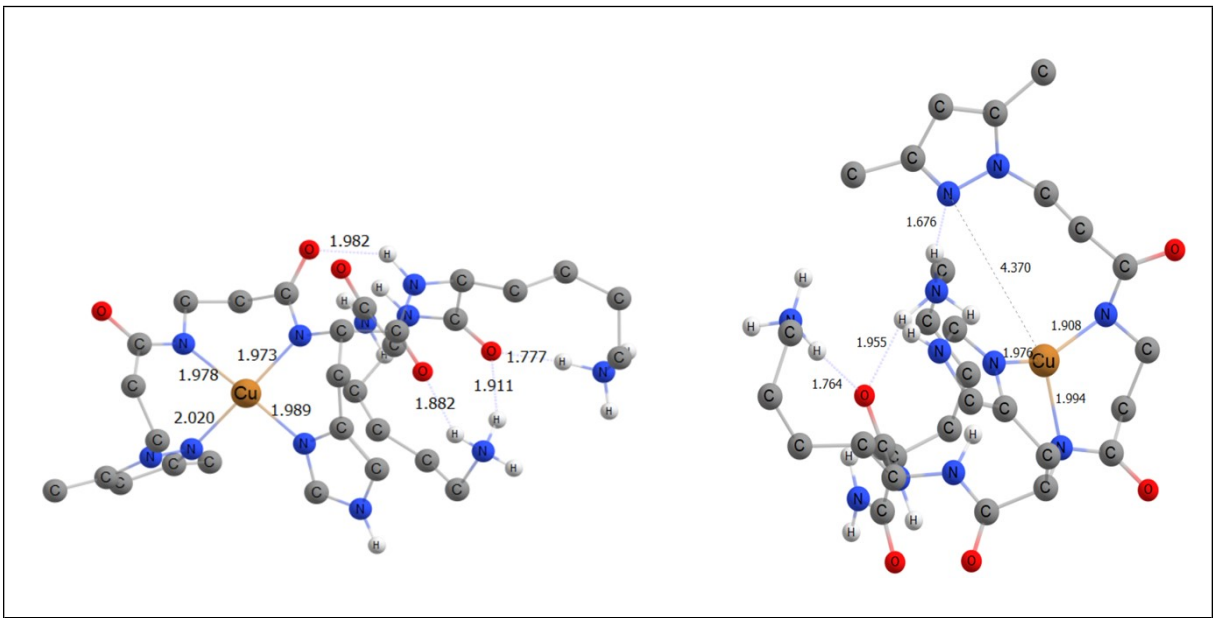

Figure S40. Cu(II) and Cu(I) complex structures of β-Ala compound **8** (7,6,6 chelates; terminal NH_2). Lowest energy structure from GFN2-xTB CREST re-optimized with DFT (BP86-D3(BJ)/def2-TZVP (COSMO). For Cu(II) (left) an ATCUN-like 4N binding (distorted square planar) and for Cu(I) (right) a 3N binding mode (distorted tetrahedral) is present.

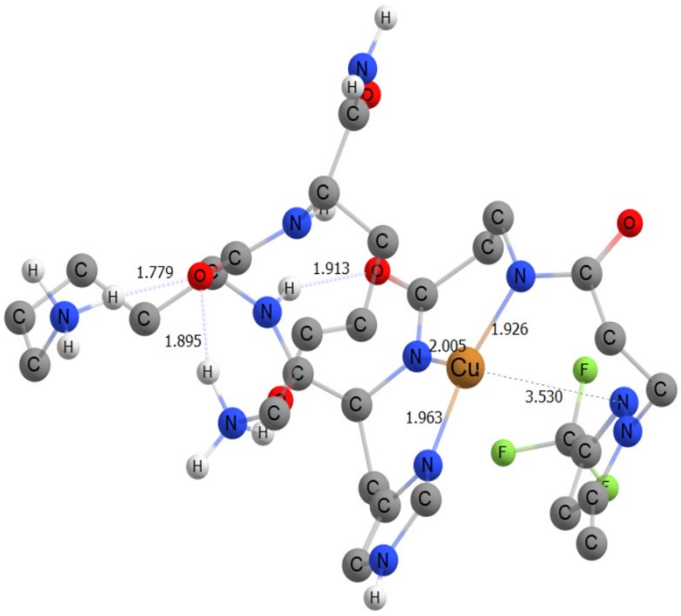

Figure S41. Cu(I) complex structures of β-Ala compound **9** (7,6,6 chelates; terminal NH_2). Lowest energy structure from GFN2-xTB CREST re-optimized with DFT (BP86-D3(BJ)/def2-TZVP (COSMO). For Cu(I) a 3N binding mode is seen (distorted tetrahedral).

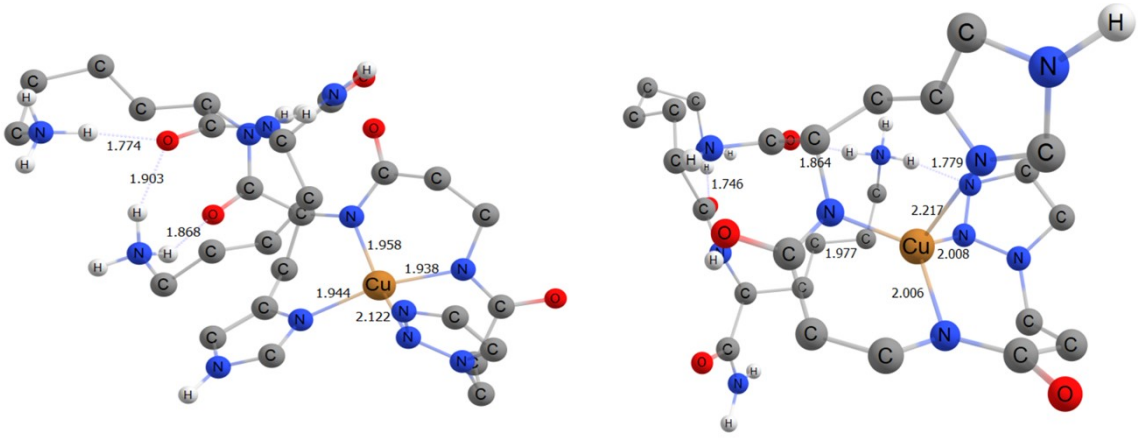

Figure S42. Cu(II) and Cu(I) complex structures of β-Ala compound **10** (7,6,6 chelates; terminal NH_2). Lowest energy structure from GFN2-xTB CREST re-optimized with DFT (BP86-D3(BJ)/def2-TZVP (COSMO). For Cu(II) (left) and Cu(I) (right) an ATCUN-like 4N binding mode (distorted square planar) is present.

S-5 *In situ* Cu(II) complex synthesis

If not stated otherwise, in DNA cleavage and ROS detection experiments (S-6 and S-7) Cu(II) ATCUN-based complex solutions (**1**–**10**) were prepared *in situ* as follows: 250 µL of a 2.5 mM peptide solution (**a**–**j**) and 250 µL of a 2 mM $CuCl_2$ solution were combined resulting in 500 µL of a 1 mM Cu(II) complex solution (Cu(II):peptide = 1:1.25).
For all DNA interaction experiments (DNA melting curves, EtBr displacement assay and CD spectroscopy) the final Cu(II):peptide ratio was 1:1.05 (a slightly lower ratio was used here to not additionally disturb the DNA binding affinity by applying an excess of chelator).
For DNA cleavage and binding studies as well as ROS detection, the *in situ* prepared Cu(II) ATCUN-based complex stock solutions were prepared in low concentrated HEPES buffer (5 mM, pH 7.4) to ensure complex formation before the actual experiment. Through dilution of these stock solutions for use in the above-mentioned experiments (50 mM HEPES buffer), the actual buffer concentration negligibly increased (50.25 mM).

ESI-MS:

The *in situ* prepared Cu(II) ATCUN complexes **1**–**10** were characterized by ESI-MS *via* an LC-MS system (*vide supra*). The calculated and found masses of the complexes are listed in Table S6. The ESI mass spectra are shown in Figures S43–S52.

Table S6. Calculated and found *m/z* values in HR ESI-MS of *in situ* prepared Cu(II) ATCUN-based complex solutions **1**-**10**. "L" stands for the corresponding peptide ligand **a**–**j**.

compound	**calculated:** **Cu(II): [Cu+L-H]$^+$** **Cu(I): [Cu+L]$^+$**	**found:** **Cu(II): [Cu+L-H]$^+$** **Cu(I): [Cu+L]$^+$**
1 (L = **a**)	614.2709 615.2787	614.2710 ---*
2 (L = **b**)	651.2661 652.2740	651.2664 652.2718
3 (L = **c**)	679.2974 680.3053	679.2978 680.3033
4 (L = **d**)	733.2692 734.2770	733.2687 734.2758
5 (L = **e**)	652.2614 653.2692	652.2607 653.2672
6 (L = **f**)	628.2865 629.2944	628.2889 629.2947
7 (L = **g**)	665.2818 666.2896	665.2806 666.2862
8 (L = **h**)	693.3131 694.3209	---* 694.3106

9 (L = **i**)	747.2848 748.2926	---* 748.2797
10 (L = **j**)	666.2770 667.2849	666.2689 667.2748

* not found under the used conditions.

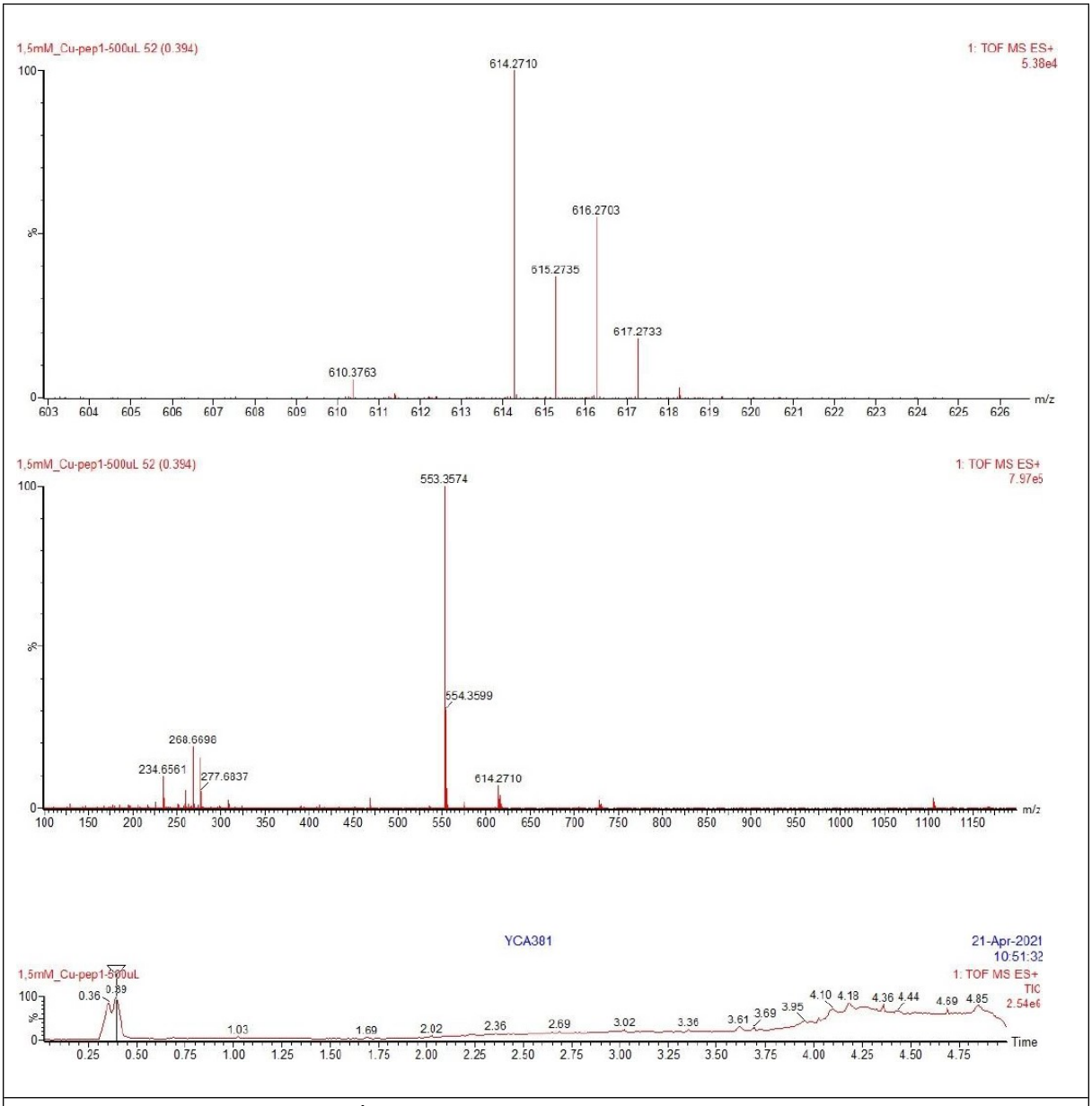

Figure S43. (Top) Zoom in (*m/z* 603 – 626) into (middle) the full range HR ESI mass spectrum (*m/z* 100 – 1200) of **1** after *in situ* preparation by combining solutions of **a** and $CuCl_2$. Dilution with MeCN. (Below) Total ion current (TIC) chromatogram (TIC) of the LC-MS measurement.

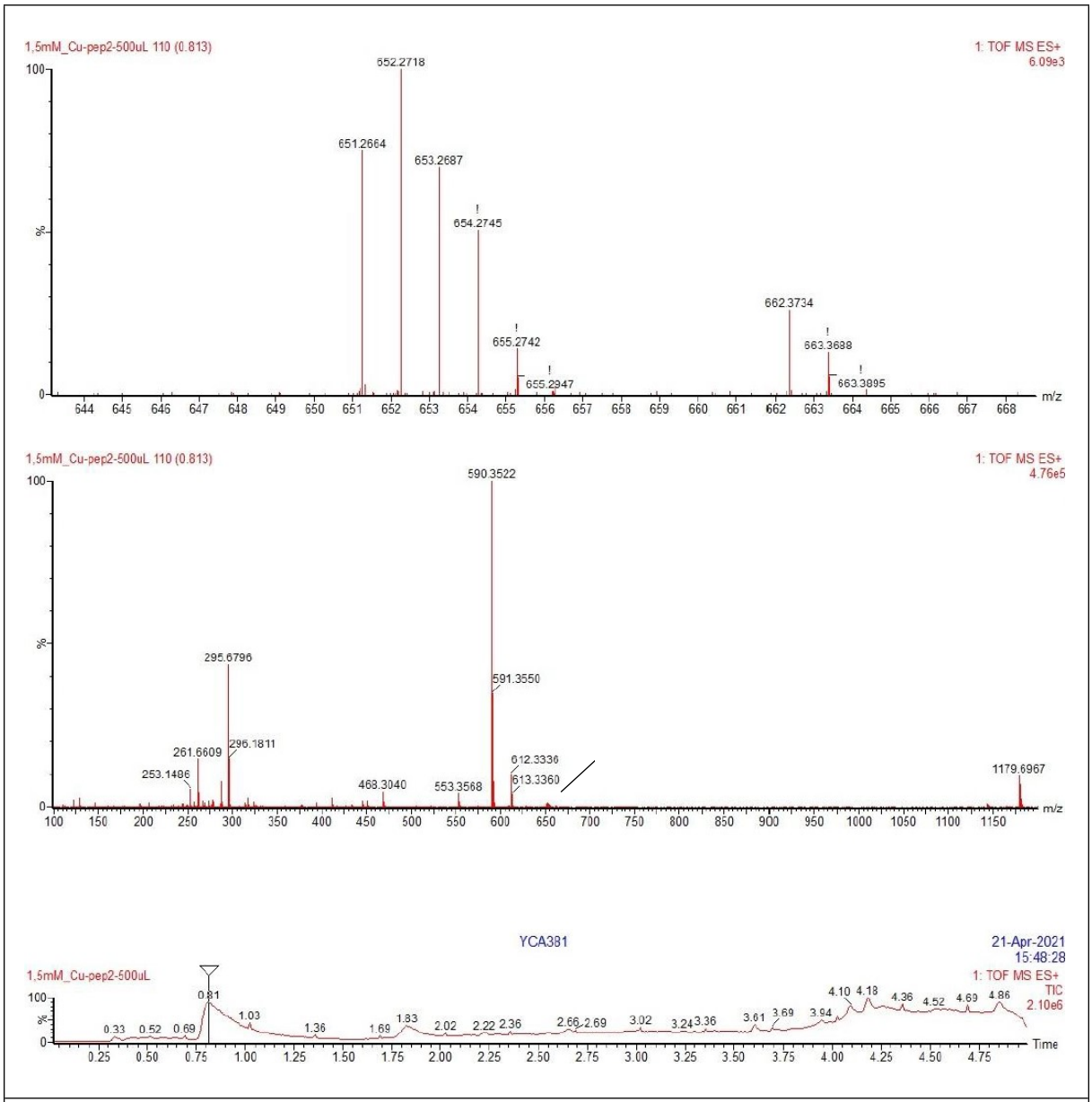

Figure S44. (Top) Zoom in (*m/z* 644 – 668) into (middle) the full range HR ESI mass spectrum (*m/z* 100 – 1200) of **2** after *in situ* preparation by combining solutions of **b** and $CuCl_2$. Dilution with MeCN. (Below) Total ion current (TIC) chromatogram of the LC-MS measurement.

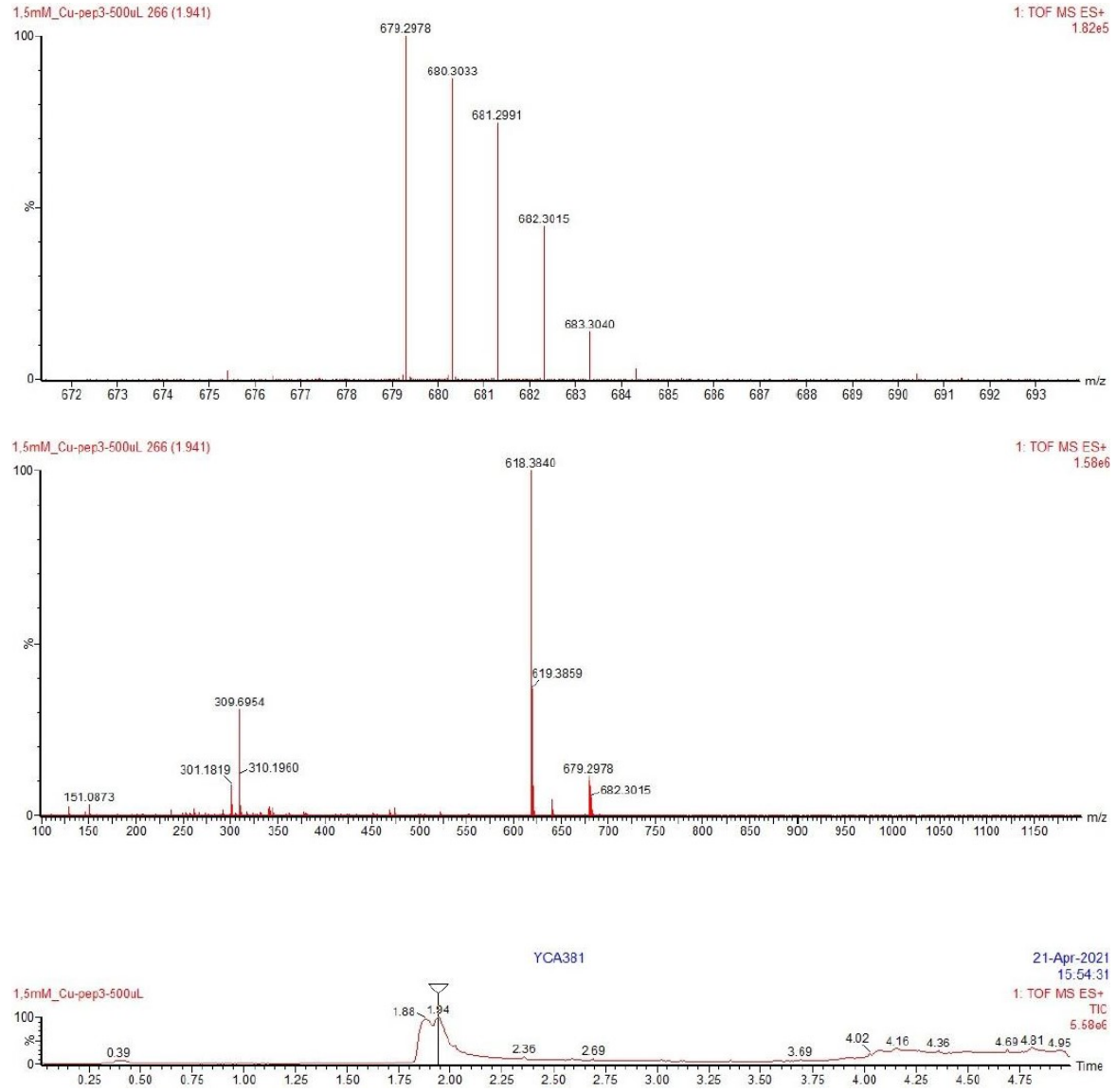

Figure S45. (Top) Zoom in (*m/z* 672 – 693) into (middle) the full range HR ESI mass spectrum (*m/z* 100 – 1200) of **3** after *in situ* preparation by combining solutions of **c** and $CuCl_2$. Dilution with MeCN. (Below) Total ion current (TIC) chromatogram of the LC-MS measurement.

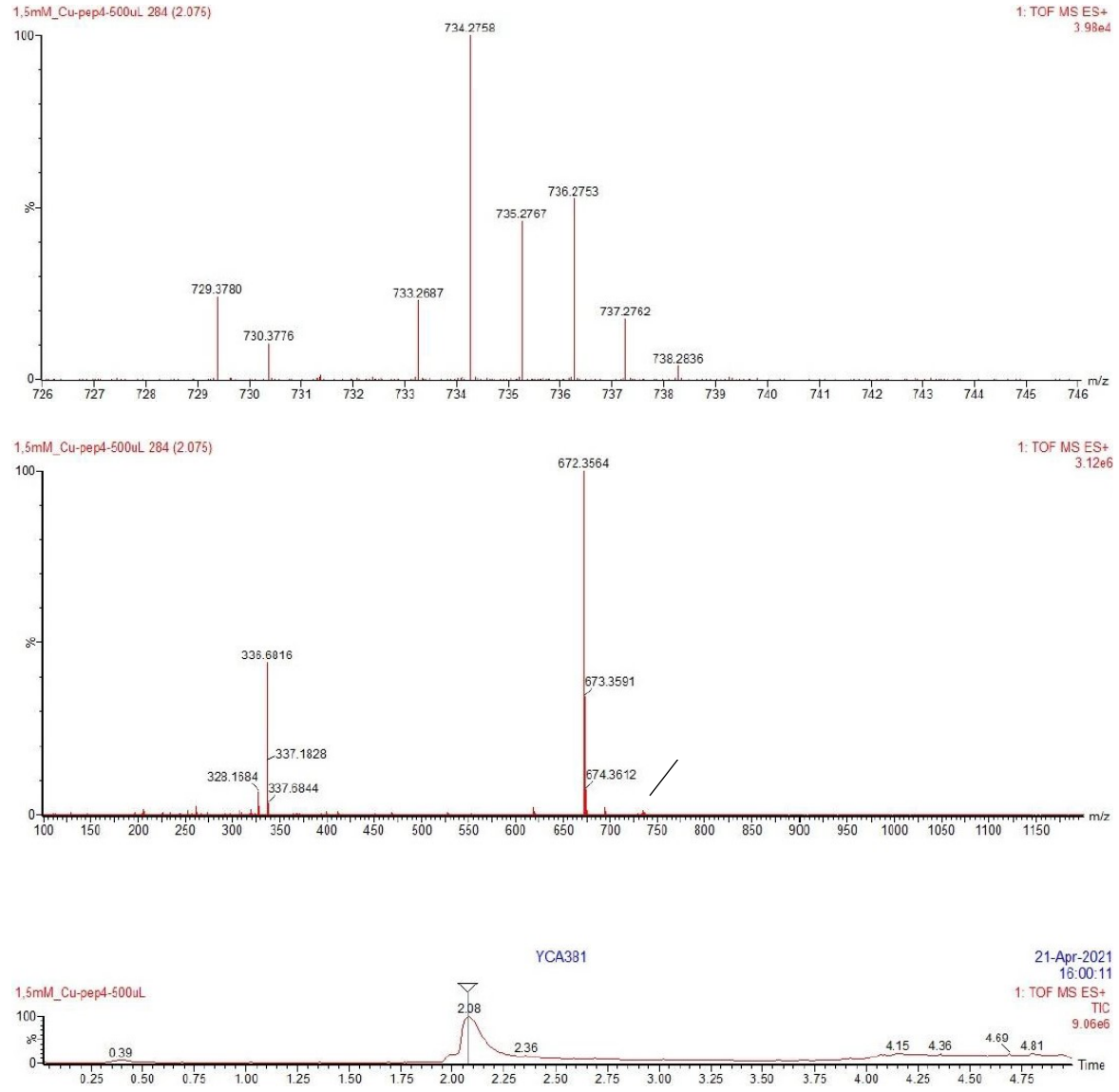

Figure S46. (Top) Zoom in (*m/z* 726 – 746) into (middle) the full range HR ESI mass spectrum (*m/z* 100 – 1200) of **4** after *in situ* preparation by combining solutions of **d** and $CuCl_2$. Dilution with MeCN. (Below) Total ion current (TIC) chromatogram of the LC-MS measurement.

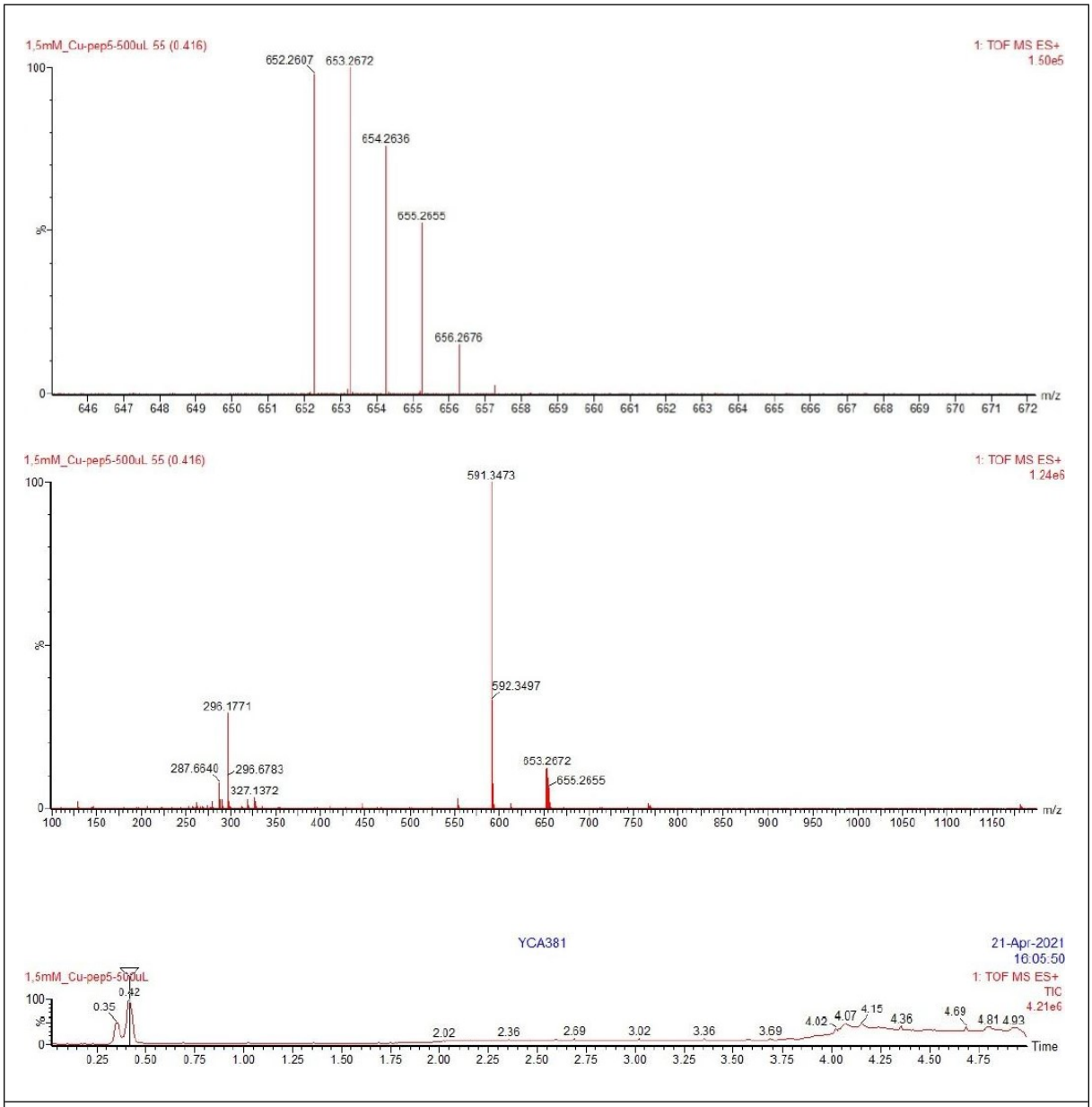

Figure S47. (Top) Zoom in (*m/z* 646 – 672) into (middle) the full range HR ESI mass spectrum (*m/z* 100 – 1200) of **5** after *in situ* preparation by combining solutions of **e** and $CuCl_2$. Dilution with MeCN. (Below) Total ion current (TIC) chromatogram of the LC-MS measurement.

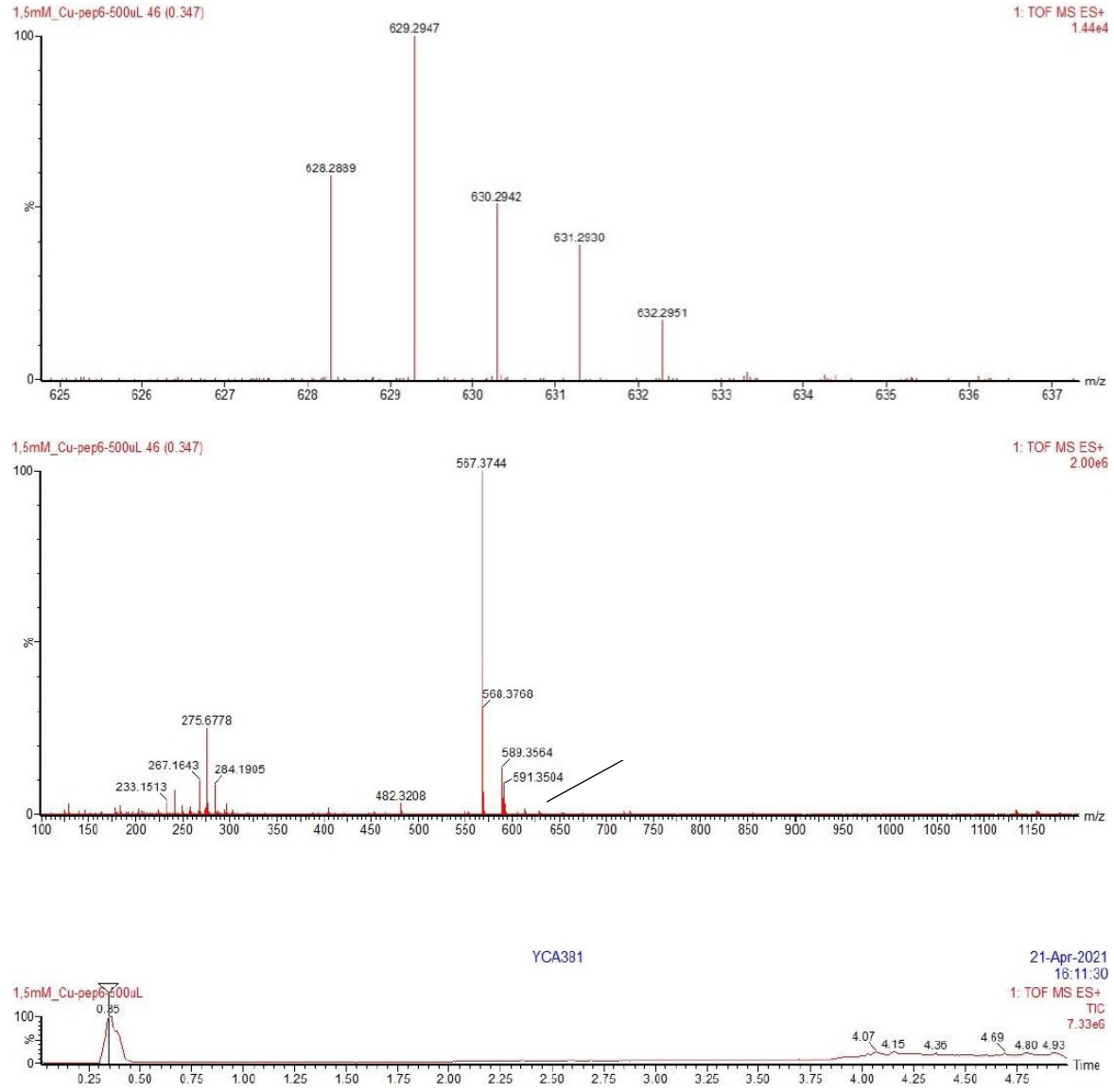

Figure S48. (Top) Zoom in (*m/z* 625 – 637) into (middle) the full range HR ESI mass spectrum (*m/z* 100 – 1200) of **6** after *in situ* preparation by combining solutions of **f** and $CuCl_2$. Dilution with MeCN. (Below) Total ion current (TIC) chromatogram of the LC-MS measurement.

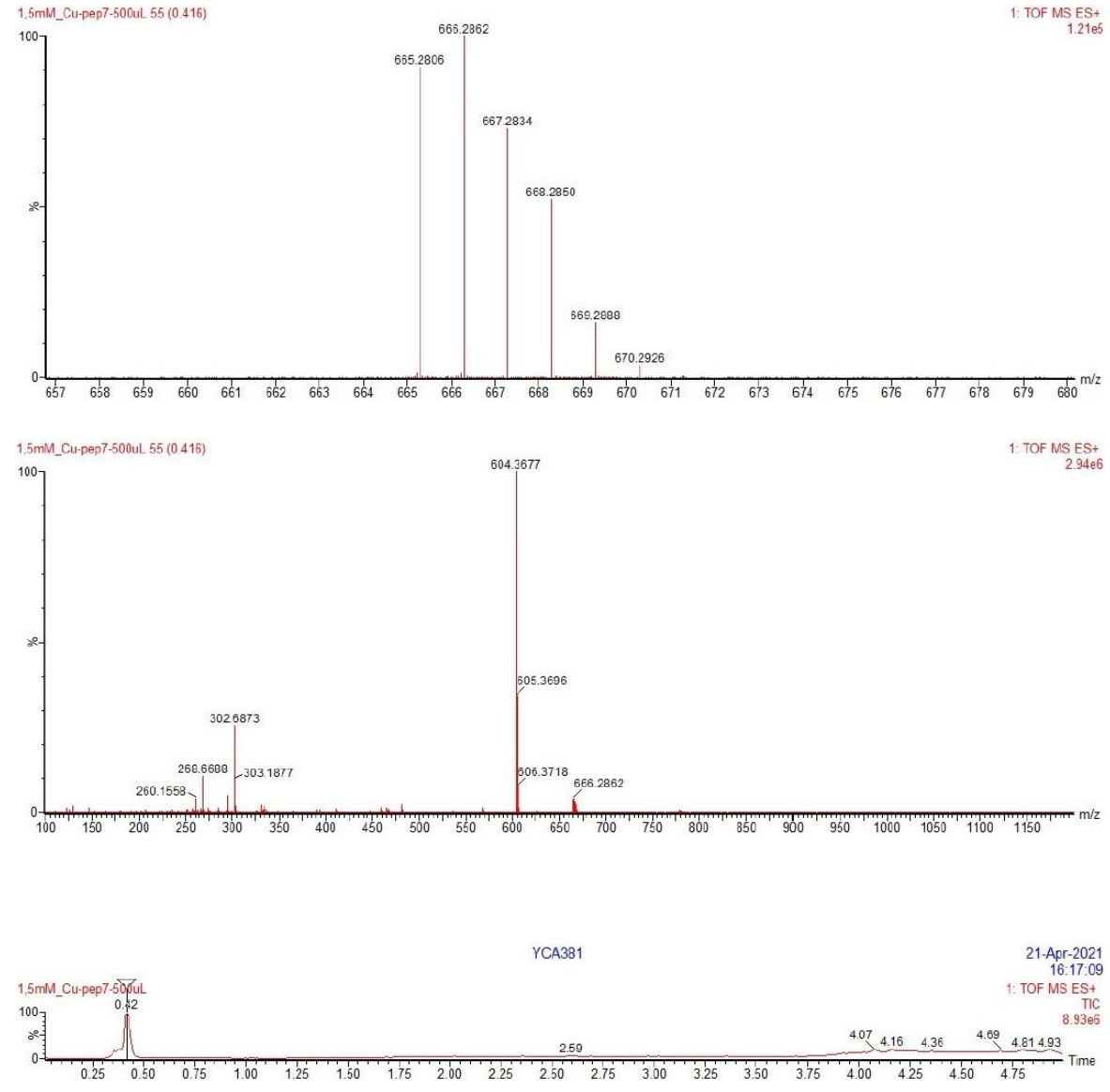

Figure S49. (Top) Zoom in (*m/z* 657 – 680) into (middle) the full range HR ESI mass spectrum (*m/z* 100 – 1200) of **7** after *in situ* preparation by combining solutions of **g** and $CuCl_2$. Dilution with MeCN. (Below) Total ion current (TIC) chromatogram of the LC-MS measurement.

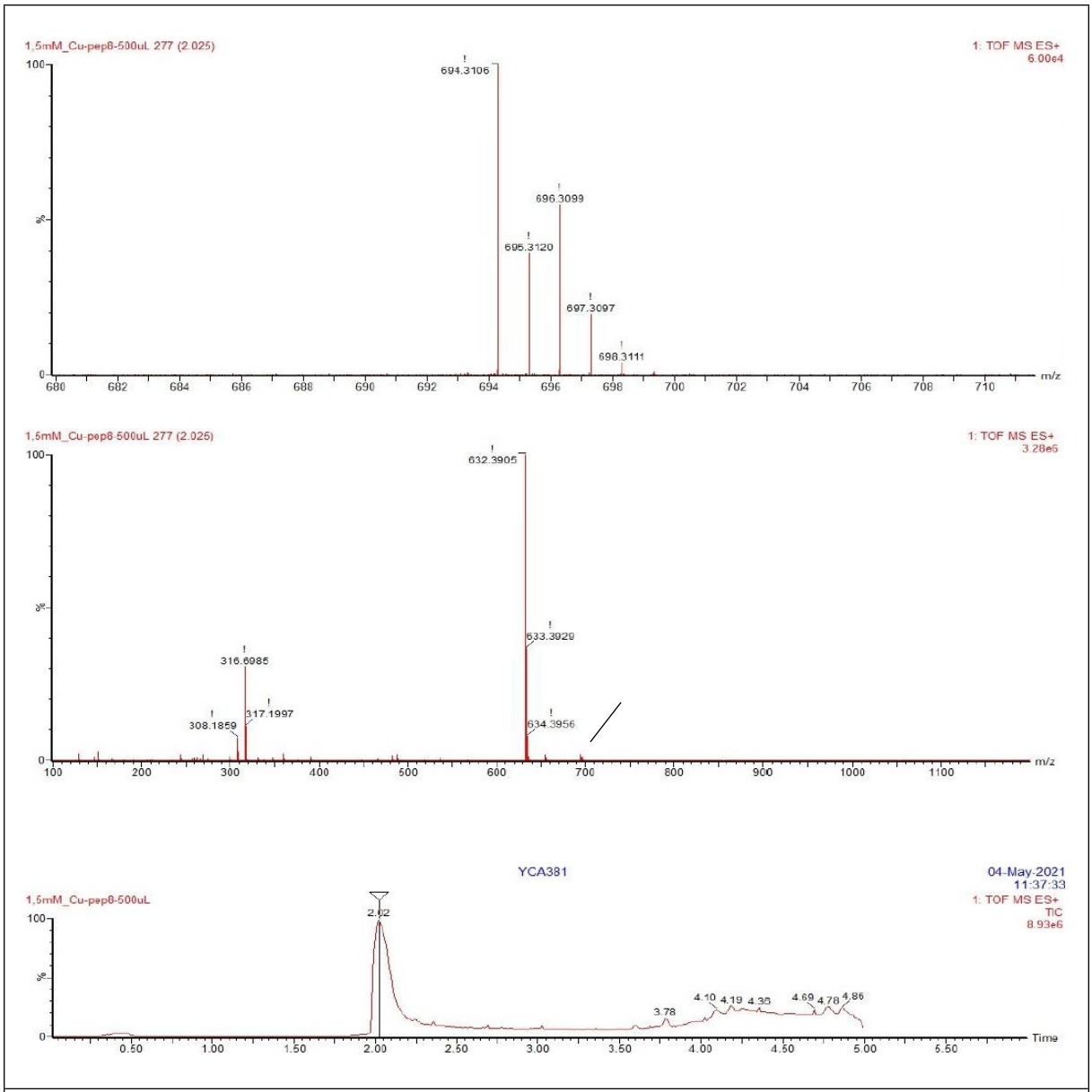

Figure S50. (Top) Zoom in (*m/z* 680 – 710) into (middle) the full range HR ESI mass spectrum (*m/z* 100 – 1200) of **8** after *in situ* preparation by combining solutions of **h** and $CuCl_2$. Dilution with MeCN. (Below) Total ion current (TIC) chromatogram of the LC-MS measurement.

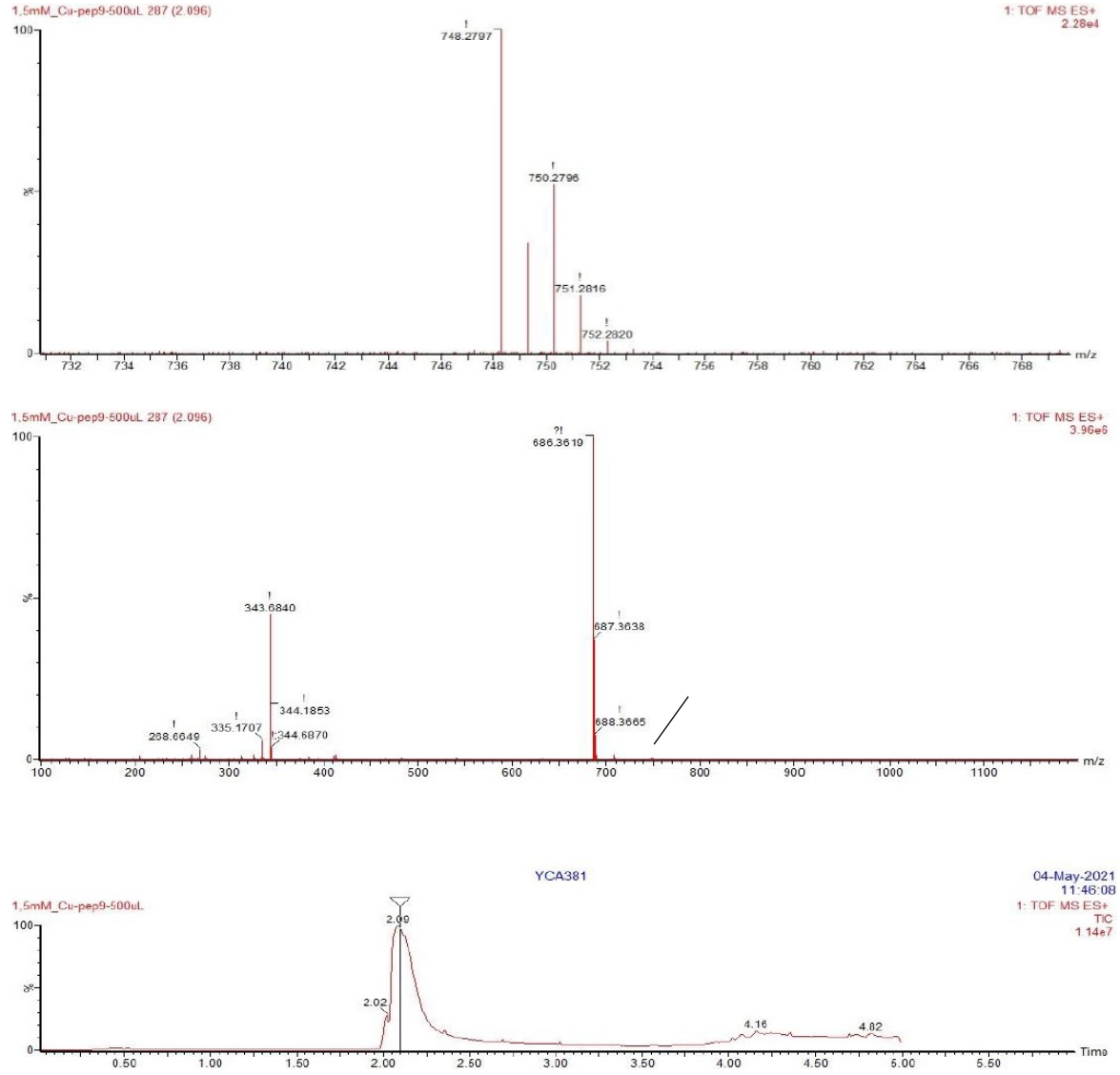

Figure S51. (Top) Zoom in (*m/z* 732 – 768) into (middle) the full range HR ESI mass spectrum (*m/z* 100 – 1200) of **9** after *in situ* preparation by combining solutions of **i** and $CuCl_2$. Dilution with MeCN. (Below) Total ion current (TIC) chromatogram (TIC) of the LC-MS measurement.

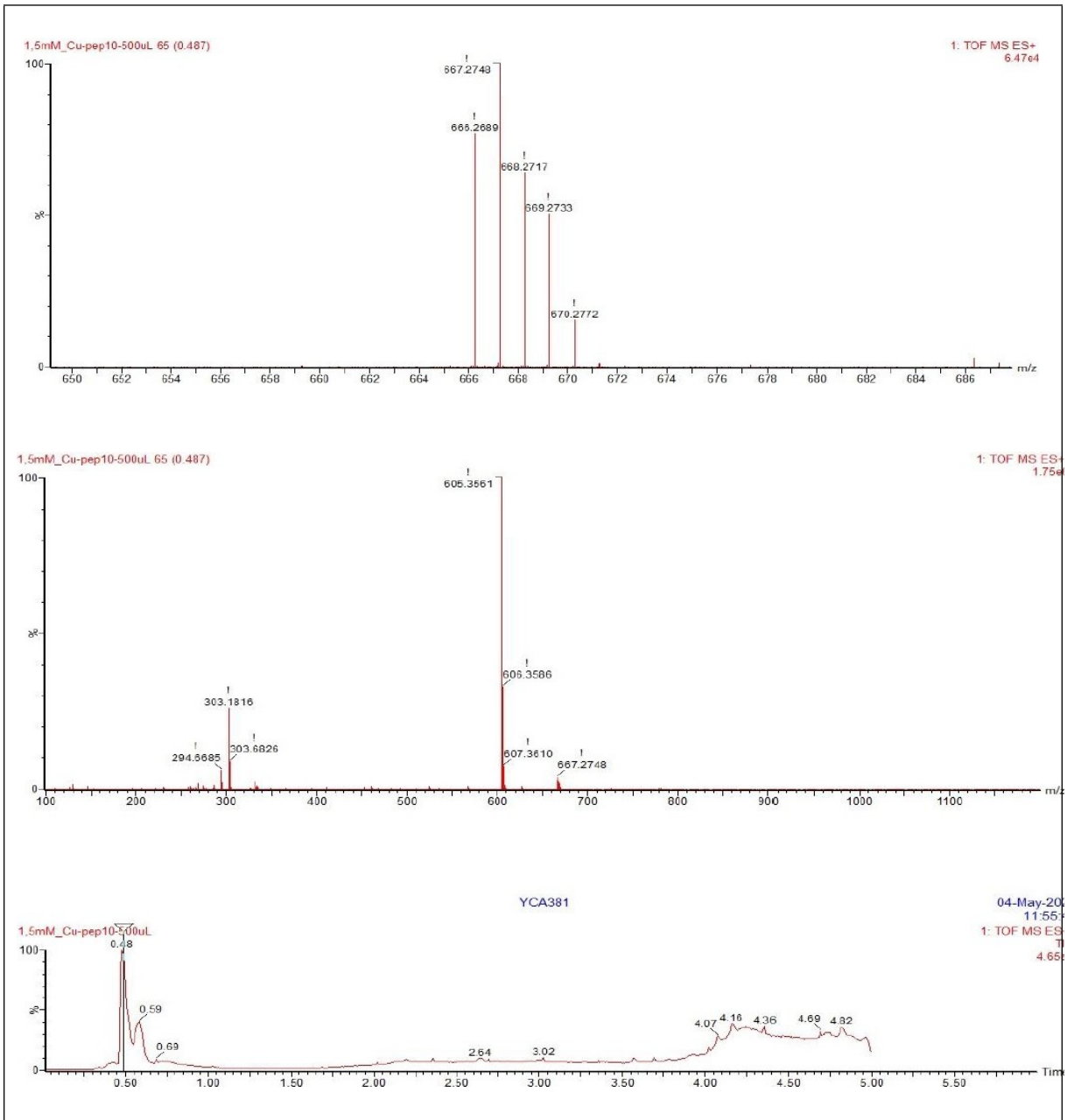

Figure S52. (Top) Zoom in (*m/z* 650 – 686) into (middle) the full range HR ESI mass spectrum (*m/z* 100 – 1200) of **10** after *in situ* preparation by combining solutions of **j** and $CuCl_2$. Dilution with MeCN. (Below) Total ion current (TIC) chromatogram of the LC-MS measurement.

S-6 DNA cleavage studies

Plasmid DNA pBR322 was purchased from Carl Roth. All DNA cleavage experiments were performed at least in triplicate to ensure reproducibility. The standard deviations are represented as the error bars. The *in situ* prepared complexes **1**–**10** (55 µM $CuCl_2$ / 68.75 µM peptide, Cu(II):peptide = 1:1.25, see S-5) were incubated with plasmid DNA pBR322 (0.025 mg/mL) buffered in HEPES (50 mM, pH 7.4) in the presence of $AscH^-$ (1 mM) as reducing agent for 1 h at 37 °C. Gel electrophoresis was carried out for 2 h at 40 V using a 1% agarose gel in 0.5X TBE buffer containing ethidium bromide (EtBr) (0.2 µg/mL). The bands of *supercoiled* (form 1), *open circular*/*nicked* (form 2), and *linear* (form 3) DNA were visualized by fluorescence imaging of intercalating EtBr on a *Bio-Rad Gel Doc EZ Imager*. Data analysis was performed with *Bio-Rad's Image Lab Software* (Version 3.0). Due to the decreased affinity of EtBr to supercoiled DNA a correction factor of 1.22 was used.[8]

For the ROS quenching assay, the following ROS scavengers were added individually or together to the tested complex **2** and **6** (52.5 µM) under the same incubation conditions: DMSO (400 mM), NaN_3 (10 mM), sodium pyruvate (2.5 mM) and SOD (625 U/mL).

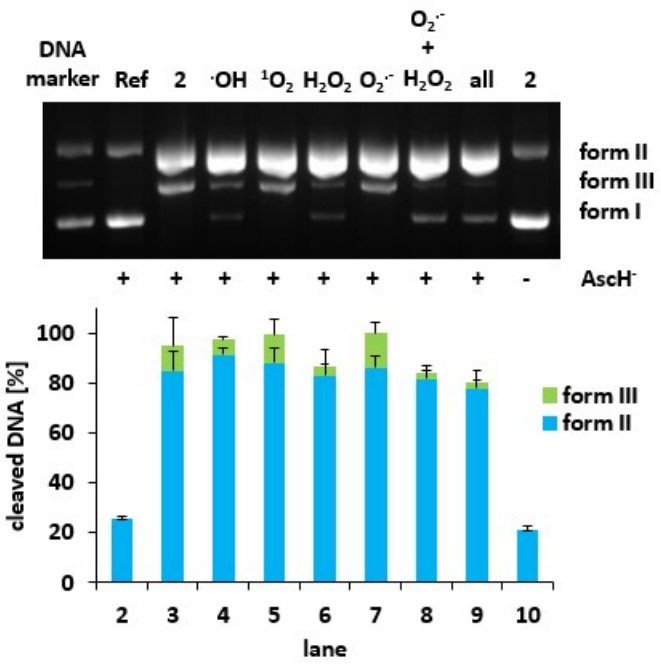

Figure S53. (Top) Cleavage of plasmid DNA pBR322 (0.2 µg) by complex **2** (52.5 µM) in HEPES buffer (50 mM, pH 7.4) in the presence of $AscH^-$ (1 mM). Incubation for 1 h at 37°C in the absence and presence of corresponding ROS scavengers. Lane 1: DNA marker (form I, II and III), lane 2: DNA reference, lane 3: **2**, lanes 4-9: **2** and scavengers for the indicated ROS (DMSO (400 mM), NaN_3 (10 mM), pyruvate (2.5 mM), SOD (625 U/mL), pyruvate (2.5 mM) + SOD (625 U/mL), all scavengers), lane 10: **6** without $AscH^-$ (Bottom) Visualization of the extent of DNA cleavage in percent. Error bars represent the standard deviation from at least three experiments.

S-7 Reactive oxygen species (ROS)

The evolution of ·OH and H_2O_2 was measured *via* a kinetic ROS fluorescence assay: Terephthalate (TPA) was used for ·OH and pentafluorobenzenesulfonyl fluorescein (PBSF) for H_2O_2 detection. The complexes **1**-**10** (50 µM) were incubated either with TPA (0.5 mM) or PBSF (25 µM) in the presence of $AscH^-$ (1 mM) in HEPES buffer (50 mM, pH 7.4) at room temperature and followed by fluorescence spectroscopy for 45 min (·OH: λ_{ex} = 320 nm and λ_{em} = 428 nm, photomultiplier voltage = 900 V; H_2O_2: λ_{ex} = 485 nm and λ_{em} = 513 nm, photomultiplier voltage = 750 V). The data time interval was 15 s. Incubation was carried out in 1.4 mL quartz cuvettes (*Hellma Analytics*).

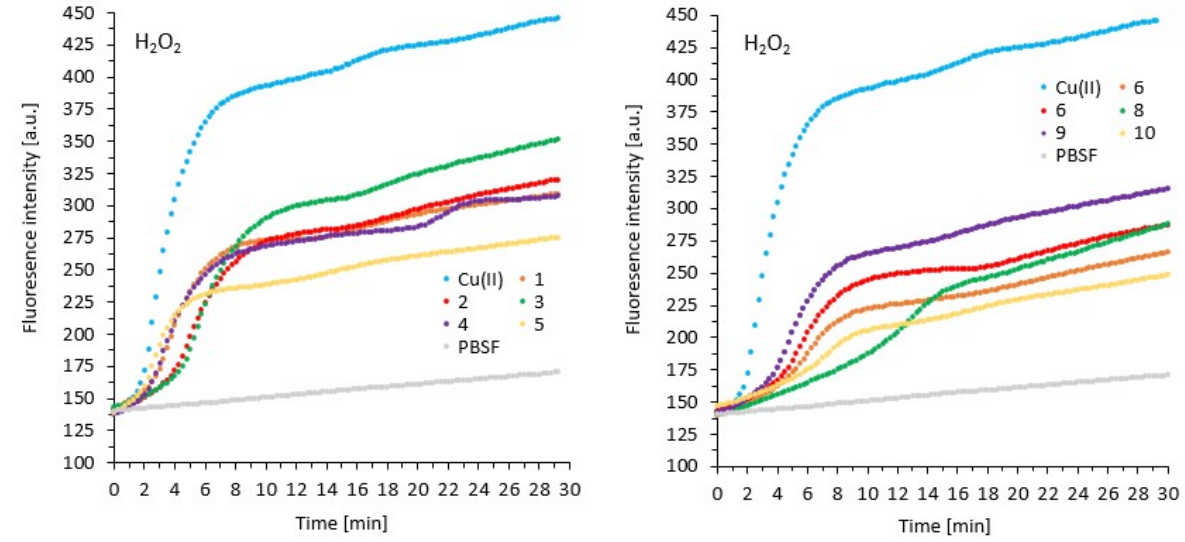

Figure S54. Kinetics of H_2O_2 production for Gly complexes **1**-**5** (50 µM) (left) and β-Ala complexes **6**-**10** (50 µM) (right) in the presence of $AscH^-$ (1 mM) in HEPES buffer (50 mM, pH 7.4) monitored by fluorescence evolution of fluoresceine (λ_{ex} = 485 nm, λ_{em} = 513 nm) for 30 min. In both graphs the same measurement of $CuCl_2$ (50 µM), dedicated as Cu(II), and PBSF as negative control (25 µM) is implemented for Gly (7,5,6) *vs.* β-Ala (7,6,6) comparison reasons.

A slight increase of the PBSF signal intensity (negative control) within 30 min is caused by auto-perhydrolysis at room temperature during the experiment, since the PBSF stock is stored at -20 °C. This behavior has been observed previously in our laboratory.[3]

S-8 DNA binding studies

In this work for Cu(II) ATCUN-based complexes **1**-**10** and $CuCl_2$ three DNA binding methods were carried out: The EtBr displacement assay *via* fluorescence, DNA melting curves *via* UV/VIS and CD spectroscopy.

S-8.1 Ethidium bromide (EtBr) displacement assay

A mixture of calf thymus (CT)-DNA (20 µM) and EtBr (1.3 µM) in HEPES buffer (50 mM, pH 7.4) was prepared in a 1 mL fluorescence cuvette. After 15 min, this solution was treated with increasing amounts of the *in situ* prepared complexes **1**–**10** and $CuCl_2$. The fluorescence spectra were collected after each addition, mixing and a waiting time of 1 min in a range of 550–700 nm using an excitation wavelength of 518 nm (photomultiplier voltage: 860 V).
In the presence of DNA, EtBr emits intense fluorescence at λ_{em} = 603 nm due to intercalation of EtBr between the base pairs of the DNA. Competitive DNA binder molecules can displace EtBr causing a decreased fluorescence emission.[9] The magnitude of decrease of the fluorescence emission is described by the Stern-Volmer equation.[10]

$$\frac{I_0}{I} = 1 + K_{SV}[Q] \qquad (1)$$

where I_0 is the fluorescence emission in absence and I in presence of a competitive binder, and [Q] is the concentration of the latter. Titration of a competitive quencher yields the Stern-Volmer constant K_{SV} by plotting its concentration [Q] against I_0/I. To obtain the binding constant K_{app} towards DNA the equation

$$K_{EtBr}[EtBr] = K_{app}[Q] \qquad (2)$$

was used, where K_{EtBr} is the binding constant of EtBr towards DNA (10^7 M^{-1})[11] and [$EtBr$] is the concentration of EtBr (1.3 µM). [Q] is the concentration of the competitive binder, where the fluorescence emission of EtBr is quenched by 50%, which can be calculated by using equation (1).
The calculated Stern-Volmer constants K_{SV} and the apparent binding constants K_{app} for **1**–**10** and $CuCl_2$ are listed in Table 1. The EtBr displacement from the EtBr-CT-DNA system (1.3 µM EtBr, 20 µM CT-DNA) in HEPES buffer (50 mM, pH 7.4) by titration of the complexes **1**–**10** and $CuCl_2$ are shown in Figures S55–S65.
Since the I_0/I plot for complexes **1**-**4** and $CuCl_2$ showed a static quenching (linear graph) and for **5**-**10** both a static and dynamic quenching (0-5 µM an upward curvature and from 5 µM on

a linear behavior), for comparison reasons a linear regression starting from 5 µM to the end concentration of the experiment for **5**-**10** was used for K_{app} calculations.[12]

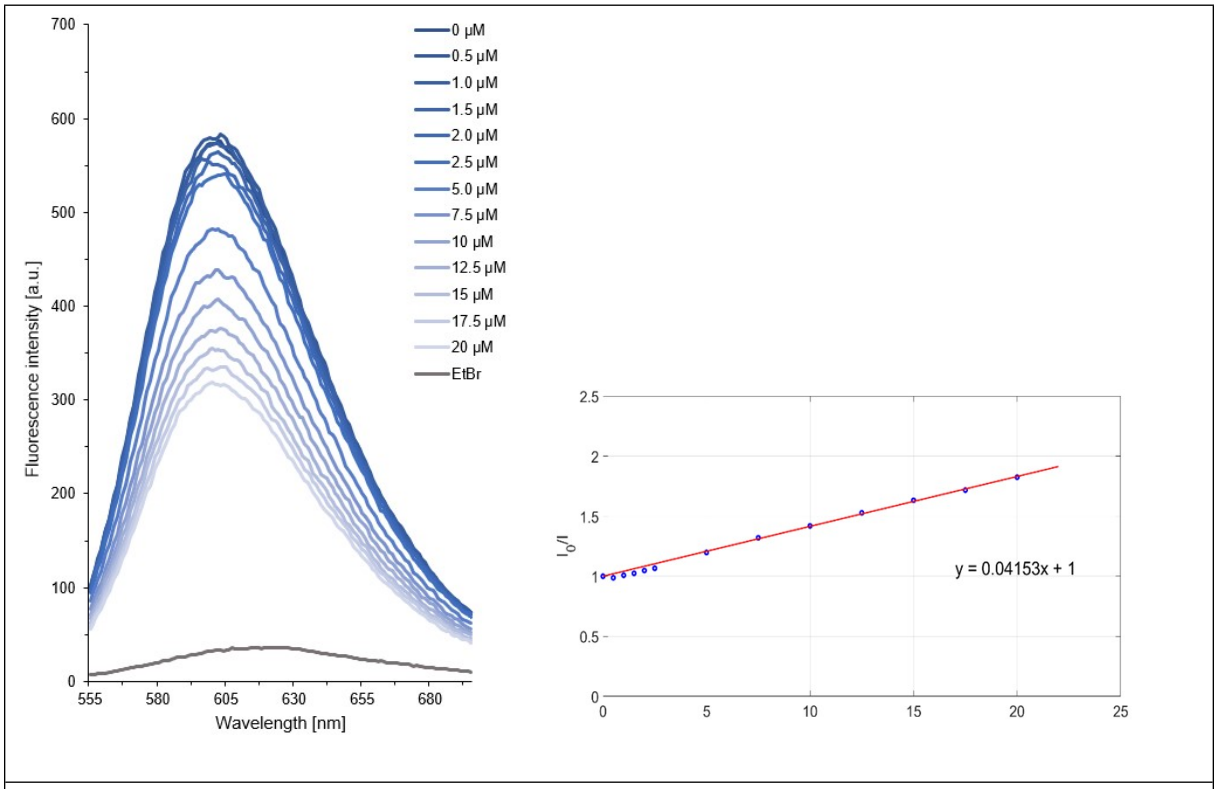

Figure S55. (Left) EtBr displacement of the EtBr-CT-DNA system (1.3 µM EtBr, 20 µM CT-DNA) in HEPES buffer (50 mM, pH 7.4) by titration of the Cu(II) ATCUN complex **1** (0–20 µM). (Right) I_0/I over [Q] to calculate K_{SV}.

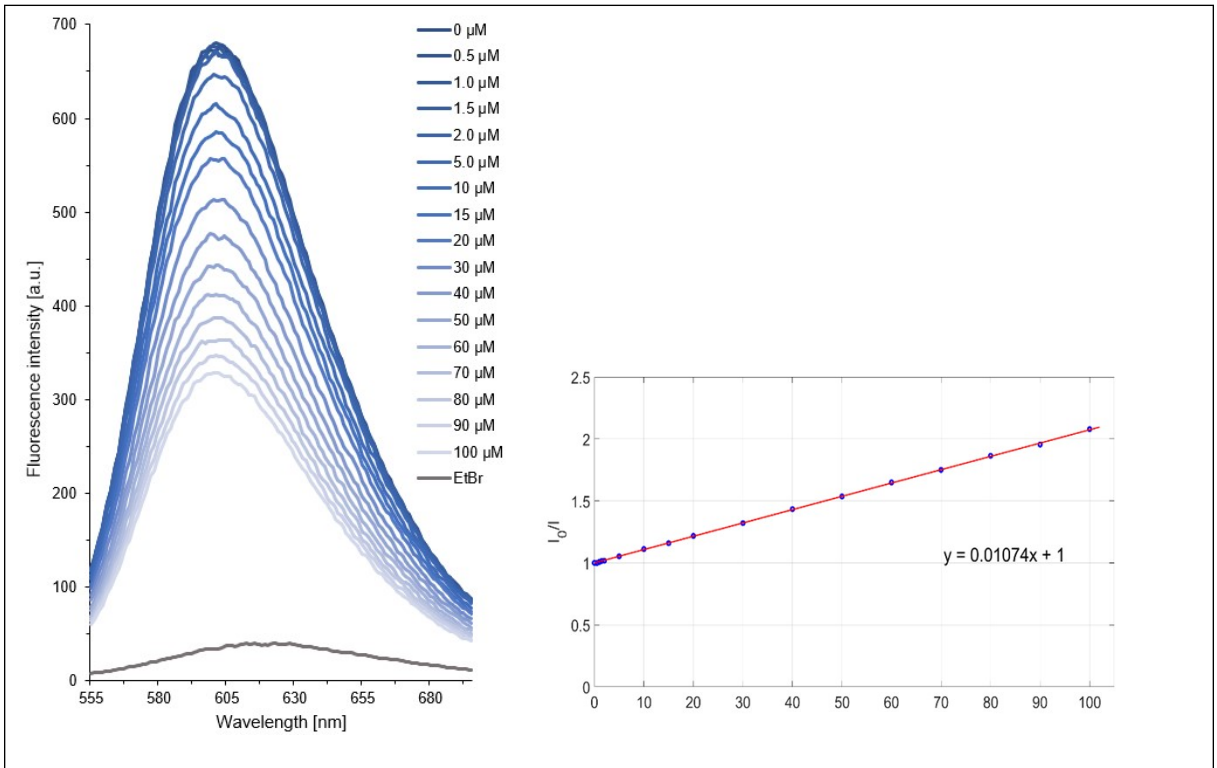

Figure S56. (Left) EtBr displacement of the EtBr-CT-DNA system (1.3 µM EtBr, 20 µM CT-DNA) in HEPES buffer (50 mM, pH 7.4) by titration of the Cu(II) ATCUN complex **2** (0–100

µM). (Right) I_0/I over [Q] to calculate K_{SV}.

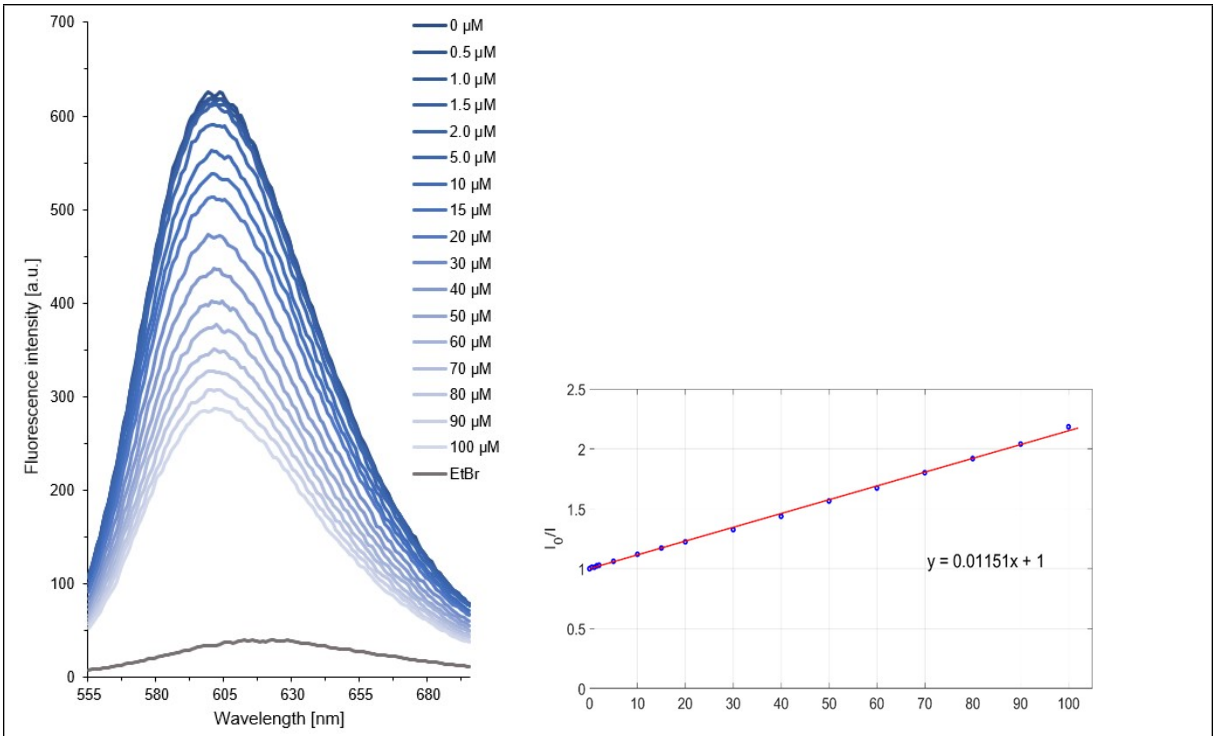

Figure S57. (Left) EtBr displacement of the EtBr-CT-DNA system (1.3 µM EtBr, 20 µM CT-DNA) in HEPES buffer (50 mM, pH 7.4) by titration of the Cu(II) ATCUN complex **3** (0–100 µM). (Right) I_0/I over [Q] to calculate K_{SV}.

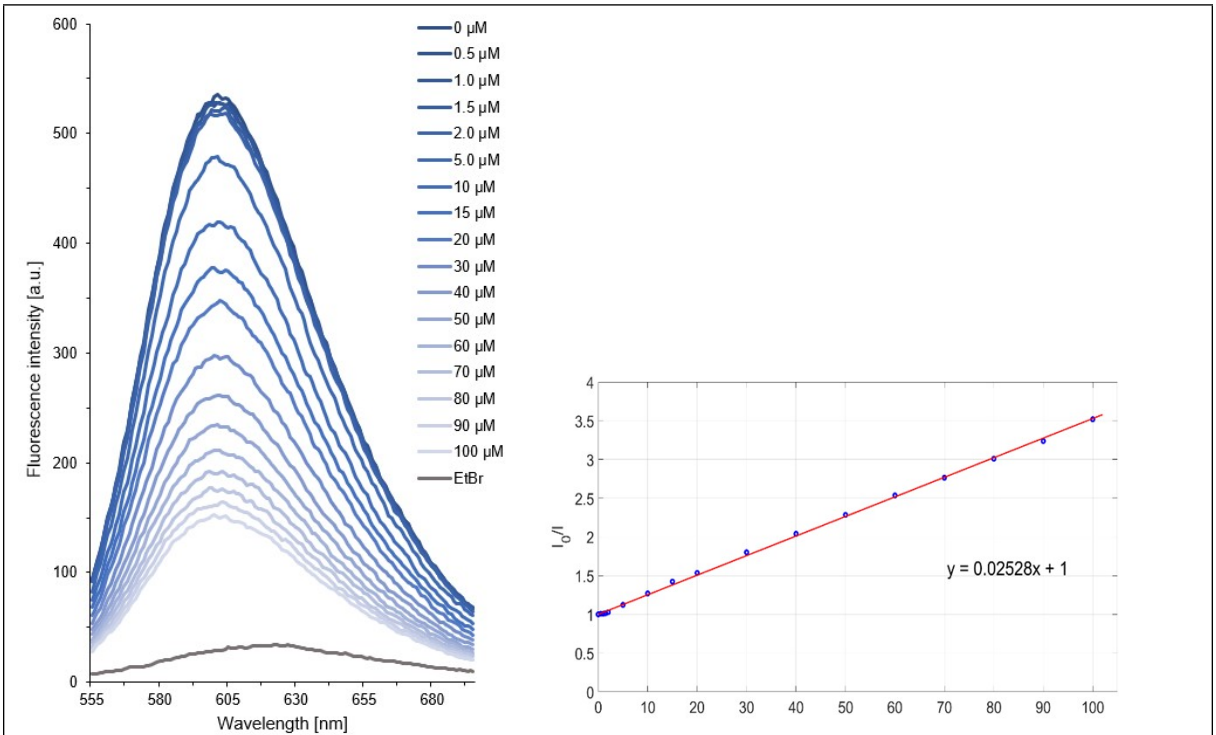

Figure S58. (Left) EtBr displacement of the EtBr-CT-DNA system (1.3 µM EtBr, 20 µM CT-DNA) in HEPES buffer (50 mM, pH 7.4) by titration of the Cu(II) ATCUN complex **4** (0–100

µM). (Right) I_0/I over [Q] to calculate K_{SV}.

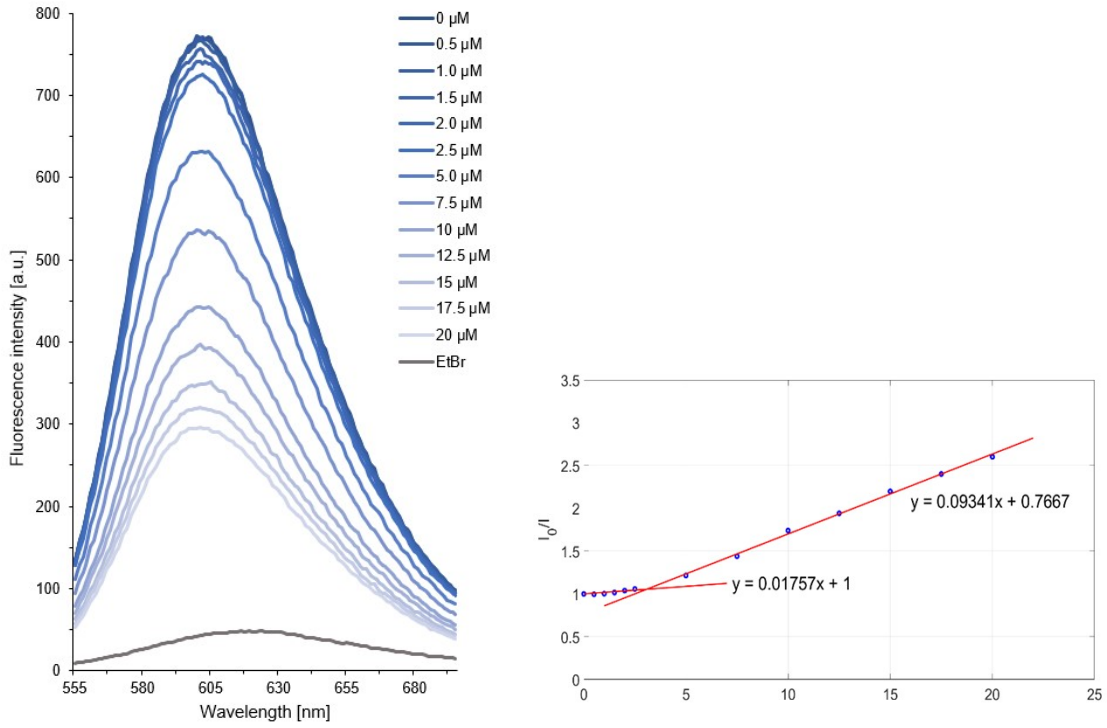

Figure S59. (Left) EtBr displacement of the EtBr-CT-DNA system (1.3 µM EtBr, 20 µM CT-DNA) in HEPES buffer (50 mM, pH 7.4) by titration of the Cu(II) ATCUN complex **5** (0–20 µM). (Right) I_0/I over [Q] to calculate K_{SV}.

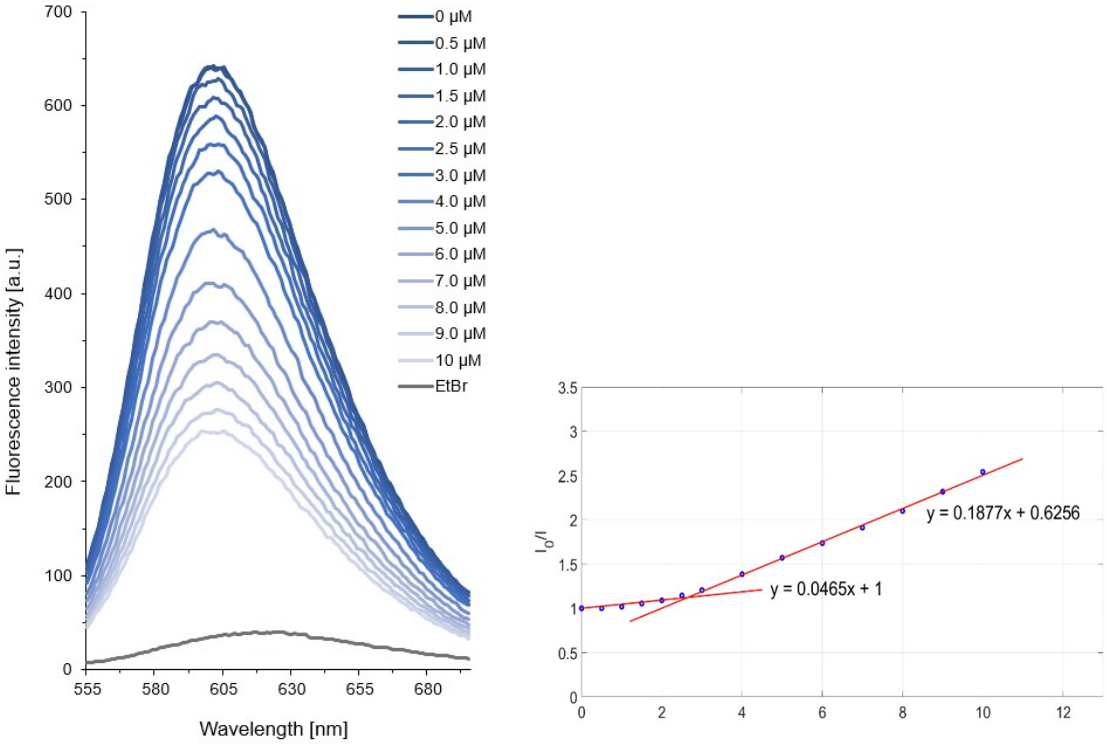

Figure S60. (Left) EtBr displacement of the EtBr-CT-DNA system (1.3 µM EtBr, 20 µM CT-

DNA) in HEPES buffer (50 mM, pH 7.4) by titration of the Cu(II) ATCUN complex **6** (0–10 µM). (Right) I_0/I over [Q] to calculate K_{SV}.

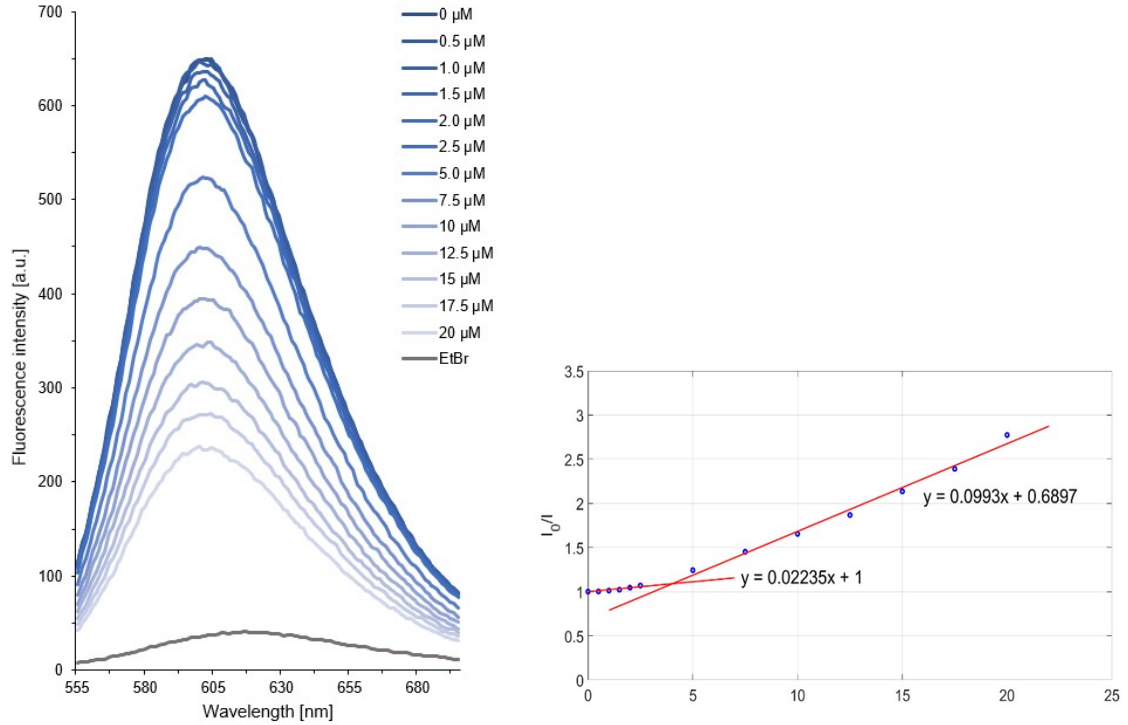

Figure S61. (Left) EtBr displacement of the EtBr-CT-DNA system (1.3 µM EtBr, 20 µM CT-DNA) in HEPES buffer (50 mM, pH 7.4) by titration of the Cu(II) ATCUN complex **7** (0–20 µM). (Right) I_0/I over [Q] to calculate K_{SV}.

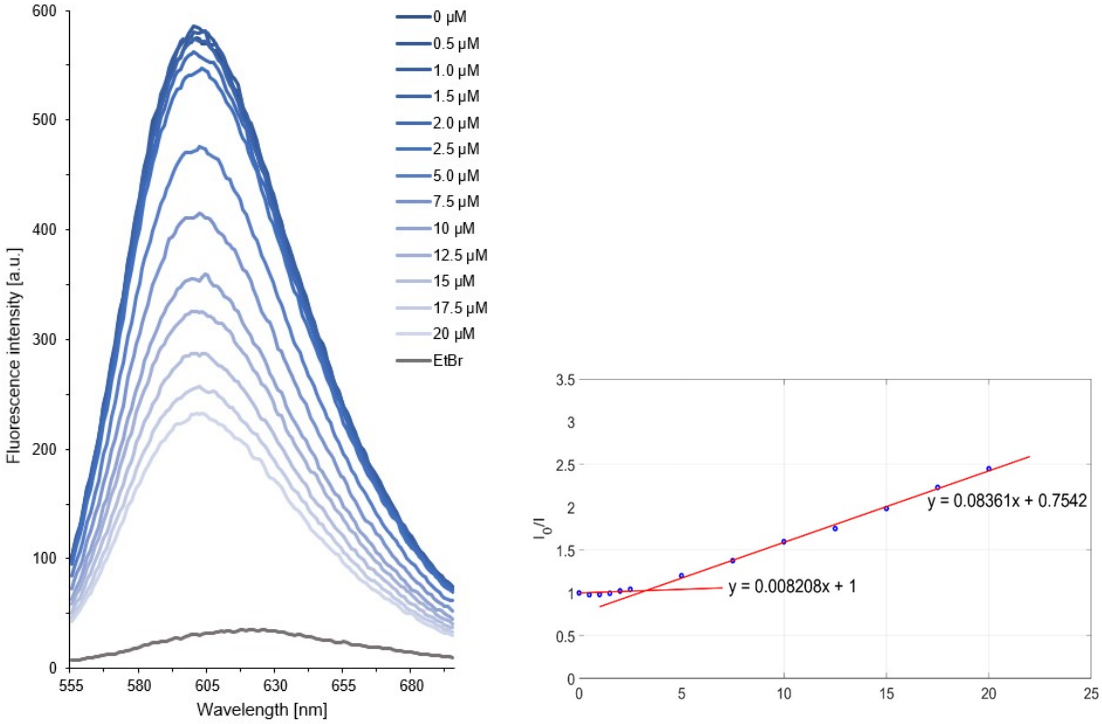

Figure S62. (Left) EtBr displacement of the EtBr-CT-DNA system (1.3 µM EtBr, 20 µM CT-DNA) in HEPES buffer (50 mM, pH 7.4) by titration of the Cu(II) ATCUN complex **8** (0–20 µM).

(Right) I_0/I over [Q] to calculate K_{SV}.

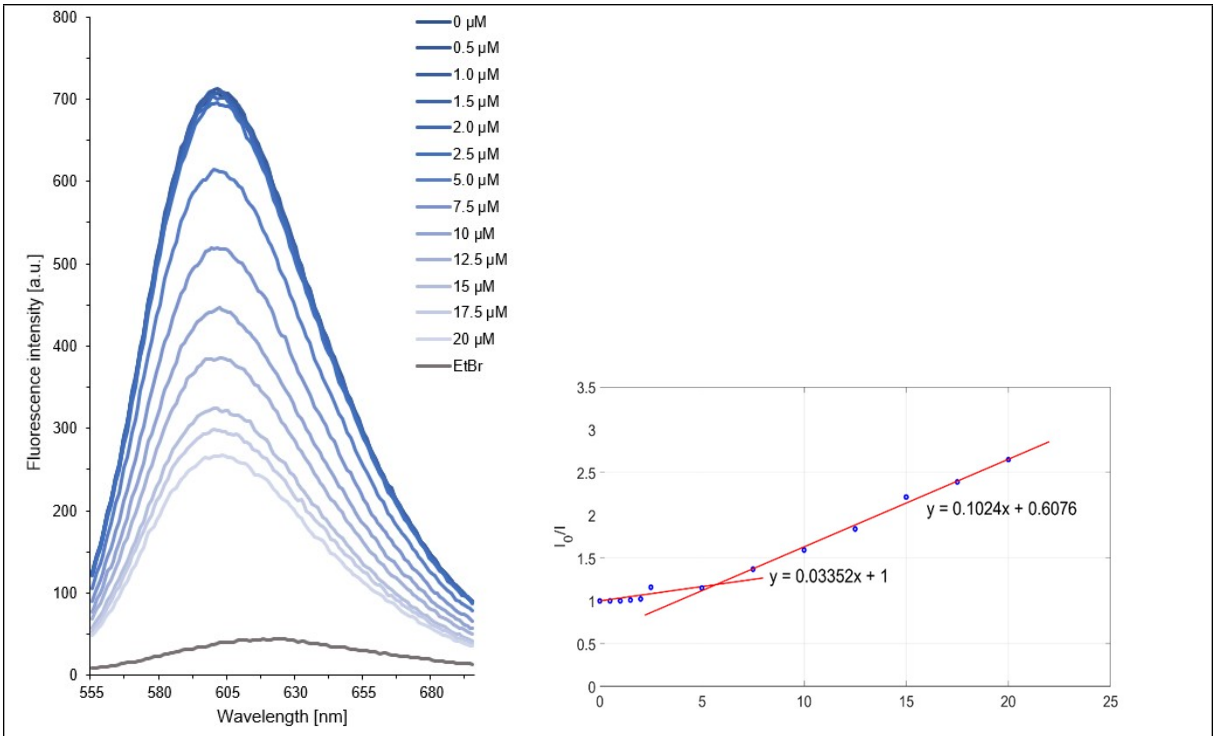

Figure S63. (Left) EtBr displacement of the EtBr-CT-DNA system (1.3 µM EtBr, 20 µM CT-DNA) in HEPES buffer (50 mM, pH 7.4) by titration of the Cu(II) ATCUN complex **9** (0–20 µM). (Right) I_0/I over [Q] to calculate K_{SV}.

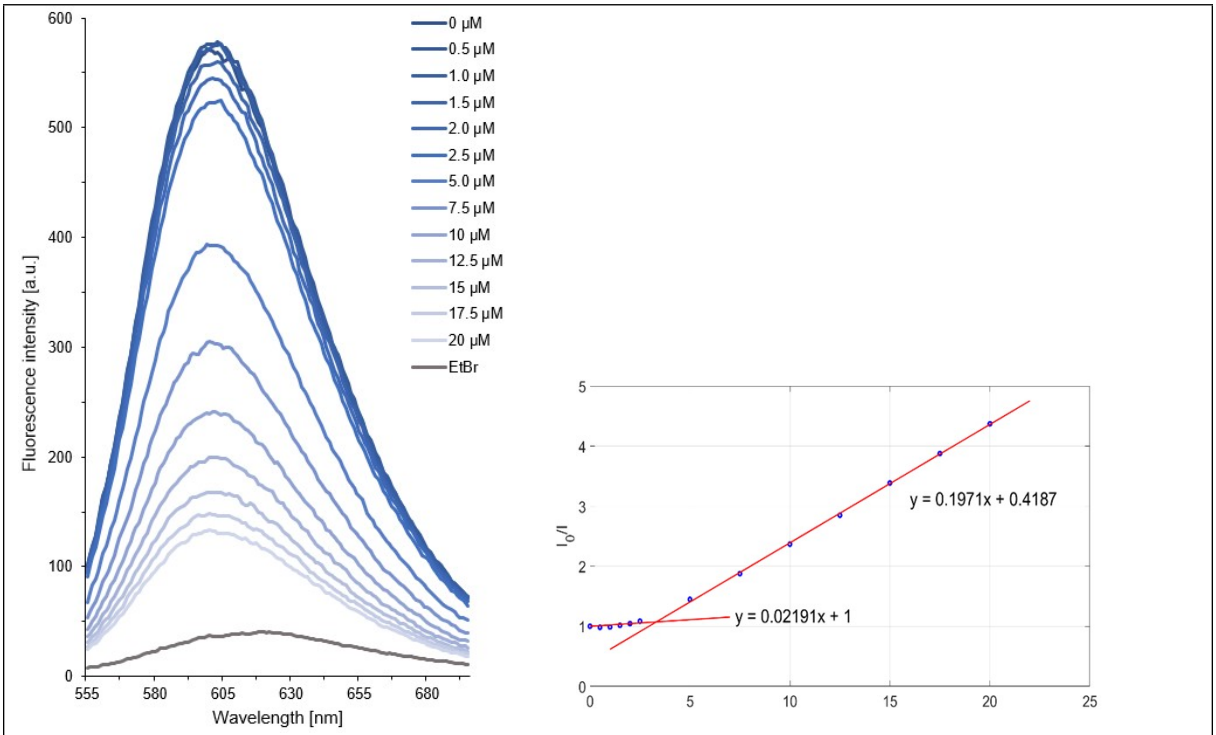

Figure S64. (Left) EtBr displacement of the EtBr-CT-DNA system (1.3 µM EtBr, 20 µM CT-DNA) in HEPES buffer (50 mM, pH 7.4) by titration of the Cu(II) ATCUN complex **10** (0–20

µM). (Right) I_0/I over [Q] to calculate K_{SV}.

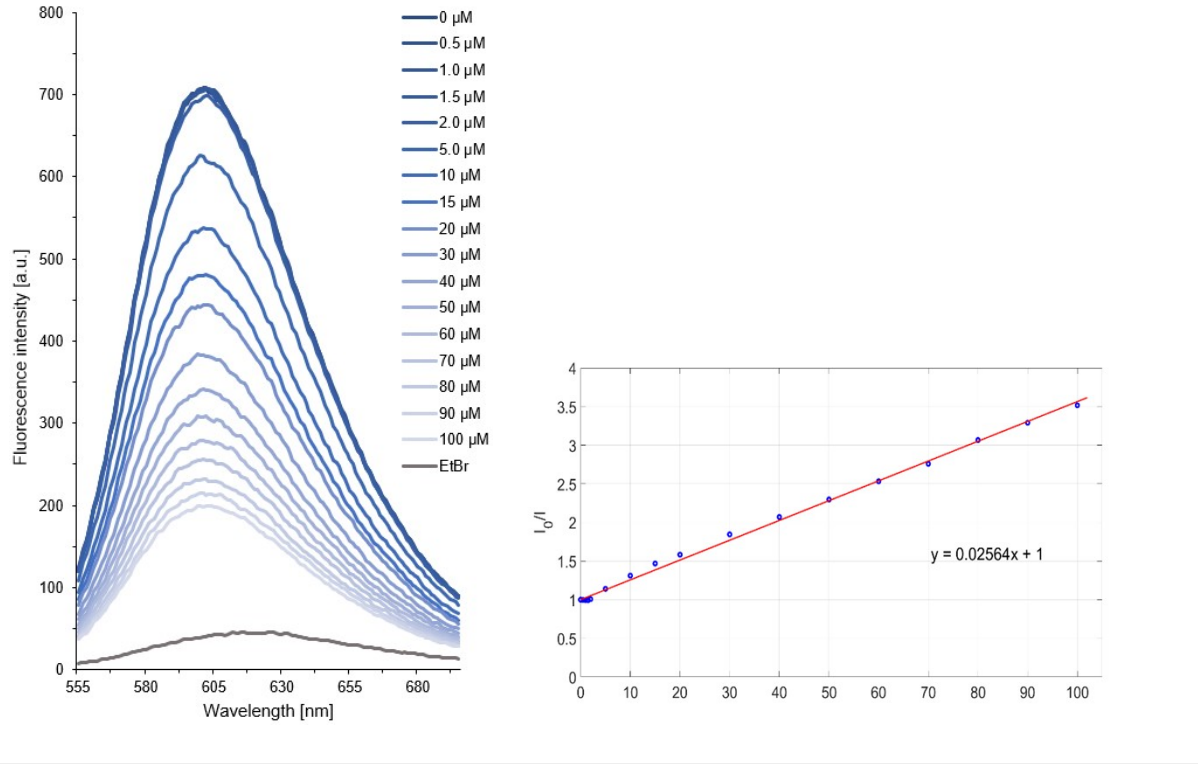

Figure S65. (Left) EtBr displacement of the EtBr-CT-DNA system (1.3 µM EtBr, 20 µM CT-DNA) in HEPES buffer (50 mM, pH 7.4) by titration of the Cu(II) ATCUN complex $CuCl_2$ (0–100 µM). (Right) I_0/I over [Q] to calculate K_{SV}.

S-8.2 DNA melting curves

DNA melting curves of CT-DNA (50 µM) in HEPES buffer (50 mM, pH 7.4) in the presence of the *in situ* prepared Cu(II) ATCUN complexes **1**–**10** or $CuCl_2$ (2.5 µM) were measured at 260 nm using a heating rate of 0.5 °C/min. Four *Hellma* cuvettes with 1 mL sample volume each were used for carrying out the experiment simultaneously. For each compound, DNA melting curves were recorded at least as triplicate for standard deviation calculation. Normalization of melting curves was utilized for better visualization.

In DNA melting experiments, the melting temperature T_m is the point where 50% of the double-stranded DNA is split into two single strands. Due to different extinction coefficients at 260 nm for double-stranded DNA and two single DNA strands, T_m can be determined via UV/VIS spectroscopy (Figure S66).[13] Thereby, an increase of T_m (Table 1) by adding complexes **1**–**10** or $CuCl_2$ (2.5 µM) to CT-DNA (50 µM) gives information about the DNA interaction strength.

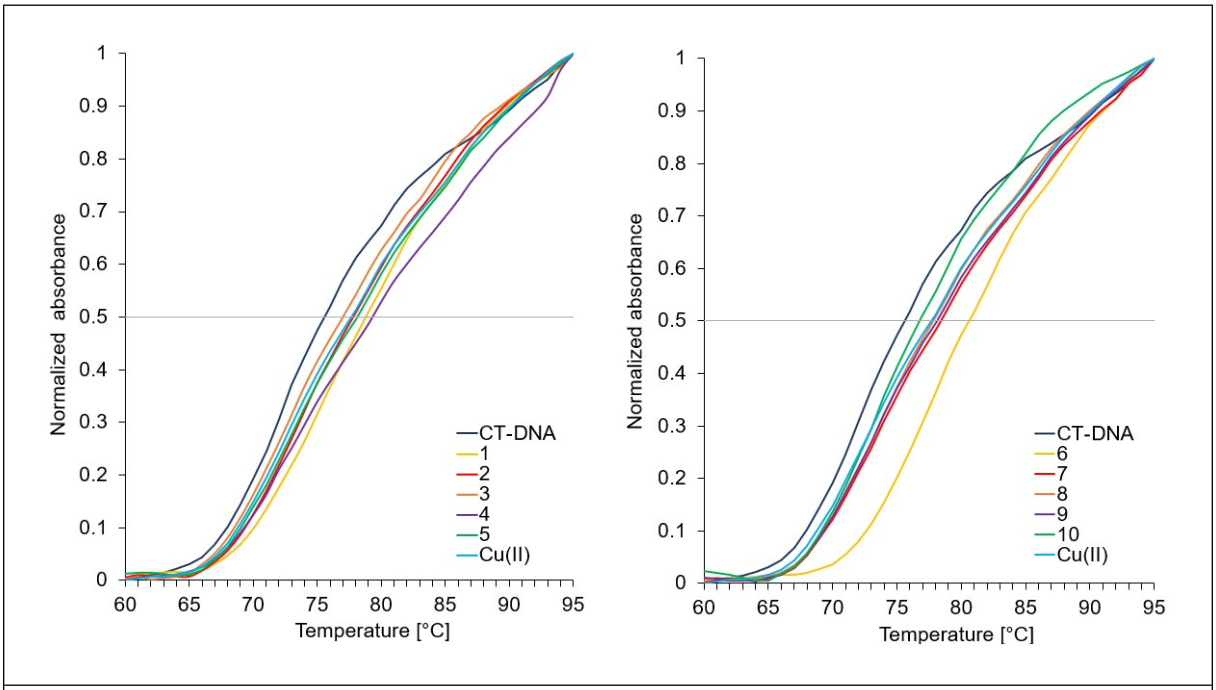

Figure S66. Normalized DNA melting curves in the presence of Gly complexes **1**–**5** (left) and β-Ala complexes **6**-**10** (right). The same measurements for the DNA reference (CT-DNA without compound) and $CuCl_2$, referred to as Cu(II), are included in both graphs (left and right) for comparison.

S-8.3 CD spectroscopy

CD spectra of CT-DNA (100 µM) in HEPES buffer (50 mM, pH 7.4) were recorded at 37 °C in a range of 225 to 320 nm with a scan rate of 100 nm/min and a data point interval of 0.1 nm. The Cu(II) ATCUN-based complexes **1**-**10** or $CuCl_2$ (10 µM to 40 µM) were added stepwise to investigate their modes of interaction with DNA. The volume of all samples was adjusted to 1 mL.

CD spectroscopy is a convenient method that can be used for a better understanding of groove binding and electrostatic interactions of the complexes towards DNA. CT-DNA exhibits a positive band at around 275 nm in the CD spectrum due to base-stacking of nucleobases and a negative band at around 245 nm, which corresponds to the helicity of the DNA (B-form).[14] Significant alteration of the positive band indicates intercalation, while changes of the negative band hint to groove binding interactions.[15–17]

In Figures 6 and S67–S71 the CD spectra of CT-DNA alone and in the presence of different concentrations of complexes **1**–**7** and $CuCl_2$ are shown.

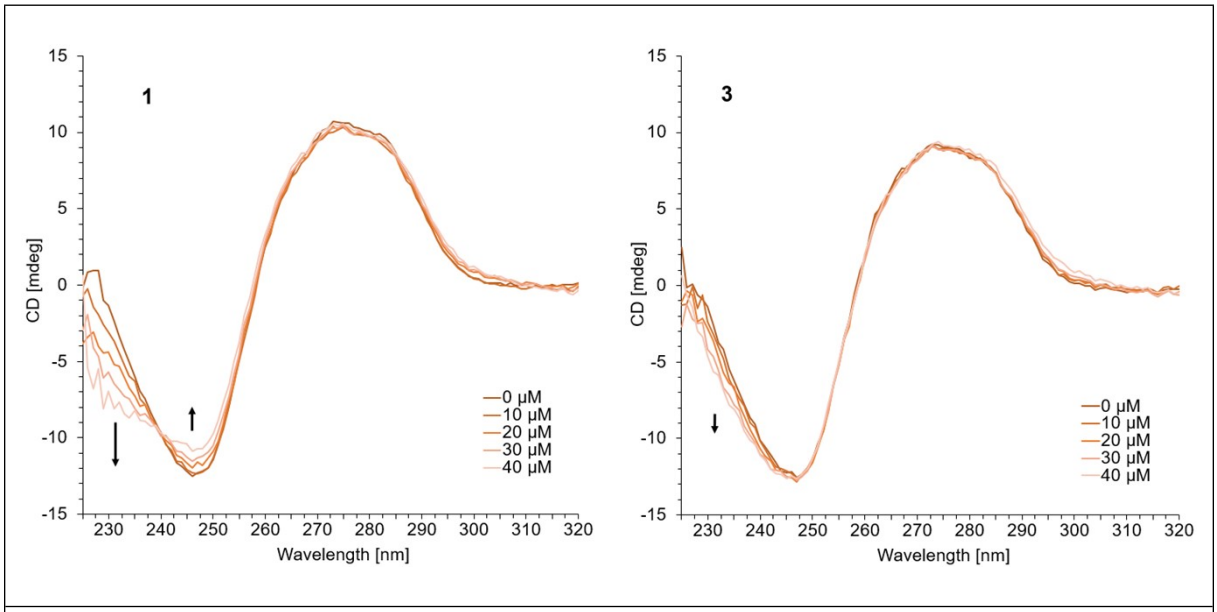

Figure S67. CD spectra of CT-DNA (100 µM) in HEPES buffer (50 mM, pH 7.4) at 37 °C with increasing concentrations (0–40 µM) of **1** (left) and **3** (right).

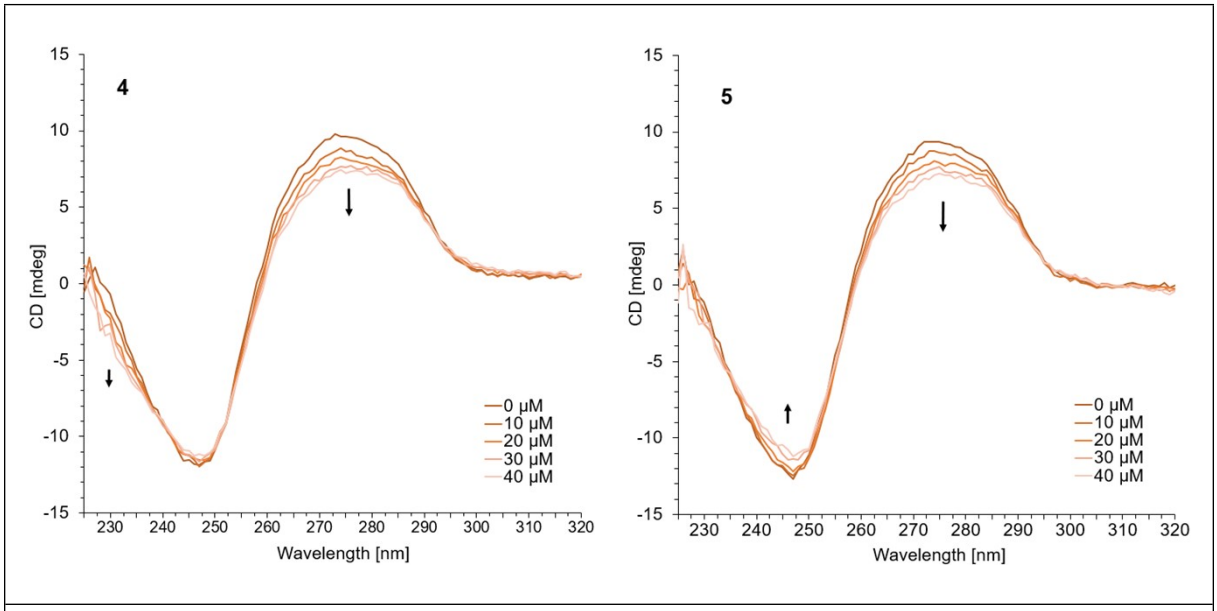

Figure S68. CD spectra of CT-DNA (100 µM) in HEPES buffer (50 mM, pH 7.4) at 37 °C with increasing concentrations (0–40 µM) of **4** (left) and **5** (right).

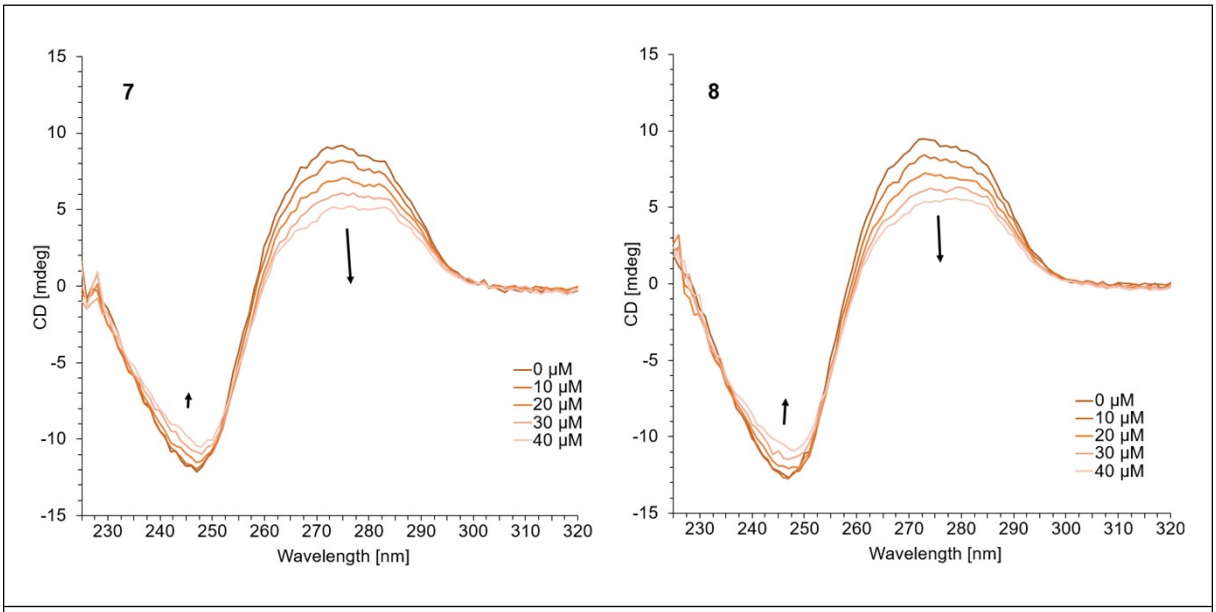

Figure S69. CD spectra of CT-DNA (100 µM) in HEPES buffer (50 mM, pH 7.4) at 37 °C with increasing concentrations (0–40 µM) of **7** (left) and **8** (right).

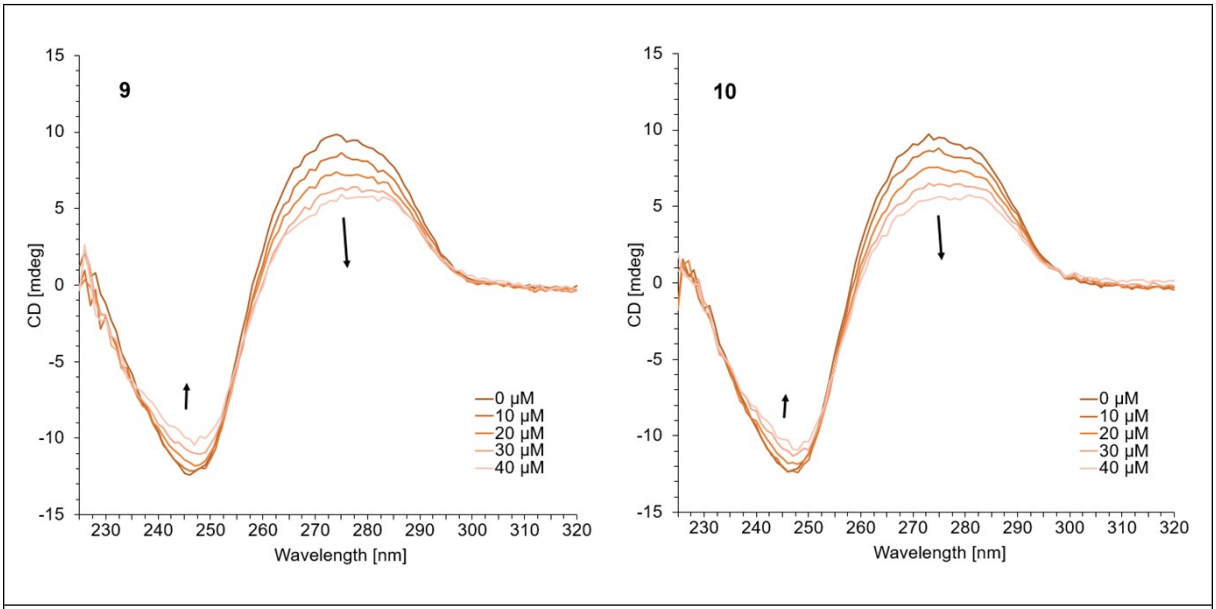

Figure S70. CD spectra of CT-DNA (100 µM) in HEPES buffer (50 mM, pH 7.4) at 37 °C with increasing concentrations (0–40 µM) of **9** (left) and **10** (right).

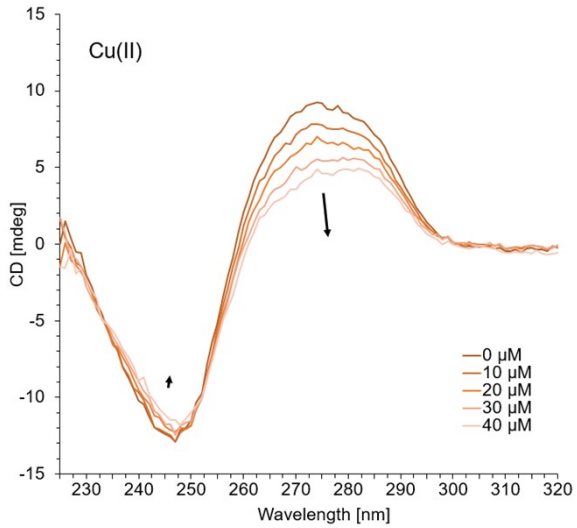

Figure S71. CD spectra of CT-DNA (100 µM) in HEPES buffer (50 mM, pH 7.4) at 37 °C with increasing concentrations (0–40 µM) of $CuCl_2$, referred to as Cu(II).

References

[1]	M. Marín-Luna, I. Alkorta, J. Elguero, *New J. Chem.* 2015, 39, 2861–2871.
[2]	Y. Jin, J. A. Cowan, *J. Am. Chem. Soc.* **2005**, 127, 8408–8415.
[3]	J. Heinrich, K. Bossak-Ahmad, M. Riisom, H. H. Haeri, T. R. Steel, V. Hergl, A. Langhans, C. Schattschneider, J. Barrera, S. M. F. Jamieson, M. Stein, D. Hinderberger, C. G. Hartinger, W. Bal, N. Kulak, *Chem. Eur. J* **2021**, 27, 18093–18102.
[4]	J. Barrera, H. H. Haeri, J. Heinrich, M. Stein, D. Hinderberger, N. Kulak, *Dalton Trans.* **2023**, 52, 3279–3286.
[5]	C. Bannwarth, S. Ehlert, S. Grimme, *J. Chem. Theory Comput.* **2019**, 15, 1652–1671.
[6]	P. Pracht, F. Bohle, S. Grimm, *Phys. Chem. Chem. Phys.* **2020**, 22, 7169–7192.
[7]	F. Furche, R. Ahlrichs, C. Hättig, W. Klopper, M. Sierka, F. Weigend, *WIREs Comput. Mol. Sci.* **2014**, 4, 91–100.
[8]	R. P. Hertzberg, P. B. Dervan, *Biochemistry* **1984**, 23, 3934–3945.
[9]	D. L. Boger, B. E. Fink, S. R. Brunette, W. C. Tse, M. P. Hedrick, *J. Am. Chem. Soc.* **2001**, 123, 5878–5891.
[10]	M. R. Eftink, C. A. Ghiron, *Anal. Biochem.* **1981**, 114, 199–227.
[11]	A. R. Morgan, J. S. Lee, D. E. Pulleyblank, N. L. Murray, D. H. Evans, *Nucleic Acids Res.* **1979**, *7*, 547–569.
[12]	M. Scaccaglia, S. Pinelli, L. Manini, B. Ghezzi, M. Nicastro, J. Heinrich, N. Kulak, P. Mozzoni, G. Pelosi, F. Bisceglie, *J. Inorg. Biochem.* **2024**, 251, 112438.
[13]	J. Wang, X. Pan, X. Liang, *J. Anal. Methods Chem.* **2016**, 2016, 5318935.
[14]	V. I. Ivanov, L. E. Minchenkova, A. K. Schyolkina, A. I. Poletayev, *Biopolymers* **1973**, 12, 89–110.
[15]	N. Shahabadi, S. Kashanian, A. Fatahi, *Bioinorg. Chem. Appl.* **2011**, 2011, 687571.
[16]	P. Uma Maheswari, M. Palaniandavar, *J. Inorg. Biochem.* **2004**, 98, 219–230.

[17]	C. Tong, G. Xiang, Y. Bai, *J. Agric. Food Chem.* **2010**, 58, 9, 5257–5262.